Effect of Phosphorus Doping on Young's Modulus and Residual Stress of Polysilicon Thin Films

by

Elena Bassiachvili

A thesis
presented to the University of Waterloo
in fulfillment of the
thesis requirement for the degree of
Master of Applied Science
in
Mechanical Engineering

Waterloo, Ontario, Canada, 2010

©Elena Bassiachvili 2010

AUTHOR'S DECLARATION

I hereby declare that I am the sole author of this thesis. This is a true copy of the thesis, including any required final revisions, as accepted by my examiners.

I understand that my thesis may be made electronically available to the public.

Abstract

On-chip characterization devices have been used to extract the Young's modulus, average stress and stress gradient of polysilicon doped with phosphorus using thermal diffusion. Devices for extracting the Young's modulus, average stress and stress gradients have been designed to work within the range of expected material property values. A customized fabrication process was developed and the devices were fabricated. Static and resonant tests were performed using clamped-clamped and cantilever beams in order to extract material properties. The experimental setup and detailed experimental results and analysis are outlined within.

Several doping concentrations have been studied and it has been concluded that the Young's modulus of polysilicon doped for 2 hours increases by approximately 50GPa and the average stress of polysilicon doped for 2.5 hours becomes more tensile by approximately 63 MPa. It has also been found that short doping times can introduce a large enough stress gradient to create a concave up curvature in free-standing structures. This work was performed in order to determine the usability of doping as a means to increase the sensitivity of temperature and pressure sensors for harsh environments. It has been concluded that doping is a promising technique and is worth studying further for this purpose.

Acknowledgements

First of all, I'd like to thank my supervisor, Dr. Patricia Nieva, without her, this work would simply not be possible. I have learned a great deal over the course of my degree and I am very grateful to her for that. I would like to thank Prof. Amir Khajepour who has also invested a lot of time into this project. I'd like to thank everyone I've worked with in the last two years, but particularly, Ali Najafi Sohi, Mohammad Shavezipur and Ryan Norris. They've so often provided me with valuable information or words of wisdom when I was struggling. I'd also like to thank the many people who have helped me with fabrication, Phani Madhavi Singaraju who performed several of the fabrication steps, Edward Xu from University of Toronto and Bill Jolley from University of Waterloo whose wealth of experience was invaluable, Rick Glew from University of Western Ontario who diced the wafers on such short notice, and many others who offered suggestions and hints when we worked together in the Pratt, CIRFE and G2n clean-rooms.

On a personal note, I would like to thank my wonderful parents, Vadim and Mila Bassiachvili, who instilled in me a curiosity and interest in the world around me, which I'm sure has lead me to pursue higher education. Their support, understanding and encouragement have been valuable beyond words. I'd like to thank my courageous boyfriend, Blake Rablah, who has put up with me spending my evenings and weekends at school in the name of research and just generally being awesome. I'd also like to thank him for proofreading my thesis. And I indubitably would like to thank my friends, Yulia Metersky, Semyon Mikheevskiy, Sara Molladavoodi, Mihaela Vlasea, Bahman Hadji, Aditya Chattopadhyay and Oxana Skiba for keeping me sane, it was no small task.

Dedication

To my grandparents, Zigfreid and Olga Bassiachvili, Boris Melamed and Lydia Khilgiyaeva.

Table of Contents

AUTHOR'S DECLARATION ii

Abstract iii

Acknowledgements iv

Dedication v

Table of Contents vi

List of Figures viii

List of Tables xiii

Chapter 1 Introduction 1

Chapter 2 Literature Review 4

2.1 Young's Modulus Measurement Techniques 4

2.2 Stress Measurement Techniques 6

2.3 Coefficient of Thermal Expansion Measurement Techniques 7

2.4 Material Properties 8

2.4.1 Young's Modulus 8

2.4.2 Stress 11

Chapter 3 Modeling of Material Properties and Devices 12

3.1 Dopant Profile Calculation 12

3.2 Stress Calculation 14

3.3 Young's Modulus 16

3.3.1 Resonant Beams 16

3.3.2 Pull-in Beams 18

3.4 Stress 21

3.4.1 Cantilever Beam Curvature 21

3.4.2 Microstrain Gauge 22

3.4.3 Buckling Strain Beams and Rings 23

Chapter 4 25

Fabrication 25

4.1 Process Flow 25

4.2 Phosphorus doping 26

4.2.1 Spin-on Process 26

4.2.2 Pre-annealing 28
4.2.3 Thermal Diffusion 30
4.2.4 Dopant concentration measurements 31
4.2.5 Reactive Ion Etching of Polysilicon 37
4.2.6 Hydrofluoric Acid Etching of Silicon Oxide 39
4.2.7 Final Devices 42
Chapter 5 Experimental Results 46
5.1 Resonant Test 46
5.1.1 Experimental Setup 46
5.2 Stress Characterization 49
5.2.1 Clamped-clamped Beam Deformation 50
5.3 Young's modulus 59
5.3.1 Clamped-clamped Beam M-Test 59
5.3.2 Clamped-clamped Beam Resonant Tests 59
5.3.3 Extracting Young's Modulus and Average Stress 63
5.3.4 Extracting Stress Gradient 70
Chapter 6 Conclusions and Future work 79
Appendix A 82
Appendix B 85
Bibliography 96

List of Figures

Figure 1. Elastic constants for single crystalline silicon versus temperature 10
Figure 2. Calculated diffusion profiles for different lengths of diffusion at 1000ºC 13
Figure 3. Stress distribution through the thickness of the polysilicon film due to dopant distribution 15
Figure 4. Resonant frequency of cantilever beams of different lengths and with different Young's moduli 17
Figure 5. Resonant frequencies of various length bridges with assumed Young's modulus of 160 GPa and average stress associated with calculated dopant profiles 18
Figure 6. Pull-in voltage for various length bridges with different values of Young's modulus with no stress 20
Figure 7. Pull-in voltage of various length bridges with different dopant distribution assuming the effective average Young's modulus is 160GPa 20
Figure 8. Out of plane deflection of cantilever beam due to dopant gradient 22
Figure 9. The displacement of the microstrain gauge associated with the residual stress of the thin film 23
Figure 10. Process flow 25
Figure 11. Wafers in quartz boat after diffusion. The two middle wafers are the required samples, the five before and after are dummy wafers 28
Figure 12. Wafers inserted into the furnace for diffusion 30
Figure 13. Wafer surface after each step of the diffusion process 31
Figure 14. Probing locations on wafer for the 4-point probe sheet resistance measurements 31
Figure 15. Wafer in the 4-point probe apparatus 32
Figure 16. Results of the 4-point probe tests of sheet resistance plotted against the doping time for six of the wafers listed in Table 7 33
Figure 17. Average electrical carrier and chemical phosphorus concentration versus the doping time 36
Figure 18. Dopant profiles predicted using the measured sheet resistance data 36
Figure 19. Chip number 38
Figure 20. Wafer after RIE 38
Figure 21. Wafer after dicing 39

Figure 22. Profilometer image of an anchor from a released device, the undercut is about 20μm 42
Figure 23. Case in which the photolithographic step was not good enough to produce 2μm features 43
Figure 24. Thin clamped-clamped beams before and after release 43
Figure 25. Cantilever beams of 2μm widths, bent in-plane... 44
Figure 26. Vernier gauge 44
Figure 27. Cantilever beams 20μm and 30μm wide 45
Figure 28. Clamped-clamped beams, 15 μm, 20 μm and 30 μm wide.. 45
Figure 29. Uncalibrated piezo shaker response 47
Figure 30. Calibrated piezo shaker response 47
Figure 31. Photograph of experimental setup 48
Figure 32. Experimental setup diagram (48) 49
Figure 33. Clamped-clamped beam set 50
Figure 34. Clamped-clamped beams chip 51
Figure 35. Three dimensional profilometer results of undoped clamped-clamped beams 52
Figure 36. Cross sections of several undoped clamped-clamped beams from profilometer results..... 52
Figure 37. Three dimensional profilometer results of clamped-clamped beams from a wafer with 0.5 hours of doping 53
Figure 38. Cross sections of several 0.5 hour doped clamped-clamped beams from profilometer results... 54
Figure 39. Three dimensional profilometer results of clamped-clamped beams from a wafer with 2 hours of doping 55
Figure 40. Cross sections of several 2 hour doped clamped-clamped beams from profilometer results 55
Figure 41. Three dimensional profilometer results of clamped-clamped beams from a wafer with 2.5 hours of doping 56
Figure 42. Cross sections of several 2.5 hour doped clamped-clamped beams from profilometer results... 57
Figure 43. Out-of-plane buckling of clamped-clamped beams versus the beam length..................... 58
Figure 44. Possible combinations of stress and Young's modulus for various doping concentrations as extracted from clamped-clamped beam buckling 59

Figure 45. Frequency response of several 250µm long clamped-clamped beams with 0 hours of doping 61
Figure 46. Frequency response of several 450µm long clamped-clamped beams with 0.5 hours of doping 61
Figure 47. Resonant frequencies of various beams from undoped, 0.5 hour, 2 hour and 2.5 hour doped polysilicon 62
Figure 48. Possible combinations of stress and Young's modulus for undoped polysilicon as extracted from clamped-clamped beam buckling and resonant tests 64
Figure 49. Possible combinations of stress and Young's modulus for 0.5 hour doped polysilicon as extracted from clamped-clamped beam buckling and resonant tests 65
Figure 50. Possible combinations of stress and Young's modulus for 2 hour doped polysilicon as extracted from clamped-clamped beam buckling and resonant tests 66
Figure 51. Possible combinations of stress and Young's modulus for 2.5 hour doped polysilicon as extracted from clamped-clamped beam buckling and resonant tests 67
Figure 52. Average Young's moduli and experimental bounds extracted using the buckling and resonant test results for different doping times 69
Figure 53. Average stress and experimental bounds extracted using the buckling and resonant test results for different doping times 70
Figure 54. Cantilever beams 71
Figure 55. Cantilever beam chip 71
Figure 56. Profilometer results for three 20µm wide cantilever beams, the longer two beams are stuck 72
Figure 57. Three dimensional profilometer results of 800µm, 700µm and 600µm undoped cantilever beams 73
Figure 58. Cross sections of 800µm, 700µm, 600µm, 500µm, 300µm and 200µm long undoped cantilever beams from profilometer results and fitted circular arcs 73
Figure 59. Three dimensional profilometer results of 800µm, 700µm, 300µm, 200µm and 100µm cantilever beams from a wafer with 0.5 hours of doping 74
Figure 60. Cross sections of 800µm, 700µm, and 200µm long 0.5 hour doped cantilever beams from profilometer results and fitted circular arcs 75

Figure 61. Three dimensional profilometer results of 800μm, 700μm and 600μm cantilever beams from a wafer with 1.5 hours of doping ... 76
Figure 62. Cross sections of 900μm, 800μm, and 700μm long 1.5 hour doped cantilever beams from profilometer results and fitted circular arcs ... 77
Figure 63. Stress gradient calculated using the circular arcs fitted to cantilever beam bending ... 78
Figure 64. Frequency response of several 250μm long clamped-clamped beams with 0 hours of doping ... 85
Figure 65. Frequency response of several 350μm long clamped-clamped beams with 0 hours of doping ... 86
Figure 66. Frequency response of several 450μm long clamped-clamped beams with 0 hours of doping ... 86
Figure 67. Frequency response of several 550μm long clamped-clamped beams with 0 hours of doping ... 87
Figure 68. Frequency response of several 250μm long clamped-clamped beams with 0.5 hours of doping ... 87
Figure 69. Frequency response of several 350μm long clamped-clamped beams with 0.5 hours of doping ... 88
Figure 70. Frequency response of several 450μm long clamped-clamped beams with 0.5 hours of doping ... 88
Figure 71. Frequency response of several 550μm long clamped-clamped beams with 0.5 hours of doping ... 89
Figure 72. Frequency response of several 650μm long clamped-clamped beams with 0.5 hours of doping ... 89
Figure 73. Frequency response of several 750μm long clamped-clamped beams with 0.5 hours of doping ... 90
Figure 74. Frequency response of several 850μm long clamped-clamped beams with 0.5 hours of doping ... 90
Figure 75. Frequency response of several 450μm long clamped-clamped beams with 2 hours of doping ... 91
Figure 76. Frequency response of several 550μm long clamped-clamped beams with 2 hours of doping ... 92

Figure 77. Frequency response of several 650μm long clamped-clamped beams with 2 hours of doping 92
Figure 78. Frequency response of a 750μm long clamped-clamped beam with 2 hours of doping..... 93
Figure 79. Frequency response of a 450μm long clamped-clamped beam with 2 hours of doping..... 93
Figure 80. Frequency response of several 450μm long clamped-clamped beams with 2.5 hours of doping 94
Figure 81. Frequency response of a 550μm long clamped-clamped beam with 2.5 hours of doping.. 94
Figure 82. Frequency response of several 650μm long clamped-clamped beams with 2.5 hours of doping 95
Figure 83. Frequency response of several 750μm long clamped-clamped beams with 2.5 hours of doping 95

List of Tables

Table 1. Young's modulus values at room temperature from literature ... 9

Table 2. Average concentration and associated stress for different diffusion times ... 15

Table 3. Fitting parameters for the M-test equations (24) ... 19

Table 4. Irregularities in dopant film and likely causes ... 27

Table 5. Pre-anneal and diffusion time for wafers ... 29

Table 6. Device layer polysilicon thickness ... 32

Table 7. Sheet resistance and resistivity of doped wafers ... 33

Table 8. Average resistivity of each wafer and the calculated average carrier and atomic concentration ... 35

Table 9. Calculated stresses and stress gradients for different diffusion times using experimental sheet resistance data ... 37

Table 10. Calibrating HF etch time to release a 30μm feature ... 40

Table 11. Anchor testing, 18 minute 49% HF release ... 41

Chapter 1
Introduction

Silicon, specifically polysilicon, has been the staple material used in MicroElectroMechanical device fabrication. While other materials have been developed, studied and utilized, polysilicon is still one of the most widely used materials for sensors and actuators. The popularity of polysilicon stems from the technology which was widely available and already well characterized at the time the field of MEMS research developed. When MEMS was a budding field, much of the work associated with silicon deposition, growth, doping, etching and other processing had been done for the use in silicon integrated circuits. Additionally, large, high-capital, facilities were already up and running, producing silicon devices efficiently, professionally and reliably. As such, polysilicon was the natural and convenient choice.

Since then, MEMS have branched out into other materials. This diversification is much needed as each application has different requirements for the mechanical, electrical and optical properties of a material. For example, MEMS designed for biological applications often need flexible membranes in order to act as micro-channels for the flow of medium containing biological agents. While harsh environments, such as combustion engines, are associated with high temperature, pressure or acidity levels, and require materials that can withstand those conditions.

Clearly, material properties play a major role in the design process of a MEMS device. However, material properties are susceptible to change due to various environmental factors as well as fabrication technique. For example, Young's modulus and coefficient of thermal expansion of polysilicon vary with the environmental temperature. A well designed device must have a predictable output for all expected environmental conditions. This means that the material properties should be well characterized for all likely conditions and this information used in the design of the device. The effect of fabrication and post-processing must also be taken into account, as Young's modulus and residual stress can be greatly impacted by variation in the fabrication process.

Fabrication steps have long been used to alter material properties. For example, polysilicon produced using the low pressure chemical vapour deposition (LPCVD) technique often has a residual compressive stress. Residual stress poses a problem in free-standing structures because it can deform

the device, for example, by causing buckling. If the device is deformed, even slightly, it will not operate as expected. If it is deformed significantly, the device may not work at all. Phosphorus doping, often used to increase the conductivity of polysilicon, also introduces tensile stress. As such, phosphorus doping is often used to relieve, or counteract, the residual compressive stress in polysilicon. Thermal annealing is used in conjunction with doping and, in fact, the two are often inseparable (as doping is often done through thermal diffusion). Assuming that the fabrication procedure is well calibrated and repeatable, and the effect of each processing step on the material properties is well characterized, one can accurately predict the resulting material properties. This information can then be used during the design phase to specify the material properties for the required application.

For sensing applications, a change of a material property due to a change in the environmental condition can make for an excellent sensing technique. For example, if the Young's modulus of a cantilever beam changes with an increase in temperature, then the resonant frequency of the beam will also change. If this effect is strong enough, this device can be used as a temperature sensor. The ability to affect the way the material reacts to an environmental change, such as temperature, using a simple and inexpensive processing step, such as doping, opens the door to numerous sensing applications. Diffusion doping might be one such inexpensive way to change the material properties of a device layer. With just one additional masking step, diffusion doping could also be used to change the properties of only certain regions of the thin film. Currently, bilayer films are used to serve a similar purpose but issues, such as delamination at high temperatures and pressures, limit the range of environments in which such devices can be used. Poor adhesion between certain materials limits the combinations of materials that can be used and hence, only a small set of effective bilayer properties is available. Doping could provide a continuous range of material property variation by changing the amount of dopant introduced into the host material, additionally avoiding the problem of delamination. Manufacturing is also simplified, as the dopant atoms can be introduced into the device layer post-fabrication which allows the costly deposition of the thin film to be outsourced to a larger facility, resulting in cost savings.

The shape of a device together with its in or out of plane deflection is often used as a sensing technique. If doping could introduce a significant amount of residual stress, or a stress gradient, that

would produce a moment to predictably deform a device layer, it could then be used to create a shape that is more sensitive to a certain environmental condition, relative to a flat device. Alternatively, if doping was used to stiffen or soften a region of a flat film, it could also be used to create a buckling or hinging point in the device. Furthermore, one could design a device where either the Young's modulus or the residual stress could vary over the device's surface.

Many parameters influence the mechanical properties of the polysilicon thin films. Anything from the grain size, fabrication technique, or material uniformity produce marked changes in the mechanical operation of the device. The environmental conditions in which the device is operating also play a large role. As the field of MEMS ventures further into uncharted territories and harsher environments it is imperative that the basic mechanical properties of thin films are not simply presumed constant under all conditions.The work detailed in this thesis focuses on characterizing the effect of phosphorus doping, specifically via the combination of a spin-on-dopant source and thermal diffusion, on the mechanical properties of polysilicon. Additionally, the feasibility of utilizing this property change as a sensing technique will be discussed. The goal of this work, is to determine whether phosphorus doping can produce significant changes in the residual stress and Young's modulus of polysilicon in a way such that the above sensor designs might be implemented. The intended final application of this research is in the field of sensors for harsh environments. Since diffusion in polysilicon begins to take place at 600°C the sensor produced using polysilicon could only work up to near this level without the dopant diffusing out of the original region(s). However, the conclusions drawn from this research will likely be applicable to other materials, such as silicon carbide, which can be used for higher temperature ranges (up to 1200°C). Since the structure of polycrystalline silicon is very similar to polycrystalline silicon carbide the trends seen in the material properties of polysilicon are transferrable to silicon carbide. As such, this work not only defines the properties of polysilicon but also serves as a prototype for higher temperature materials and devices.

Chapter 2
Literature Review

Addition of impurities to polysilicon has been thoroughly explored for the purpose of tuning the electrical characteristics of the material. The addition of boron (B) or phosphorus (P) is commonly used to make bulk single-crystal silicon and polysilicon thin films more electrically conductive. In addition to the electrical effects, these dopants also produce mechanical changes by causing residual stress (1), change in Young's modulus (2), change in the coefficient of thermal expansion (3), as well as other mechanical parameters. Many different approaches have been taken to characterize the Young's modulus of MEMS materials. However, the characterization has mostly been done for lightly doped crystalline silicon rather than heavily doped polysilicon. Additionally, since heavy boron doping is used for as an etch stop for KOH etching of silicon more work has been done on characterizing the effect of boron on the mechanical properties of silicon(4), (5), (6) rather than phosphorus.

2.1 Young's Modulus Measurement Techniques

The most direct and generally accepted way to find the Young's modulus of a material is through tensile testing; a sample is clamped to a loading apparatus and pulled from both ends until it yields. The stress versus strain for the given sample is plotted and the Young's modulus is extracted from the initial linear region of the graph before plastic deformation or yielding occurs. At the macro level, this test is standard. However, since the thin-film material properties vary from bulk material properties, one cannot use a thick sample for such a test. Hence, one of the major difficulties in performing the tensile test for thin films is the sample preparation, thin films are fragile which makes them difficult to handle. To work around this, some groups fabricated the specimen separately and then carefully attached to holders (7) which get clamped into the load cell. Other groups grow the thin film on a thick wafer and then etch away the portion of the wafer beneath the sample, creating a free standing thin film(8),(9) with holders on each side. Some groups create free-standing structures, such as cantilever beams attached to a wafer using sacrificial layers. They then use an adhesive or electrostatic force in order to attach the handle, or probe, to the thin film structure(10). Another difficulty with tensile tests of thin films is that very sensitive equipment capable of applying small forces and measuring small displacements is required. Shrape's group (8) took an interesting

approach by using an interferometric strain/displacement gauge(11) in order to measure the elongation of the material under load.

Successful attempts at replicating the macro testing techniques on-chip have been made by several groups. For the tensile test discussed above, on-chip actuation using electrostatic comb (12) or parallel-plate (13) drives has been demonstrated and is able to produce forces large enough to reach the yielding point of the specimen (12). This method avoids the use of a load cell and the force applied to the sample is related to the voltage applied to the electrostatic actuator. The force developed by electrostatic actuation can be predicted and controlled accurately enough for this application. Reliability In addition to characterizing the Young's modulus, electrostatic actuation can also be used for fatigue measurements (14), which are useful for investigating reliability, one of the major issues associated with MEMS devices. The drawback of the on-chip electrostatic actuation technique is the space required for the actuation mechanism. Additionally, as this test is destructive the devices can only be used once and any repeat measurements would require the fabrication of spare devices.

Nanoindentation and microscratch testing have been used to measure the hardness, Young's modulus and scratch resistance of single crystal and poly silicon (15),(16). A depth sensing nanoindenter has also been used on micro and nano scale beams in order to perform bending tests from which the Young's modulus and expected type of break were extracted. Notches were made in some of the beams in order to concentrate the bending stress and find the yielding stress of the material(16). Bending tests using the atomic force microscope (AFM) have been performed on microcantilevers (17) to find the Young's modulus and a stylus-type surface profiler has been used to find the Young's modulus of silicon nitride beams (18). In both these techniques, a force is applied to the tip of a cantilever beam and the associated deflection is recorded. Based on the deflection to force relation the Young's modulus can be extracted. A tactile technique where the sample is actually contacted by the probe allows for the extraction other useful parameters such as fracture toughness, scratch resistance and coefficient of friction. However, care must be taken in choosing the correct tools, such as probe tips, in order to get accurate experimental data.

Indirect measurement of Young's modulus is also possible by relating a structure's resonant frequency (19), deflection (20) or some other mechanical response to this material property. The advantage of this approach is that the space occupied by the devices is not excessive and the experiments can be carried out using only standard electrical equipment, though often more specialized equipment makes measurements easier. On-chip lateral resonators with comb-drive electrostatic actuators have been used (19), (21) to extract the Young's modulus of doped and undoped polysilicon thin films. Work has also been done with other materials, such as Ni and Al for example(22). Simple out-of-plane resonators such as cantilever beams and bridges(23) have also been used by numerous groups. The advantage of using simple structures is that there are fewer parameters that can be non-ideal, this makes the model and the extracted values more accurate. Numerical or analytical models may then be used to map the mechanical response back to the Young's modulus.

The M-test is also a very well-developed and widely used on-chip technique for extracting the Young's modulus and residual stress of the material. Devices such as cantilevers, bridges and circular plates of different sizes are fabricated atop a conductive substrate. An increasing potential is applied between the substrate and the device until a critical pull-in voltage is reached and the device collapses onto the substrate. As both the device and the substrate are conductive a current begins to flow and the pull-in voltage is easily identified electrically. Parameters related to the residual stress of the film and the Young's modulus are extracted from the pull-in voltages of a set of devices(24). Intrinsically, this method relies on the geometry of the device under test, and, as such, any fabrication uncertainties or irregularities are prone to skewing the results if not accounted for properly. Work has been done to identify possible sources of non-idealities and account for them in the model(25).

2.2 Stress Measurement Techniques

The stress of the thin film is another important quantity that must be characterized. This is necessary not only because it is an important parameter but also because the presence of a residual stress changes the effective stiffness of constrained mechanical structures and can impact the extracted Young's modulus. Residual stress in undoped LPCVD polysilicon thin films is usually compressive. Phosphorus doping is used to introduce tensile stress in order to counteract the intrinsic compressive stress. Several techniques have been used to characterize the effect of phosphorus doping on the stress polysilicon thin films. The curvature of the wafer before and after polysilicon deposition as well as

after doping has been measured and correlated to the stress in the polysilicon film(1). The solute contraction coefficient of phosphorus in single crystalline silicon(26) has been found by a similar method. An X-ray technique has also been used to find the lattice contraction coefficient (27), which closely matches results from (1).

On-chip devices have also been used to extract the pre-release residual stress by observing the in-plane deflection of specially designed devices. The residual stress is converted into strain once the sacrificial layer is removed and the device is allowed to deform. Microstrain gauges with mechanical amplifiers (28), bent-beam strain gauges (29), and ring structures(30) have been demonstrated to measure compressive and tensile stresses. Depending on the fabrication steps, the residual stress may vary through the thickness of the film creating an out-of-plane stress gradient. The curvature of cantilever beams has been used to measure the stress gradient produced in a boron doped single crystal silicon film(31),(5). Heavy boron doping is used as an etch-stop for KOH etching of silicon, and is often used to thin the wafer or create a thin membrane. As such, the stress is an important parameter to consider. Cantilever and bridge deflection has also been used to characterize the stress in phosphorus doped polysilicon beams through the use or interferometry(32). Another group has been able to extract the average as well as gradient stress by looking at the bending and curvature of cantilever beams(33). By separating the bending at the anchor from the curvature of the beam the two stress parameters can be decoupled. The deflection obtained using and optical profilometer is compared to a numerical simulation and the stress values are extracted. An analytical expression fitted to the numerical model was also presented(33).

2.3 Coefficient of Thermal Expansion Measurement Techniques

The linear coefficient of thermal expansion is an important parameter for devices that are expected to operate at a variety of temperatures or those operating using an appreciable current which could produce Joule heating. Additionally, to extract the temperature dependent Young's modulus the coefficient of thermal expansion of the material must be known in order to compensate for the elongation and associated stress due to expansion. In order to measure the thermal expansion one must heat the material and observe the expansion. Most common ways of heating the samples are using a furnace, a heat lamp or Joule heating. Readout can be done using interferometric, optical or

electrostatic means. However, temperature related electrical effects must also be considered with electrostatic readout or actuation at higher temperatures.

The stress extraction techniques described in section 2.2 can be used to find the additional stress associated with thermal expansion. The results of experiments performed at room temperature can be compared to the high temperature readings, and the difference attributed to thermal expansion. Resonant and pull-in techniques described in section 2.1 can also be used, as the effective stiffness of the beams depends on the stress which is correlated to the amount of expansion. However, the Young's modulus of silicon is known to change appreciably (34) with change in temperature; that change must also be accounted for (3). If there is a material whose mechanical properties, including the coefficient of thermal expansion, have been well characterized, a bi-layer cantilever device can be used to extract the coefficient of thermal expansion of the second material (35). The bi-layer cantilever is heated and the change in curvature is observed. From there, the difference in the coefficients of thermal expansion can be extracted and the thermal coefficient of the second material can be calculated.

Devices designed as thermal actuators can also be used to find the coefficient of thermal expansion. For example, the hot-cold arm actuator(36) and the fishbone thermal actuator(37) are both designed to convert the expansion due to Joule heating into a measureable amount of displacement. By correlating the current to the produced heat using the resistivity and thermal conductivity of the material one can extract the amount of expansion per degree by observing the device displacement.

2.4 Material Properties

2.4.1 Young's Modulus

Young's modulus of polycrystalline silicon and single crystalline silicon of different orientations has been well characterized. Additionally, the Young's moduli of single and poly crystalline silicon doped with boron and phosphorus have been found for certain concentrations and certain doping techniques. Table 1 summarizes the values found in literature. The change in Young's modulus of polysilicon with doping comes from two origins. The first is the incorporation of the dopant atoms

into the crystalline lattice of the grains, the second is the segregation of atoms along the grain boundaries.

Table 1. Young's modulus values at room temperature from literature

Reference	Young's Modulus (GPa)	Doping	Film	Extraction Technique
(16)	165	Undoped	(100) silicon	Nanoindentation
	167	undoped	Polysilicon	
(13)	143	unknown	Polysilicon, 15µm thick	On-chip tensile test
(23)	133	Boron, approximately 10^{20} atoms cm^{-3}	(100) silicon	Out-of-plane resonator
(4)	122-125±2.08	Boron, 6-9 Ωcm	(100) silicon	Tensile and resonant
(38)	200-220±20	Boron, $5\times10^{19}cm^{-3}$	(110) silicon, 2.5µm thick	Pull-in voltage
(39)	164.3±3.2	Light phosphorus	Polysilicon, 2.25 µm thick	Electrostatic actuation, interferometric readout
(19)	130±5	In-situ phosphorus, $4.5\times10^{20}cm^{-3}$	Polysilicon, 2µm thick	Lateral resonators
	160±6	In-situ phosphorus, $2.5\times10^{20}cm^{-3}$		
(2)	162.6±0.6	$POCl_3$, 7.34 Ω/□	Polysilicon deposited at 605ºC, 2µm thick	Lateral resonators
	161.9±2.3	$POCl_3$, 6.97 Ω/□		
	163.1±0.4	$POCl_3$, 6.40 Ω/□		
	161.2±2.0	$POCl_3$, 4.41 Ω/□		
	155.6±5.6	$POCl_3$, 3.66 Ω/□		
	161.8±1.4	$POCl_3$, 3.59 Ω/□		
	157.1±3.7	$POCl_3$, 2.86 Ω/□		
	156±5.9	$POCl_3$, 2.6 Ω/□		

Unfortunately, the existing data on the effect of doping on the Young's modulus of silicon is scattered and even inconsistent between sources. This is to be expected, as the fabrication process in each of the sources is independent of each other and even small inconsistencies between two processes can change the Young's modulus of a thin film, let alone major differences in critical steps. The dopant source varies widely between works; in-situ, liquid source, gas source, contact source. The temperature, ambient gas, and annealing time also vary. The film fabrication technique, thickness and Young's modulus extraction method are different as well. The best source for characterizing the effect of phosphorus doping on Young's modulus has been the work done by Lee et al. (2). A variety of dopant concentrations were used, a consistent fabrication procedure and a simple Young's modulus extraction technique was employed.

The temperature dependence of the elastic constants for single crystalline silicon has been well characterized and the data is presented in Figure 1 (34). Equation 1- Equation 3 (34) show the numerical fit to the experimental data used to produce the graph in Figure 1.

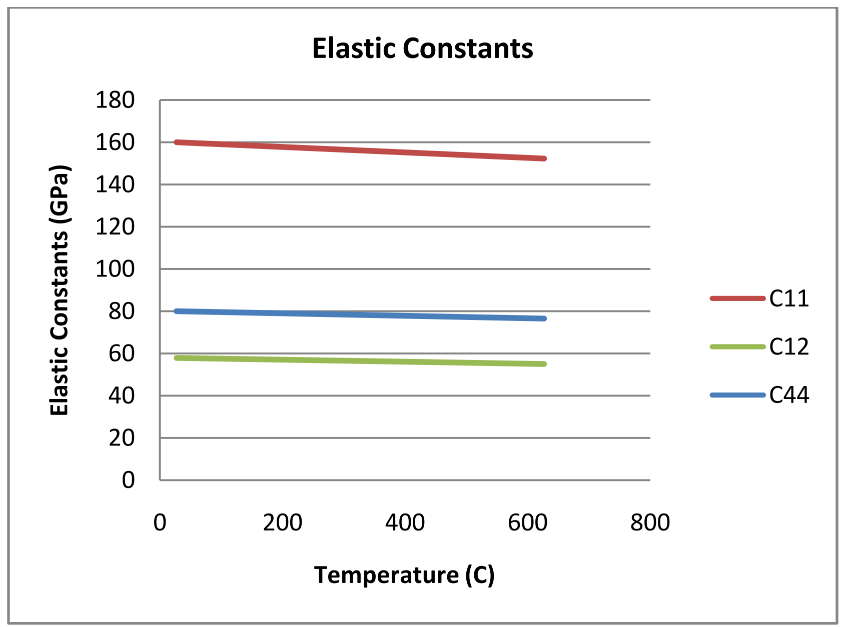

Figure 1. Elastic constants for single crystalline silicon versus temperature

$$C_{11} \cong 16.38 - 0.0128T \quad \text{Equation 1}$$

$$C_{12} \cong 5.92 - 0.0048T \quad \text{Equation 2}$$

$$C_{44} \cong 8.17 - 0.0059T \quad \text{Equation 3}$$

In order to calculate the Young's modulus of polysilicon the Voigt or Reuss volume average can be used, so the trends in C_{11}, C_{12} and C_{44} are transferable to the expected trend in polysilicon's Young's modulus.

2.4.2 Stress

Stress due to doping in polysilicon is produced by the atoms incorporated in the crystalline lattice as well as those remaining along the grain boundaries. The radius of the phosphorus atom is 1.07Ǻ and that of a silicon atom is 1.176Ǻ. Due to this mismatch, the atoms incorporated into the lattice produce tensile stress in the material(27). The solute lattice contraction coefficient of phosphorus is silicon is $\beta_{P\text{-}Si} = 1\times10^{-24}$ cm^3/atom (26). The more silicon atoms are substituted by phosphorus the higher the amount of contraction and hence, the higher the induced stress. The effect of the dopant atoms found along the grain boundary is more challenging to ascertain, a possible way to find that effect is suggested in Chapter 6. It has been suggested that the dopant atoms along the grain boundaries introduce compressive stress into the polysilicon(40) which counteracts the tensile stress in the grains. Hence, the distribution of atoms in the material is important in determining the residual stress.

Chapter 3
Modeling of Material Properties and Devices

3.1 Dopant Profile Calculation

Phosphorus diffusion in single crystalline silicon occurs via two mechanisms, vacancy and interstitialcy, though interstitialcy dominates (41). For polysilicon, diffusion additionally occurs along the grain boundaries (42) and the diffusivity along grain boundaries can be up to 100 times larger than in crystalline silicon. The diffusivity constant for polysilicon diffusion at 1000°C has been experimentally determined to be between 6.9×10^{-13} cm^2/s and 63×10^{-13} cm^2/s (41). As the grain structure of polysilicon depends on the deposition conditions and processing techniques, this value can only be used as an estimate since the polysilicon used in this work has undergone a different fabrication process.

Given that the diffusion discussed herein occurs at 1000°C from a high concentration dopant source, see section 4.2, we can use the constant surface concentration assumption to calculate the dopant profile, Equation 4 (41). With heavy phosphorus doping, concentration dependent diffusivity must also be considered. The diffusivity, D, is constant for low dopant concentrations but becomes concentration dependent when the dopant concentration is high. Fair and Tsai (43) investigated the effect of concentration dependent diffusivity and produced a mathematical model to fit the available empirical results, Equation 4 - Equation 8 (43). Equation 5 describes the diffusivity constant at high concentrations and Equation 6 - Equation 8 are the associated empirically determined variables.

$$C(x,t) = C_s erfc\left(\frac{x}{2\sqrt[2]{Dt}}\right) \quad \text{Equation 4}$$

$$D = h\left[D_i^x + D_i^= \left(\frac{n}{n_i}\right)^2\right] \quad \text{Equation 5}$$

$$D_i^x = 3.85 exp\left(\frac{-3.66}{kT}\right) \quad \text{Equation 6}$$

$$D_i^{=} = 44.2exp\left(\frac{-4.37}{kT}\right) \quad \text{Equation 7}$$

$$h = 1 + \frac{n}{n_i}\left[\left(\frac{n}{2n_i}\right)^2 + 1\right]^{-\frac{1}{2}} \quad \text{Equation 8}$$

Where C_s is the surface dopant concentration, x is the depth, D is the diffusion constant, t is the diffusion time, k is the Boltzmann constant and T is the diffusion temperature. Equation 4 describes the concentration of dopant at a certain depth in the film, x, after a diffusion time, t. This equation is valid in the case of a constant surface concentration of dopant, which is applicable to the diffusion method used. It was assumed that solid solubility was reached at the surface of the film (44).

Using the technique and model presented in Fair and Tsai's paper (43) diffusion profiles for the 3-region phosphorus diffusion were calculated and are shown in Figure 2. The high concentration, kink and tail regions characteristic of phosphorus diffusion in silicon can be clearly seen in the profiles.

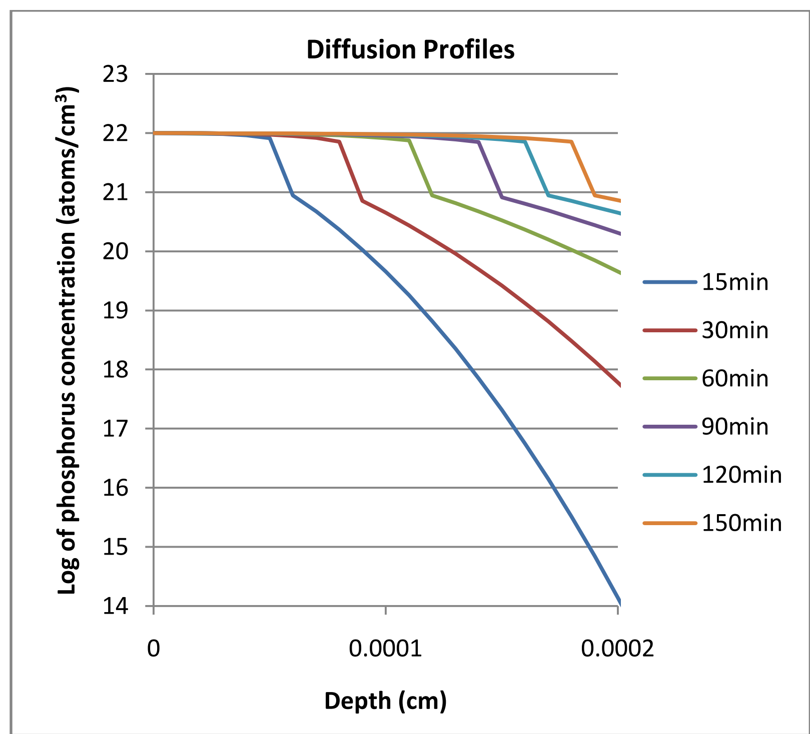

Figure 2. Calculated diffusion profiles for different lengths of diffusion at 1000ºC

As concentration dependent material properties are being investigated, it must be noted that the concentration gradient through the polysilicon layer also entails a gradient in the Young's modulus and residual stress.

3.2 Stress Calculation

Introduction of phosphorus atoms into the silicon crystalline lattice causes the lattice to contract. This contraction results in a tensile stress, proportional to the dopant concentration being introduced into the thin film. The induced stress can be calculated using Equation 9 (27).

$$\boldsymbol{\sigma = \beta \cdot C \cdot E} \qquad \text{Equation 9}$$

Where β is the lattice contraction coefficient, 1.8×10^{-24}, for phosphorus in silicon, C is the phosphorus concentration in the grains and E is the Young's modulus. Dopant atoms are also found in the grain boundaries and are expected to have an effect on the residual stress. It is expected that the atoms in the grain boundaries would introduce compressive stress. However, the magnitude of the tensile stress is expected to be much larger, thus, the overall induced stress should be tensile. As discussed earlier, the effect is difficult to predict from literature, due to that, the effect of the atoms in the grain boundaries has been neglected. The calculated dopant concentrations after diffusion, shown in Figure 2, are not uniform through the thin film, indicating that the induced stress will also vary through the thickness. Figure 3 shows the expected stress associated with the dopant profiles for the different diffusion times calculated using Equation 9 and assuming a Young's modulus of 160GPa.

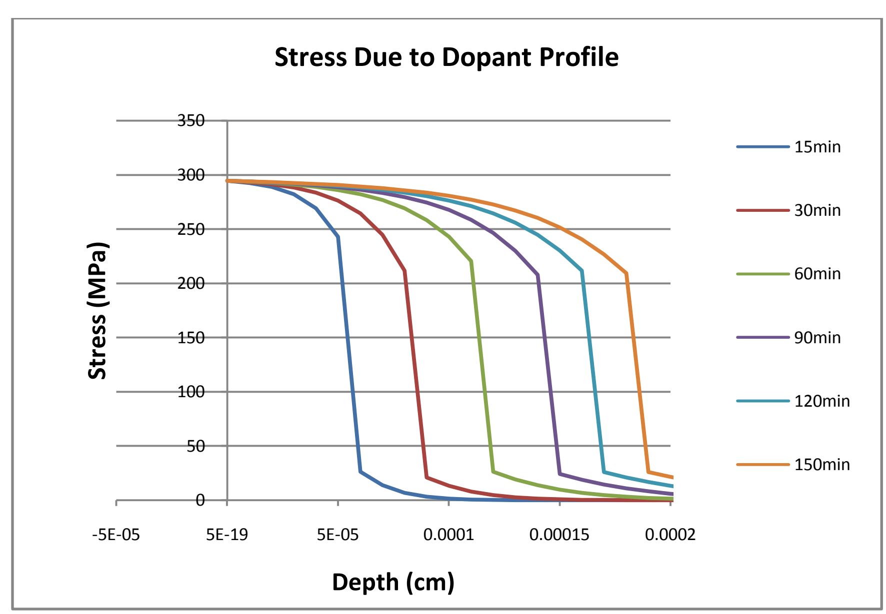

Figure 3. Stress distribution through the thickness of the polysilicon film due to dopant distribution

From the expected stress distribution, the average stress and the stress gradient can be calculated, and are presented in Table 2. These values can be used in the lumped model for calculating the pull-in voltage as well as the resonant frequencies of the test beams.

Table 2. Average concentration and associated stress for different diffusion times

Diffusion time (min)	Average Concentration (atoms/cm^3)	Average Stress (MPa)	Stress Gradient (MPa)
15	1.1694×10^{21}	86.1	294.40
30	1.6977×10^{21}	124.9	294.38
60	2.2987×10^{21}	169.1	293.06
90	2.8411×10^{21}	208.4	288.36
120	3.2369×10^{21}	236.1	281.20
150	3.6132×10^{21}	261.7	272.99

3.3 Young's Modulus

In order to properly size the devices and accurately predict their responses an approximate expected value of the Young's modulus at various dopant concentrations should be known. Literature provides scattered accounts of the effect of phosphorus doping on the Young's modulus of thin polysilicon films. The deposition, doping, and material property extraction process varies from paper to paper. Additionally, the range of dopant concentrations studied per work is usually not large. Comparing data between papers can be prohibitive as the processing varied. As such, it is difficult to predict the expected Young's modulus any more accurately than simply providing an estimated range. The trend presented in literature indicates that the Young's modulus decreases with an increase in phosphorus concentration, though inverse trends were also reported, with the lowest reported value around 130 GPa and highest around 170GPa. As such, the range of 120-180GPa has been chosen as the target. However, devices sensitive to values above and below the predicted range have also been fabricated.

3.3.1 Resonant Beams

The resonant frequency of cantilever beams can be used to extract the Young's modulus. As the cantilever beams are free to deform once the sacrificial layer is etched away they elongate and curl in order to alleviate the residual stress. The elongation is negligible compared to the original length of the beam and does not affect the resonant frequency significantly.

Since the expected residual stress gradient is rather high, the beam curvature is expected to be significant enough to make electrostatic actuation and extraction of the pull-in voltage inaccurate (24). Due to this, the cantilever devices will be attached to a piezoelectric shaker and the beams will be actuated mechanically. In addition to avoiding uneven electrostatic force, mechanical actuation also allows the tests to be performed at higher temperatures. Electrical readout can degrade at higher temperatures but mechanical actuation with optical readout will be functional up to the shaker's maximum allowable temperature. The Young's modulus can be extracted from the resonant frequency by assuming ideal conditions and using Equation 10.

$$f_0 = 0.162 \frac{t}{L^2} \sqrt{\frac{E}{\rho}} \qquad \text{Equation 10}$$

Where ρ is the density, t is the thickness, L is the length, and f_0 is the resonant frequency. Figure 4 shows the change in the resonant frequency with change in the Young's modulus for beams of different lengths.

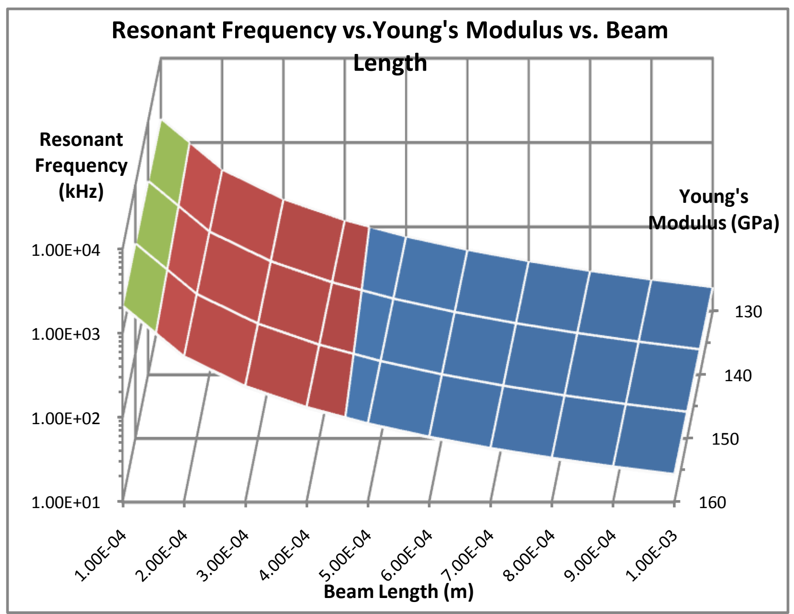

Figure 4. Resonant frequency of cantilever beams of different lengths and with different Young's moduli

The resonant frequency of clamped-clamped beams can be used to extract the average residual stress once the effective Young's modulus is known. Since the clamped-clamped beams are constrained at both sides the elongation or contraction produces stress in the structure and softens or stiffens the beam. The resonant frequency of a clamped-clamped beam can be found analytically using Equation 11(23). The effect of stress on the resonant frequency can be accounted for by introducing another term, as shown in Equation 12(23).

$$f_0 = 1.028\frac{t}{L^2}\sqrt{\frac{E}{\rho}} \qquad \text{Equation 11}$$

$$f_{0\,stress} = f_0\sqrt{\left(1+\frac{B\sigma L^2}{Et^2}\right)} \qquad \text{Equation 12}$$

Where B= 0.295 and σ is the average stress value. Once the Young's modulus is extracted from the resonant tests of cantilever beams it can be used to extract the average residual stress from the clamped-clamped beam resonant tests. Figure 5 shows the change in the resonant frequency of clamped-clamped beams due to the expected stresses calculated in section 3.2, presented in Table 2. Since the expected stress is tensile the effective Young's modulus increases thereby increasing the resonant frequency.

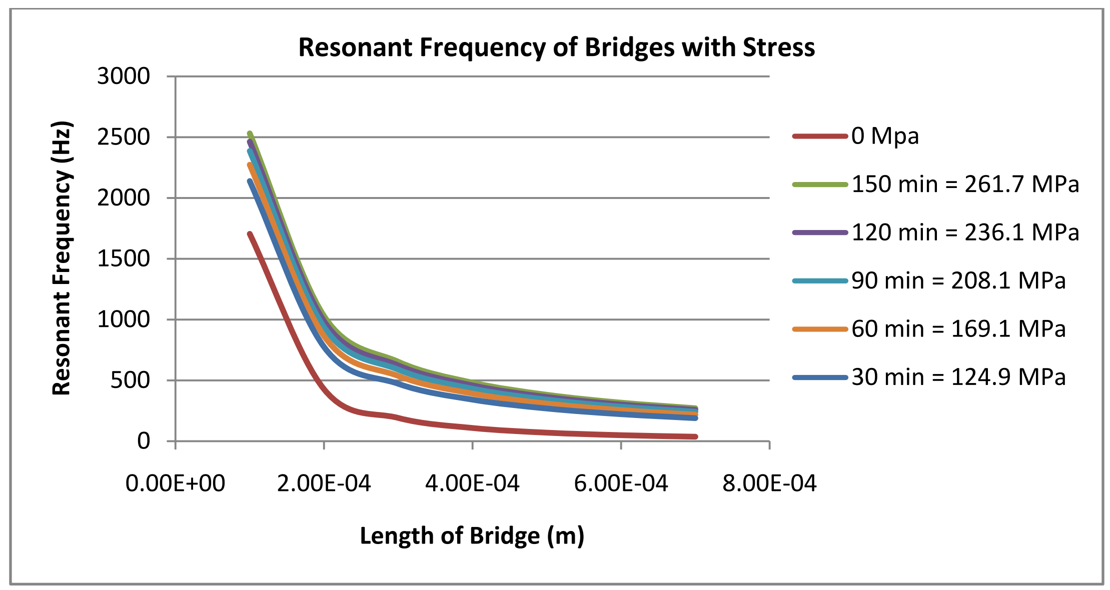

Figure 5. Resonant frequencies of various length bridges with assumed Young's modulus of 160 GPa and average stress associated with calculated dopant profiles

3.3.2 Pull-in Beams

Following the procedure outlined by the widely-used M-test (24), clamped-clamped bridge structures were designed to fit the expected range of Young's moduli and stress values. The M-test is performed by applying an increasing DC voltage between the structure, clamped-clamped beam in this case, and the substrate. When the structural stiffness of the device is overcome by the electrostatic force that is developed between the substrate and the beam, the beam collapses onto the substrate and a current begins to flow between the two conductors. This current can be measured and used as a clear sign of pull-in. Equation 13 describes the relationship between the pull in voltage and the stress and Young's modulus related parameters, S and B respectively, which are defined in Equation 16 and Equation 17.

$$V_{pull-in} = \sqrt{\frac{\gamma_{1n} S}{\varepsilon_0 L^2 D_n \left[1 + \gamma_{3n} \frac{g_0}{w}\right]}} \quad \text{Equation 13}$$

Where

$$D_n = 1 + \frac{2\left\{1 - cosh\left(\frac{\gamma_{2n} kL}{2}\right)\right\}}{\left(\frac{\gamma_{2n} kL}{2}\right) sinh\left(\frac{\gamma_{2n} kL}{2}\right)} \quad \text{Equation 14}$$

And

$$k = \sqrt{\frac{12S}{B}} \quad \text{Equation 15}$$

$$S = \tilde{\sigma} t g_0^3 \quad \text{Equation 16}$$

$$B = \tilde{E} t^3 g_0^3 \quad \text{Equation 17}$$

Where $\tilde{\sigma}$ and $\tilde{E}$ are the effective stress and Young's modulus, g_0 is the initial air gap, L is the length of the beam and ε_0 is the permittivity of air. The numerically derived fitting parameters, γ_{1n}, γ_{2n}, γ_{3n}, are outlined in Table 3.

Table 3. Fitting parameters for the M-test equations **(24)**

Numerical Constant	n=1, Cantilever Beams	n=2, Clamped-clamped Beams
γ_{1n}	0.07	1.55
γ_{2n}	1.00	1.65
γ_{3n}	0.42	0.00

Figure 6 shows the predicted pull-in voltages of various length clamped-clamped beams for different expected values of Young's modulus assuming no residual stress.

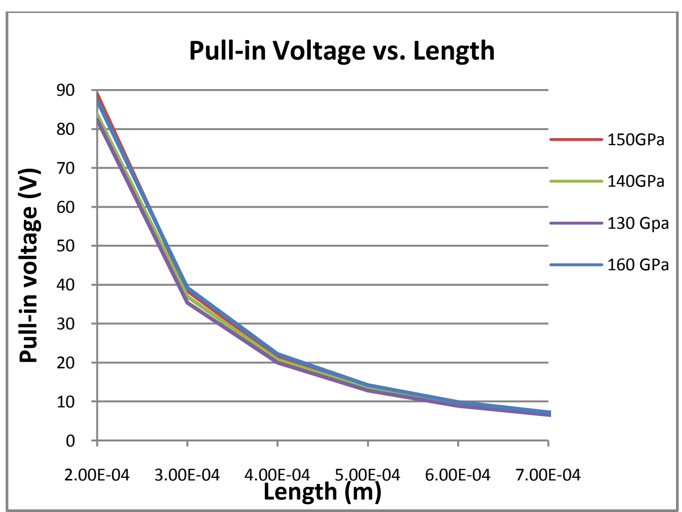

Figure 6. Pull-in voltage for various length bridges with different values of Young's modulus with no stress

The graph above shows that the shorter beams are more sensitive to the change in Young's modulus, however, they require higher actuation voltages. In order to make the model more accurate, average stress is incorporated. Figure 7 shows the variation of the pull-in voltage with beam length for beams with the expected average stresses from Table 2.

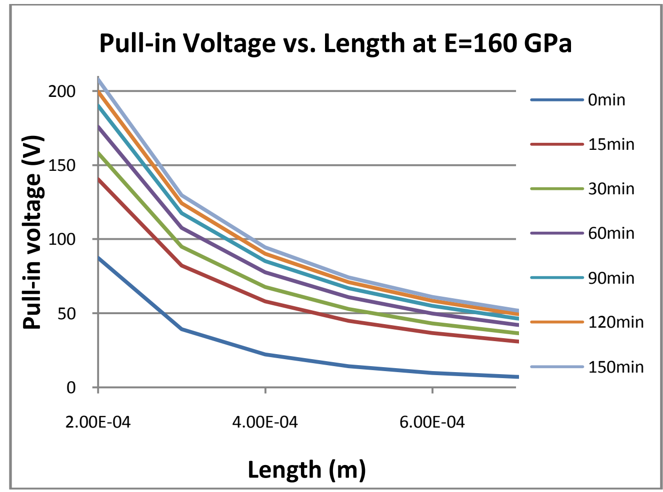

Figure 7. Pull-in voltage of various length bridges with different dopant distribution assuming the effective average Young's modulus is 160GPa

It is evident from Figure 7 that residual tensile stress stiffens the structure and increases the pull-in voltage.

3.4 Stress

The residual stress in diffusion doped polysilicon has two components that need to be characterized, the average stress and the stress gradient. All the presented techniques for characterizing the stress rely on the conversion of the film stress to strain once the supporting sacrificial layer is removed. The deformation that occurs is measured and correlated back to the original stress value.

3.4.1 Cantilever Beam Curvature

Using a volumetric change approach, the deflection of the cantilever beam, d, at length x, due a linearly changing dopant distribution through the thickness of the film can be calculated using Equation 18(4).

$$d = \frac{(N_t - N_b)(R_{Si} - R_P)x^2}{[R_{Si}N_{Si} - (N_t + N_b)(R_{Si} - R_P)]t} \qquad \text{Equation 18}$$

Where N_t and N_b are the concentrations of phosphorus at the top and bottom of film respectively, t is the thickness of the film. R_{Si} and R_P are the atomic radii of silicon and phosphorus and N_{Si} is the intrinsic silicon concentration. Figure 8 shows the calculated deflection of cantilever beams of different length with stress gradients associated with the calculated doping profiles in Figure 2.

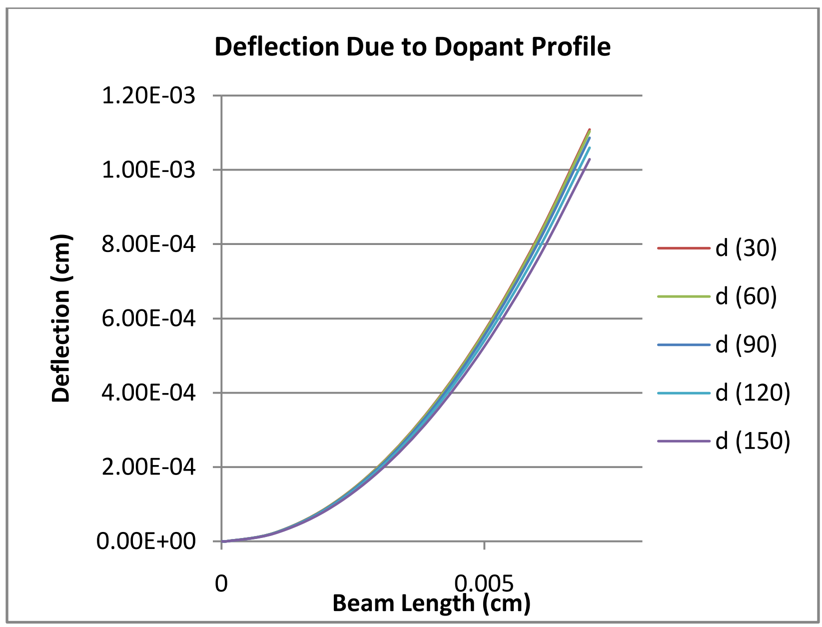

Figure 8. Out of plane deflection of cantilever beam due to dopant gradient

The stress gradient, σ_g, can be extracted from the radius of curvature of the beam, ρ, using Equation 19 (45).

$$\sigma_g = \frac{Ed}{\rho} \qquad \text{Equation 19}$$

3.4.2 Microstrain Gauge

On-chip microstrain gauges (28) can be used to obtain the average compressive or tensile stress of the thin film. Equation 20 (28) describes the relation between the displacement of the gauge tip and the residual stress.

$$\boldsymbol{\sigma} = \frac{2L_{sb}\delta_v}{3L_{tb}L_{ib}\left(\frac{1-\left(\frac{W_{ib}}{L_{sb}}\right)^2}{1-\left(\frac{W_{ib}}{L_{sb}}\right)^3}\right)} \qquad \text{Equation 20}$$

Where L_{sb} is the length of the slope beam, L_{ib} is the length of the indicator beam, L_{tb} the length of the test beam and w_{ib} is the width of the indicator beam (28). The stress can be accounted for and used to extract the Young's modulus as well as to predict the average doping concentration, hence, verifying the dopant distribution model. Figure 9 shows the calculated displacement associated with residual stresses in the range produced by the doping.

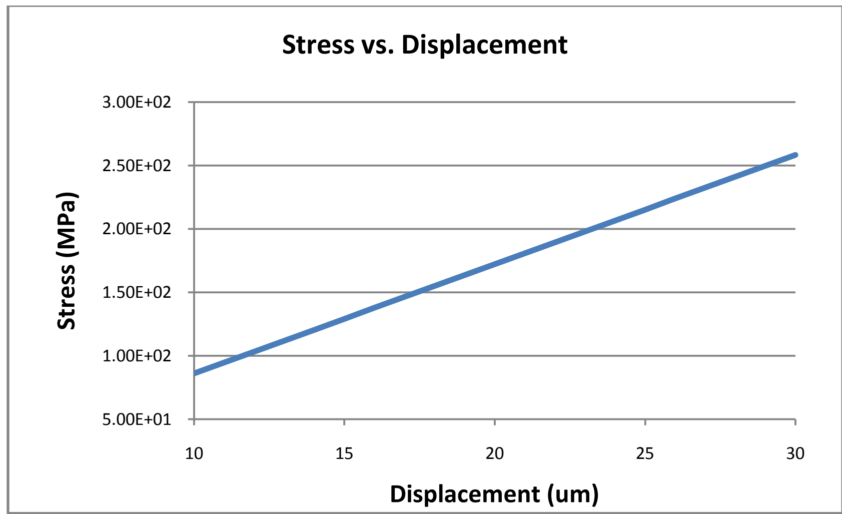

Figure 9. The displacement of the microstrain gauge associated with the residual stress of the thin film

The stress produces a displacement that is large enough to read using a regular microscope.

3.4.3 Buckling Strain Beams and Rings

Clamped-clamped beams of different lengths are fabricated and observed after release. The devices deform due to residual stress and those longer than the critical length for a given stress buckle. By finding the critical length for buckling of beams one can extract the compressive stress using Equation 21 (30).

$$\sigma = E\frac{\pi^2}{3}\left(\frac{t}{L_{critical}}\right)^2 \qquad \text{Equation 21}$$

Once buckled, the amount of out-of-plane deflection can also be used to find the compressive stress using Equation 22.

$$\sigma = \frac{E\pi^2}{12L^2}(3d^2 + 4t^2) \quad \text{Equation 22}$$

Since tensile stress will not cause beams to buckle rings are used in order to extract the tensile stress. The strain ring and beam structures proposed by Guckel et. al. (30) allow for measurement of tensile stress. The structure converts the tensile stress into compressive and causes buckling based on Equation 23 (30).

$$\sigma = \frac{E(kR)^2\left(\frac{t}{R_{critical}}\right)^2}{12g} \quad \text{Equation 23}$$

Where $R_{critical}$ is the critical radius for bucking, R is the average radius of the inner and outer part of the ring, t is the film thickness and g is the conversion efficiency ratio for tensile strain to compressive strain conversion.

Chapter 4

Fabrication

For the fabrication process, 25 n-type phosphorus doped wafers were purchased from Silicon Valley Microelectronics Inc. The supplier grew 2µm of wet thermal oxide at just above 1000ºC followed by LPCVD deposition of 2µm of undoped polysilicon at 600ºC. The wafer structure is similar to silicon on insulator (SOI) wafers, except, the device layer is polysilicon instead of single crystalline silicon. The devices for material characterization were produced from the polysilicon layer. The thermal oxide acted as an anchor connecting the polysilicon devices to the substrate as well as an electrical isolator from the substrate. In order to get free-standing structures, portions of the oxide beneath the devices was etched, so, the oxide also acted as a sacrificial layer. The fabrication process is described in further detail in the following subsections and in Figure 10.

4.1 Process Flow

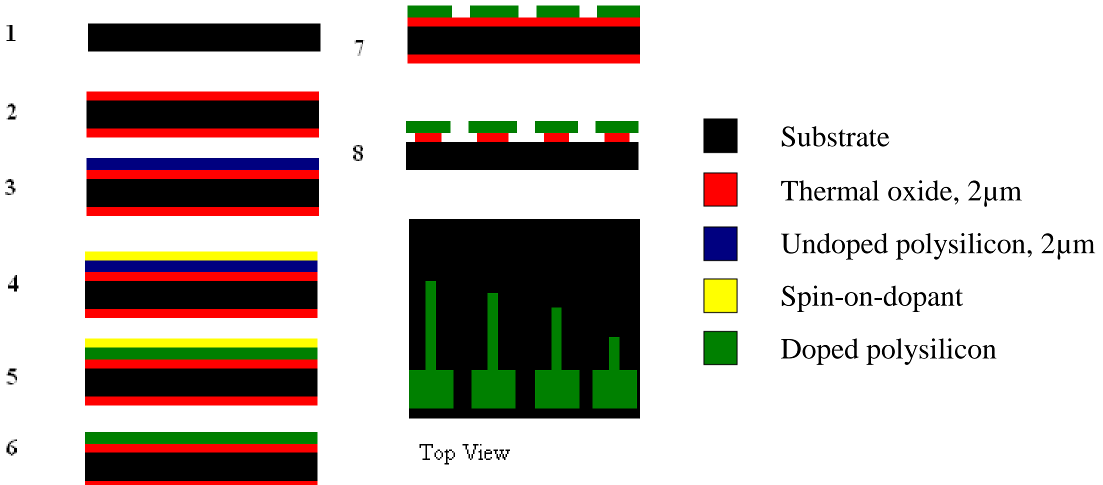

Figure 10. Process flow

Step 1, the process starts with a doped silicon wafer which is used as a mechanical support and will also be used for electrostatic actuation of the devices. Step 2, 2µm of wet thermal oxide is grown on the wafer at just above 1000°C. The oxide is used to mechanically connect the polysilicon to the

substrate and also to electrically isolate it. Step 3, 2µm of LPCVD polysilicon is deposited at 625ºC on the polished side of the wafer, the polysilicon is not doped.
In Step 4, the Filmtronics P512 spin-on-dopant is spun on and hard-baked at 200ºC for 15 minutes. Then, in step 5, the wafer is placed in a diffusion furnace at 1000ºC for a pre-determined amount of time in an atmosphere of 75% N_2 and 25% O_2. The amount of doping time for each wafer differs, this produces several samples with varying average dopant concentrations. In order to keep the thermal budget of all the wafers the same, and avoid possible changes of mechanical properties due to this parameter, each sample is pre-annealed prior to the dopant application. Therefore, each sample spends the same amount of time in the furnace.

The resulting PSG film is removed in step 6 using a 1% HF dip and the doped polysilicon is patterned with RIE in step 7. The wafer is then diced and in step 8 the structures are released by removing the oxide using 49% HF. The HF etches the oxide isotropically, each device is connected to an anchor plate large enough for a significant amount of the oxide underneath it to remain connected to the substrate.

4.2 Phosphorus doping

Thermal diffusion from a spin-on dopant source was used to introduce phosphorus into the device layer of the wafers. The dopant source used was P512 from Filmtronics, which is a combination of water, ethanol, SiO_2 and 12% phosphorus concentration.

4.2.1 Spin-on Process

Prior to spin-on the wafers were heated on a hot plate for 5 minutes at 200˚C in order to remove any moisture and prepare the surface for proper spin-on-dopant adhesion. In order to get a uniform layer on the wafer the spinning process was optimized. The dispense and spin parameters were varied in order to produce the most uniform coating possible. Spinner with a vacuum chuck was used, it was found that 5000 rpm was the optimal spin speed, which falls in the recommended 3000-6000rpm range that the manufacturer provides. Stationary dispense was used to apply 2 mL of the spin-on-dopant to the wafer.

The spun wafers were then baked on hot plate for 15 minutes at 200˚C in order for most of the water and ethanol in the mixture to evaporate, producing a solid dopant coating. It was noted that the resulting coating had certain irregularities such as radial striations, particles and pinpoint vacancies. Table 4 shows pictures of these irregularities and the likely causes.

Table 4. Irregularities in dopant film and likely causes

Irregularity	Image	Possible Cause
Radial Striations		Spin-on-dopant may have incorporated some moisture from the air causing the viscosity of the solution to change.
Particles		No exhaust on the spinner causing drops of dopant to dry in air and fall back onto wafer during spin.
Pinpoint Vacancies		Inadequate volume of dopant dispensed.

While many irregularities were eliminated with calibration of the spin-on technique and others were greatly reduced in frequency of occurrence or severity of presentation, the film was still not considered uniform enough to be the sole dopant source. In order to minimize the effects of the uneven dopant distribution, a secondary dopant source was introduced. Ten phosphorus doped dummy wafers were coated with the spin-on-dopant, using the same procedure as outlined above, and

used as solid sources during diffusion. These source wafers were placed ahead and behind the device wafers on the quartz boat to provide a phosphorus, P_2O_5, filled ambient. Figure 11 shows the ten dummy wafers and two sample wafers arranged in the quartz boat after diffusion. Though the irregularities in the dopant layer on the device wafers exist, the gaseous form of the phosphorus from the source wafers should compensate for spots where the spin-on-dopant layer is thinner. This brings the doping environment closer to the infinite source assumption as phosphorus should always be available at the surface of the device layer.

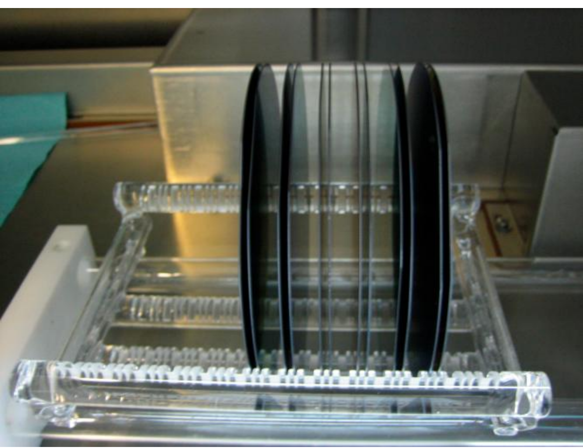

Figure 11. Wafers in quartz boat after diffusion. The two middle wafers are the required samples, the five before and after are dummy wafers

4.2.2 Pre-annealing

The distribution and concentration of the dopant atoms introduced by thermal diffusion depend on several factors. Two of the most important ones are diffusion temperature and diffusion time. The temperature of diffusion was kept constant from the diffusion of one wafer to the next, as such, the time had to be varied in order to obtain different dopant concentrations in different wafers. However, this meant that the concentration of phosphorus in the polysilicon was related to the time the wafer spent in the furnace at a high temperature. Ideally, the dopant concentration should be independent of any other processing parameter such that the effects of other processes cannot be erroneously attributed to the presence of phosphorus in the polysilicon. Annealing polysilicon at high temperature changes the properties of the material. For example, high temperature annealing leads to stress relaxation and grain growth which, in turn, affect the mechanical properties (2).

In order to decouple the phosphorus concentration from the time spent at a high temperature the wafers were pre-annealed. The wafers which were to have the lowest dopant concentration were pre-annealed longest and those that were to have the highest dopant concentration were pre-annealed for a shorter amount of time. This resulted in all wafers spending an equal amount of time in the furnace overall, with about five minutes possible variation due to loading and unloading time. Table 5 contains the details of the pre-annealing and doping times and temperatures for each wafer. The temperature of the furnace was 700ºC when the wafers were inserted or removed for pre-annealing in order to avoid oxidation upon contact with the ambient outside the furnace. The temperature was ramped up to 1000ºC and maintained for the required amount of time and then ramped down again to 700ºC before the wafers were taken out. The ramp-up and ramp-down was not required for the diffusion step as the spin-on-dopant protected the polysilicon surface from oxidation.

Table 5. Pre-anneal and diffusion time for wafers

Wafer number	Pre-anneal time (hr)			Diffusion time at 1000˚C (hr)	Total time (hr)
	700˚C ↑1000˚C	1000˚C	1000˚C ↓700˚C		
1, 2	0	0	0	0	3.0 at 1000˚C + 0.25 at 700˚C ↑1000˚C + 0.75 1000˚C ↓700˚C
3, 4	0.25	2.5	0.75	0.5	3.0 at 1000˚C + 0.25 at 700˚C ↑1000˚C + 0.75 1000˚C ↓700˚C
5, 6	0.25	2.0	0.75	1.0	3.0 at 1000˚C + 0.25 at 700˚C ↑1000˚C + 0.75 1000˚C↓700˚C
7, 8	0.25	1.5	0.75	1.5	3.0 at 1000˚C + 0.25 at 700˚C ↑1000˚C + 0.75 1000˚C ↓700˚C
9,10	0.25	1.0	0.75	2.0	3.0 at 1000˚C + 0.25 at 700˚C ↑1000˚C + 0.75 1000˚C ↓700˚C
11,12	0.25	0.5	0.75	2.5	3.0 at 1000˚C + 0.25 at 700˚C ↑1000˚C + 0.75 1000˚C↓700˚C

It must be noted that the pre-annealing took place in a 100% N_2 atmosphere while the diffusion was done in 75% N_2, 25% O_2. Pre-annealing was done in a nitrogen atmosphere to prevent oxidation as the wafers were not yet coated with dopant at that stage. Figure 12 shows the wafers in the quartz boat being inserted into the furnace for diffusion. After the pre-anneal, the wafers were dipped in 1% HF solution until they became hydrophobic in order to remove any oxide that may have formed. The diffusion of phosphorus is about 30 times slower through oxide than polysilicon (46) and a layer of

oxide between the dopant and the device layer could slow down the diffusion by preventing the phosphorus atoms from reaching the polysilicon. An additional concern was the amount of polysilicon that would have been used by the formed oxide had the diffusion been done in the presence of oxygen. That portion would have been removed during the HF dip, thinning the device layer. Since the pre-annealing time varies between the wafers there would be an inverse relation between polysilicon thickness and dopant concentration, possibly leading to erroneous conclusions.

Figure 12. Wafers inserted into the furnace for diffusion

4.2.3 Thermal Diffusion

The dopant coated sample wafers were placed on a quartz boat with 3/32” seperation with the device side facing away from the gas flow. Five source wafers were placed on either side of the sample wafers facing the sample wafers and the boat was placed in the furnace. The ambient was 75% N_2 and 25% O_2 and the temperature was 1000˚C. The diffusion times can be found in Table 5. Figure 13, below, shows the surface of a wafer after each of the steps undergone during diffusion. Figure 13 (d), the post-diffusion polysilicon, shows a smooth, even surface without irregularities and looks similar to Figure 13 (a), the pre-diffusion polysilicon. This implies that the doping process has not damaged the surface of the polysilicon. In general, thermal diffusion causes minimal damage to the material as opposed to ion implantation where the surface is bombarded with high energy particles.

Given the high temperature at which the diffusion took place, the possibility of re-crystallization of the polysilicon should be considered. TEM could be used to check for grain size and X-ray crystallography could be used to find the crystal orientation. Since crystalline silicon has highly direction dependent mechanical properties, this information would be quite useful.

Wafer surface before diffusion (a)	Wafer surface after spin-on (b)	Wafer surface after diffusion (c)	Wafer surface after HF dip (d)

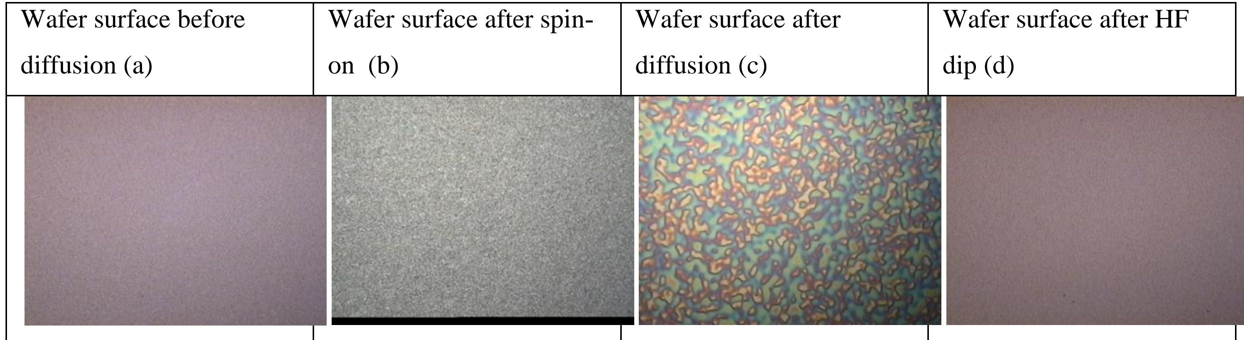

Figure 13. Wafer surface after each step of the diffusion process

4.2.4 Dopant concentration measurements

After diffusion, the wafers were dipped into 1% HF until they were hydrophobic, indicating the oxide had been removed. A 4 point probe was used the measure the sheet resistance of the wafers at the center and four additional radial points, as illustrated in Figure 14. Figure 15 shows the wafer about to be probed using the 4 point probe apparatus.

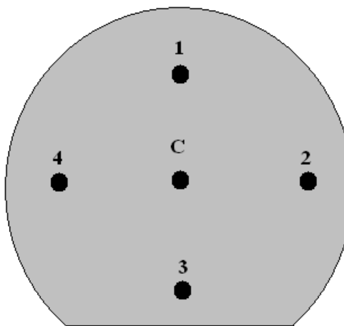

Figure 14. Probing locations on wafer for the 4-point probe sheet resistance measurements

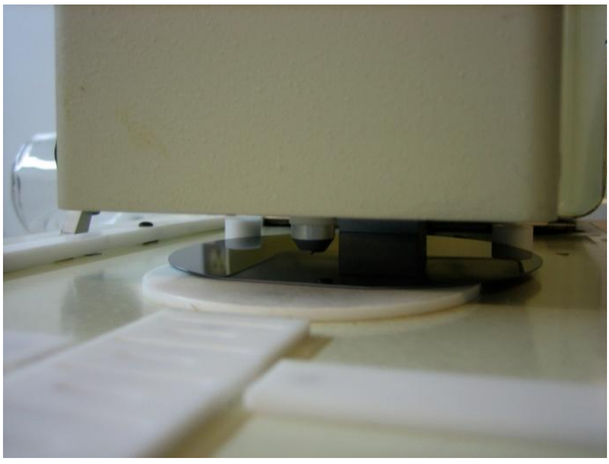

Figure 15. Wafer in the 4-point probe apparatus

In order to calculate the resistivity from the sheet resistance the thickness of the polysilicon was measured using the Nanospec 4000 scanning UV ellipsometer. For this measurement, it was assumed that the thermal oxide beneath the polysilicon is, in fact 2µm as the manufacturer specified. Since the oxide was grown thermally, which is a well known and very controllable process, this assumption should be valid. Table 6 shows the results for the measured polysilicon thickness.

Table 6. Device layer polysilicon thickness

Wafer	Thickness (µm)
1	2.0267
2	2.0346
3	2.0530

As the thicknesses varied only slightly between the measured wafers and since all the wafers were processed in the same batch it is assumed that the other wafers will be of approximately the same thickness. Additionally, thickness values provided by the manufacturer agreed closely to the measured values. Table 7 shows the sheet resistance values obtained by the 4 point probe method and the average resistivity for the wafer assuming 2µm thick polysilicon, calculated using Equation 26. Figure 16 shows the average sheet resistance plotted versus the doping time.

Table 7. Sheet resistance and resistivity of doped wafers

Wafer	Doping Time (min)	Sheet Resistance at center (Ω/□)	Sheet Resistance at 1 (Ω/□)	Sheet Resistance at 2 (Ω/□)	Sheet Resistance at 3 (Ω/□)	Sheet Resistance at 4 (Ω/□)	Average Sheet Resistance (Ω/□)	Average Resistivity (Ω/cm)
10	0	9.15×10^{7}	9.15×10^{7}	9.15×10^{7}	9.15×10^{7}	9.15×10^{7}	9.15×10^{7}	1.83×10^{4}
2	30	11.8	12.7	13.0	14.4	13.8	13.14	2.68×10^{-3}
15	60	2.78	3.11	2.57	2.61	4.02	3.018	6.036×10^{-4}
3	90	2.60	2.67	2.75	2.81	2.61	2.688	5.376×10^{-4}
6	120	2.25	2.25	2.10	2.19	2.64	2.286	4.572×10^{-4}
7	150	1.97	2.10	2.07	2.09	2.20	2.074	4.148×10^{-4}

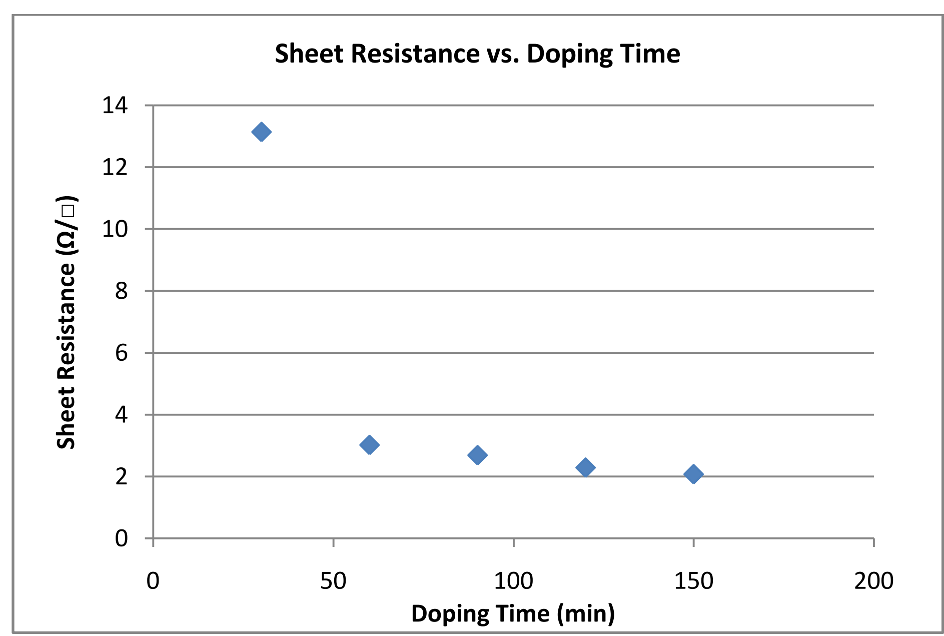

Figure 16. Results of the 4-point probe tests of sheet resistance plotted against the doping time for six of the wafers listed in Table 7

It must be noted that due to the high gradient in the dopant profile, the 4 point probe results may be skewed by the high dopant concentration region at the top of the thin film, adding a degree of inaccuracy to these measurements. However, since the surface concentration is linked directly to the

dopant profile the extracted value can still be used as a measure of average dopant concentration in the thin film. Sheet resistance drops drastically from the undoped wafer to an hour doped wafer. As the diffusion time increases, the decrease in resistivity between two subsequent wafers is reduced. This is due to the fact that not all the chemically incorporated phosphorus atoms are electrically active at dopant concentrations higher than 10^{18} atoms/cm^3. The average sheet resistance is related to the impurity concentration C(x) by Equation 24 (41).

$$R_s = \frac{1}{q\mu_{eff} \int_0^{x_j} C(x)dx} \qquad \text{Equation 24}$$

C(x) for each diffusion time can be obtained from the calculated dopant profiles in Figure 2, q is the charge of an electron and μ_{eff} is the effective majority carrier mobility in n-type semiconductor which can be calculated analytically using Equation 25 (41).

$$\mu_{eff} = \mu_n = \frac{1360 - 92}{1 + \left(\frac{C}{1.3} \times 10^{17}\right)^{0.91}} + 92 \qquad \text{Equation 25}$$

The average resistivity of the material can be calculated using Equation 26. The calculated resistivities can be found in Table 7.

$$\rho = R_s \cdot x_j = \frac{1}{q\mu_{eff}C_{ave}} \qquad \text{Equation 26}$$

Where x_j is the junction depth defined by the depth at which the dopant concentration is less than 10^{16} atoms/cm^3. The doping profiles in Figure 2 indicate that the junction depth of all the samples is larger than the 2μm thickness of the polysilicon film, hence, x_j can be assumed to be 2μm. Rearranging Equation 26 for C_{ave} in terms of resistivity we obtain Equation 27.

$$C_{ave} = \frac{1}{q\mu_{eff}\rho} \qquad \text{Equation 27}$$

Using the average resistivity of each wafer one can extract the average concentration of electrically active phosphorus atoms using the data presented by Mousty et. al. (47), which improves upon the Irvin curve by incorporating the concentration effects. The electron mobility is considered constant for concentrations higher than approximately 2×10^{19} cm^{-3}(43). An empirically derived relation between the electrically active phosphorus atoms, n, and the overall chemical concentration C_T is presented in Equation 28 (43).

$$C_T = n + 2.04 \times 10^{-41} n^3 \qquad \text{Equation 28}$$

From there, the average chemical concentration of phosphorus can be calculated using Equation 28. Table 8 shows the resistivity of each sample wafer, extracted average carrier concentration from Mousty's data, and calculated chemical phosphorus concentration. The average carrier concentration and chemical phosphorus concentrations are plotted versus the diffusion time in Figure 17.

Table 8. Average resistivity of each wafer and the calculated average carrier and atomic concentration

Wafer	Average Resistivity (Ω/cm)	Average Carrier Concentration (e^-/cm^{-3})	Average Chemical Phosphorus Concentration ($atoms/cm^3$)
10	1.83×10^{4}	0	0
2	2.68×10^{-3}	1.2×10^{19}	1.2×10^{19}
15	6.036×10^{-4}	9.1×10^{19}	1.06×10^{20}
3	5.376×10^{-4}	1.1×10^{20}	1.37×10^{20}
6	4.572×10^{-4}	1.4×10^{20}	1.96×10^{20}
7	4.148×10^{-4}	1.8×10^{20}	2.99×10^{20}

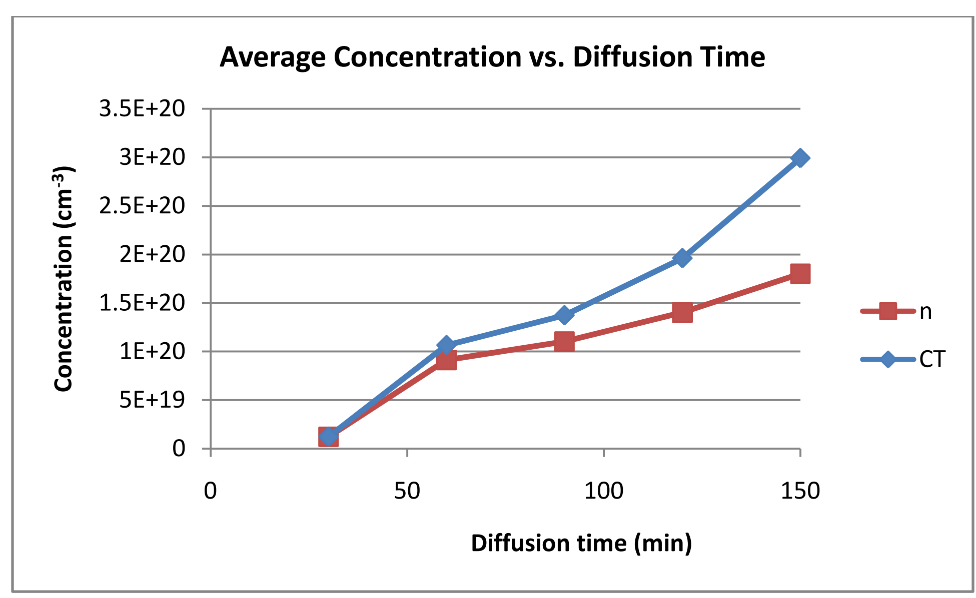

Figure 17. Average electrical carrier and chemical phosphorus concentration versus the doping time

Using the chemical concentration data, the estimated dopant distribution curves can be adjusted to fit the experimental resistivity data and are presented in Figure 18 and Table 9.

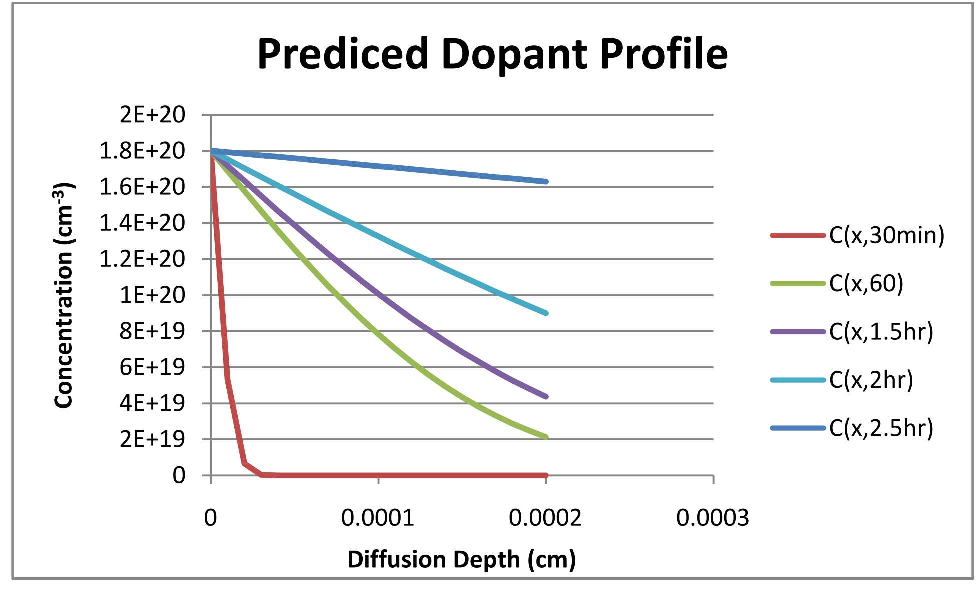

Figure 18. Dopant profiles predicted using the measured sheet resistance data

Table 9. Calculated stresses and stress gradients for different diffusion times using experimental sheet resistance data

Doping Time (hr)	Dopant Induced Average Tensile Stress (MPa)	Dopant Induced Average Stress Gradient (MPa)
0	0	0
0.5	0.428	6.73
1	3.24	5.94
1.5	3.92	5.10
2	4.99	3.37
2.5	6.41	0.641

4.2.5 Reactive Ion Etching of Polysilicon

Reactive ion etching was used to pattern the polysilicon and create the required devices. In order to get structures which have close to ideal geometry an anisotropic etching technique was needed, which meant wet etching could not be used. Photoresist, AZ3312, was used as a masking material to protect the required parts of the polysilicon during the RIE process. It was spun on at 4000rpm for 40 seconds to produce a 1µm thick layer, soft baked for 1 minute at 90ºC then exposed for 3 seconds through the mask using the MA6 Karl Suss mask aligner. The exposed photoresist was then developed for 10 seconds and hard baked for 5 minutes at 120ºC.

The RIE recipe was tuned by adjusting the pressure, bias voltage and ratio of gases present. The recipe was tested to make sure that the photoresist would withstand the etching for the required amount of time. Additionally, the recipe was tuned to achieve good sidewall straightness and roughness. The final RIE recipe used a pressure of 50mtorr, DC bias of 40V and 50ccm of SF_6 and 5ccm of O_2. With the final recipe, the etch rate did vary over the wafer with the edges etching slightly faster than the center. However, as each chip on the wafer was labeled individually any variation between chips could be tracked and accounted for. An example of a chip number can be seen in Figure 19. Figure 20 shows a picture of a wafer after RIE. The dicing lines and some of the larger structures are visible.

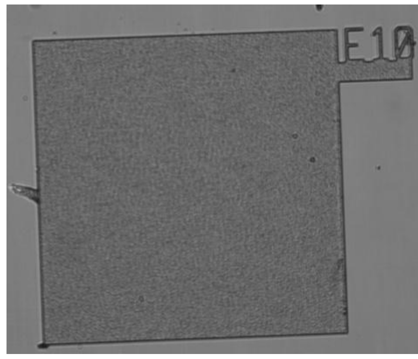

Figure 19. Chip number

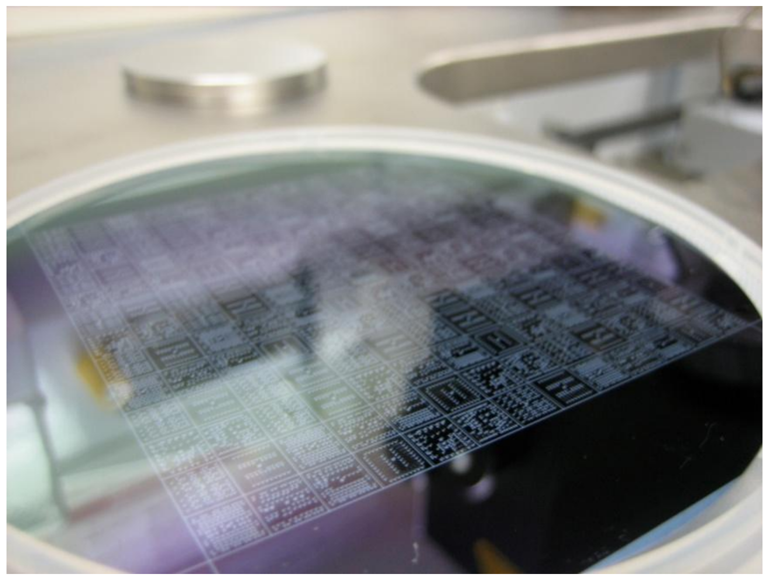

Figure 20. Wafer after RIE

The wafers were then coated in a protective photoresist layer, attached to UV dicing tape and diced into 5mm × 5mm chips. Figure 21 shows a diced wafer after the photoresist has been removed and the dicing tape has been exposed to UV to reduce the stickiness.

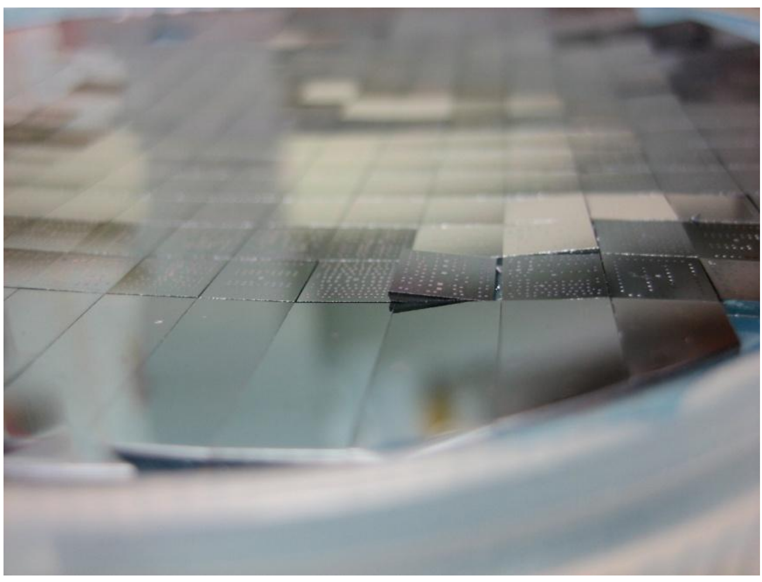

Figure 21. Wafer after dicing

4.2.6 Hydrofluoric Acid Etching of Silicon Oxide

In order to remove the sacrificial silicon dioxide layer and release the devices hydrofluoric acid (HF) was used. Hydrofluoric acid is highly selective for silicon oxide over silicon and attacks the polysilicon devices minimally during the release process. Thermal oxide was chosen in order to make the anchors of the devices sturdy. Since the oxide is grown from the silicon wafer it is well attached to the substrate, it is also denser than LPCVD oxide making for a stronger anchor. The high density of the oxide means that the HF etch rate is slower.

Due to the chosen fabrication process, the anchors connecting the devices to the substrate consist of a large polysilicon plate which acts as a mask and protects most of the oxide underneath. The device is connected to the plate and is attached to the substrate by the column of oxide, Figure 10 depicts the process. The size of the anchor must be chosen in accordance to the largest feature size in the free-standing devices that needs to be released. Since the HF acid etches the silicon oxide isotropically it will attack the oxide underneath the polysilicon evenly from all sides. As such, the anchors must be large enough such that even if the width of the largest device feature is etched from each side, the anchor is still large and stable enough to support the device and not cause excessive mechanical losses. However, the etching process is complex and many factors affect the etch rate. Since the

process is diffusion limited the shape and size of the cross-section of oxide to be etched as well as the masking material, polysilicon in this case, can affect the etching process (41).

Since many variables influence the etch rate of oxide the anchor size was chosen experimentally. An inexpensive flexible mask was used to create anchors, cantilever beams and plates in order to characterize the etch rate of the silicon oxide, determine the required etching time and to find the most appropriate anchor size. Initially, a 10:1 buffered oxide etch (NH_4F + HF) was used in order to slow down the etching process and maintain good control over the amount of oxide etched. However, the thermal oxide was very resilient and the required etching time was several hours. Due to that, 49% HF was used instead. Table 10 shows the results of time calibration of the HF release in order to release 30μm features. Beams of various lengths and widths attached to anchors of various sizes were used. For each release time, 6, 8 and 20 minutes, the beams were nudged with a probe tip to see if they were released. The released beams bent sideways whereas the unreleased beams broke at the boundary of the oxide and polysilicon due to the applied stresses. It was concluded that 20 minutes was a sufficient amount of time to release a 30μm feature.

Table 10. Calibrating HF etch time to release a 30μm feature

Release Time (min)	Beams	Broken 30μm beam
6	· 30μm beams unreleased · 20 μm beams unreleased, about 5 μm of oxide remaining	
8	· 30μm beams unreleased · 20 μm beams with bits of oxide remaining	

20	· 30 µm beams released · 50 µm beams unreleased, about 15 µm of oxide remaining	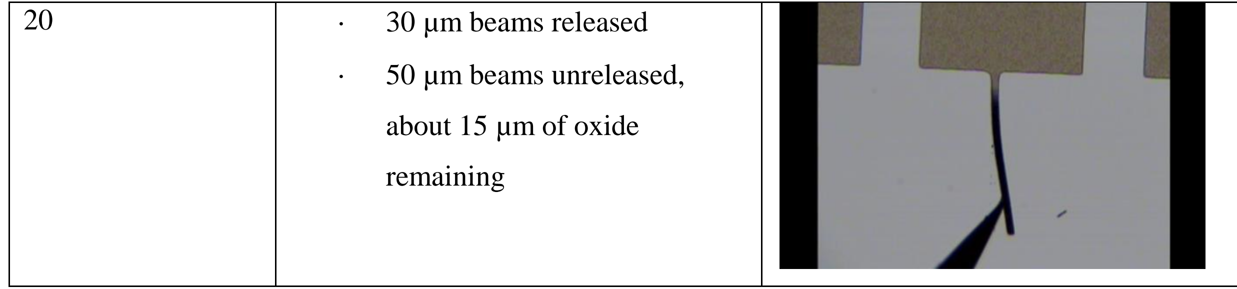

For the 20 minute release the undercut of different anchor sizes was checked by breaking the polysilicon plate using a probe tip, as shown in Table 11. Some of the 50µm anchors had been washed away, likely because they were smaller than 50µm due to the quality of the photolithography mask. By breaking the edges of the anchor the amount of oxide beneath becomes evident. The 300µm anchors were chosen for the final mask.

Table 11. Anchor testing, 18 minute 49% HF release

Anchor size (µm)		Anchor size (µm)	
50	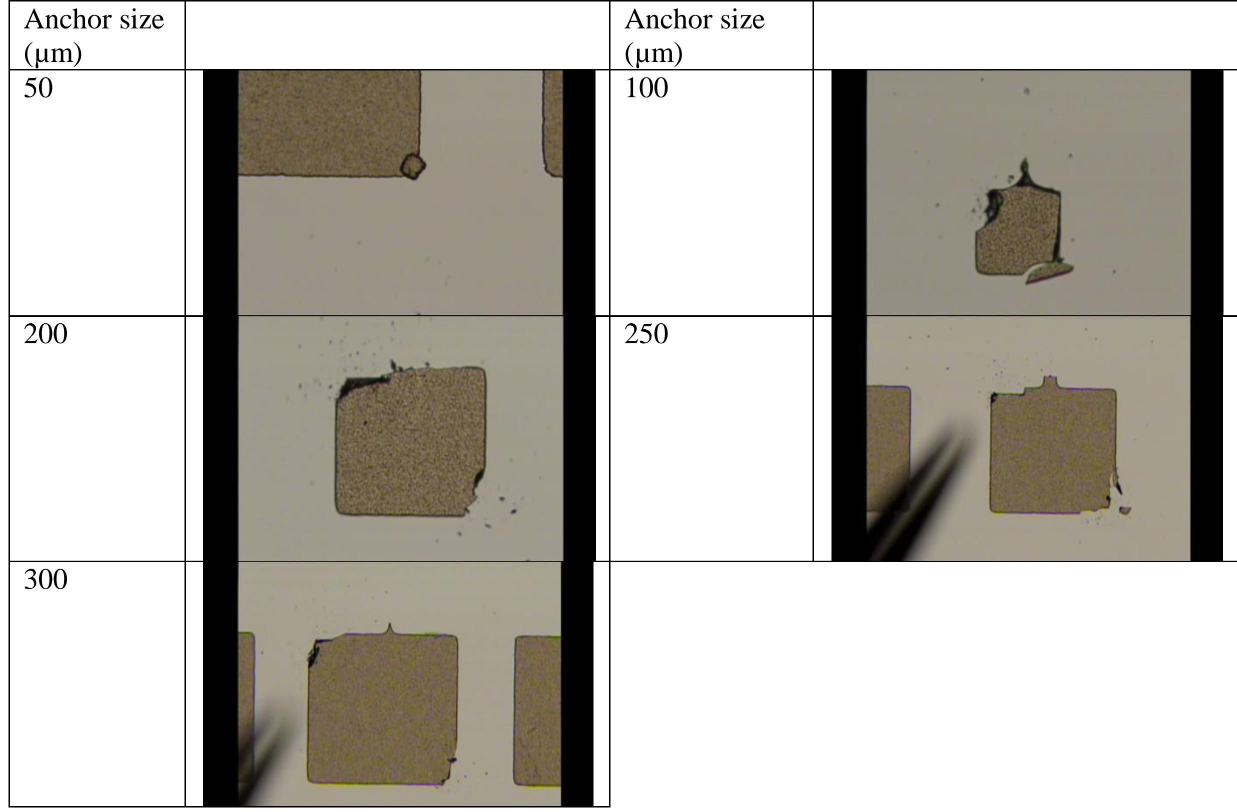	100	
200		250	
300			

After the release and testing of the proper chrome-mask devices a profilometer was used to measure the topology of the devices. Since the profilometer uses optical interferometry for measuring the topology one can adjust the parameters such that the change in transparency due to the oxide underneath the anchor is interpreted as a step in the z direction. Figure 22 shows the result of such a measurement, the undercut appears to be approximately 20 µm.

Figure 22. Profilometer image of an anchor from a released device, the undercut is about 20µm

4.2.7 Final Devices

Of the devices designed and fabricated, only a few were viable at the end of the process. The 2 µm feature sizes were difficult to replicate using the available photolithographic process. Figure 23 (a) shows the resulting pattern on the wafer after RIE and Figure 23(b) shows the masking pattern used. The beams in Figure 23(b) are 2 µm in width and have clearly not been transferred onto the polysilicon. Once the photolithography step was adjusted and calibrated the 2 µm features were transferred onto the polysilicon, however they were likely narrower than 2 µm.

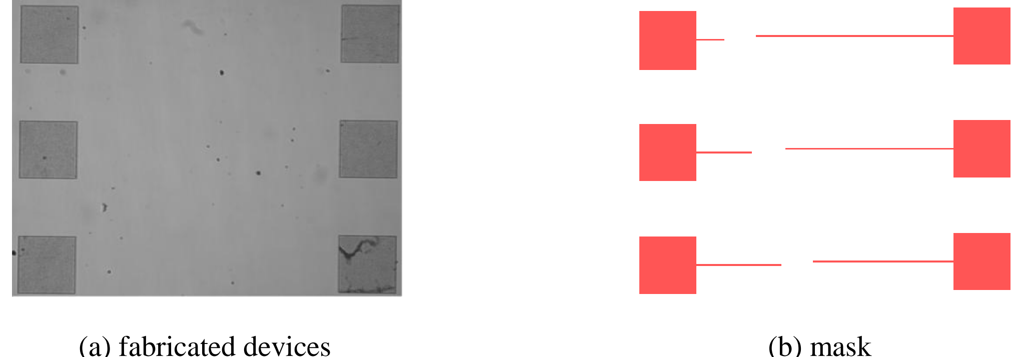

(a) fabricated devices (b) mask

Figure 23. Case in which the photolithographic step was not good enough to produce 2μm features

Many of the 2 μm and 5 μm features were too fragile to survive the release even when they did get transferred onto the polysilicon. Figure 24 (a) shows several clamped-clamped bridges with 2 μm and 5 μm widths before the release. The beams are well defined and not deformed. Figure 24 (b) shows similarly sized beams, also 2 and 5 μm wide after the release. First and second mode in plane buckling has occurred likely due to the fact that the width is smaller than or comparable to the thickness of the beam. Figure 24 (c) shows another released 2 μm that had broken likely during the release process when it was transferred from one liquid to another. Narrow cantilevers also deformed through in-plane bending as Figure 25 shows. Due to these issues devices containing long narrow parts were rendered unusable.

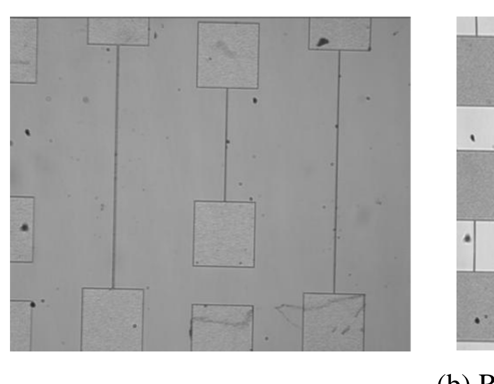

(a) Unreleased 2μm and 5μm clamped-clamped beams

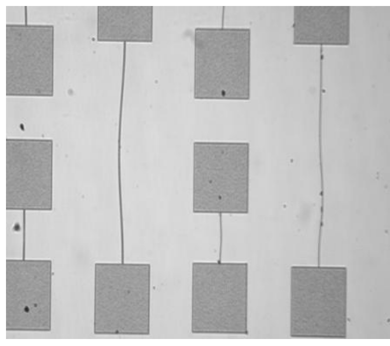

(b) Released 2μm and 5μm clamped-clamped beams, buckled in plane.

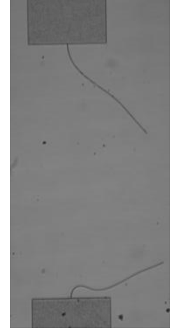

(c) Released 2μm clamped-clamped beam, broken.

Figure 24. Thin clamped-clamped beams before and after release

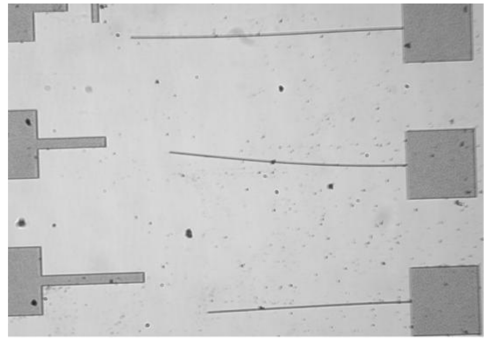

Figure 25. Cantilever beams of 2μm widths, bent in-plane.

Shorter 2μm features, like the indicators on the Vernier gauges, were not disturbed by the release. Figure 26 (a) shows a Vernier gauge before the release and Figure 26 (b) shows it after. While the teeth of the gauge are unaffected the beam it is attached to has broken, so again, the associated device is unusable. In the future, larger minimum feature sizes should be used, however, this would reduce the sensitivity of the devices greatly. Alternatively, a vapour HF release could be used to avoid stiction and breakage.

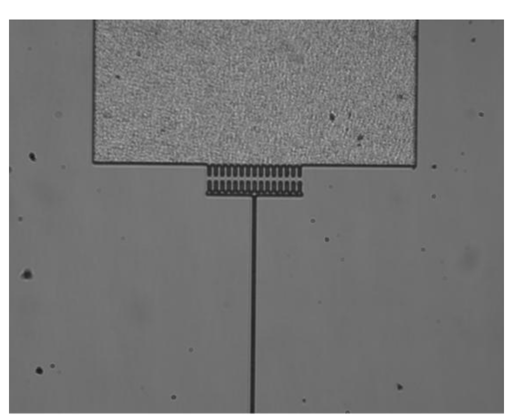

(a) Vernier gauge prior to release

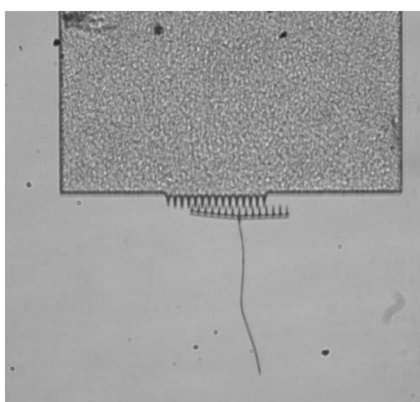

(b) Vernier gauge after release

Figure 26. Vernier gauge

The devices from 10µm to 30µm wide survived the release almost without issue. Figure 27 and Figure 28 show devices that have turned out well and are fully functional.

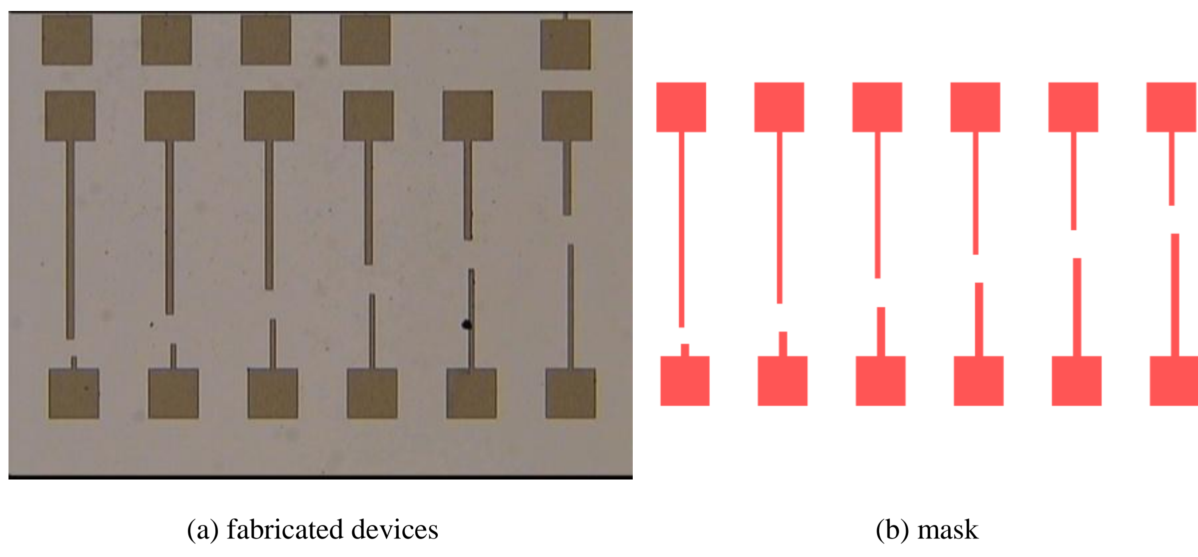

(a) fabricated devices (b) mask

Figure 27. Cantilever beams 20µm and 30µm wide

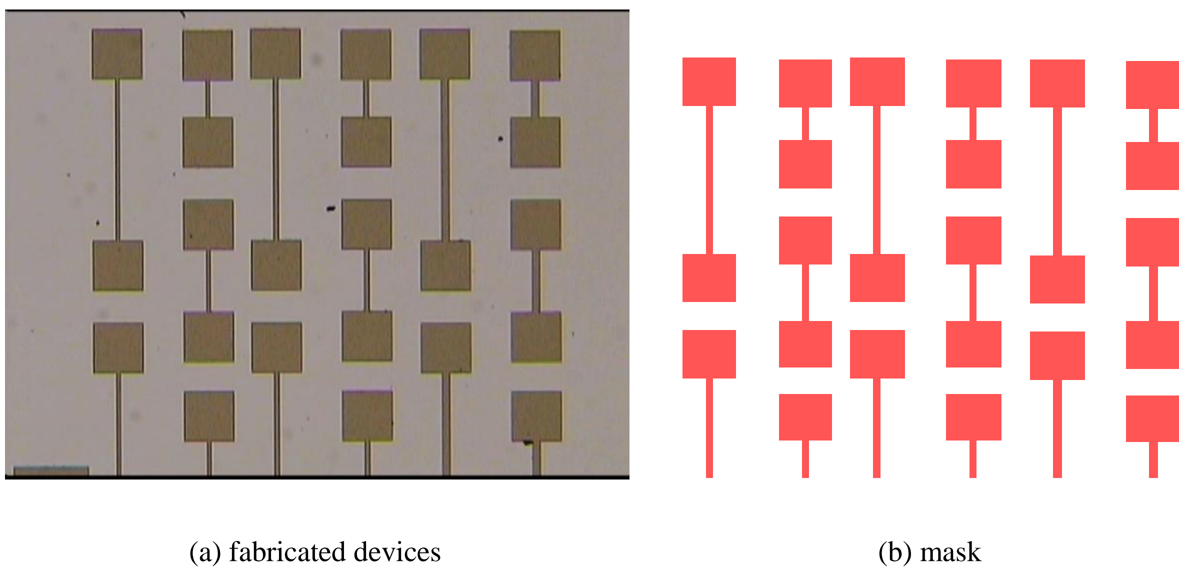

(a) fabricated devices (b) mask

Figure 28. Clamped-clamped beams, 15 µm, 20 µm and 30 µm wide

Chapter 5
Experimental Results

The devices were tested at room temperature. The primary goal of this experiment is to characterize the material properties of polysilicon with various concentrations of phosphorus. In the resonant test, the chip containing the devices was attached to a piezoelectric shaker and actuated mechanically. Additionally, devices were observed statically for buckling or deformation in order to extract the stresses.

5.1 Resonant Test

5.1.1 Experimental Setup

A 10mm x 10mm piezoelectric shaker from CeramTec was used to produce out of plane actuation. An Agilent 33220A Function Waveform Generator was used to provide the electrical signal to the piezoelectric shaker. The displacement produced by the piezo varied significantly with frequency when the same voltage was applied at all frequencies, as Figure 29 shows. The displacement of the piezoelectric shaker was calibrated by varying the voltage applied at different frequencies to produce the same amount of displacement at each frequency and get a consistent actuation force at the device. The calibrated displacement curve is shown in Figure 30. Although there is still a variation in the amount of displacement from frequency to frequency, it is much smaller.

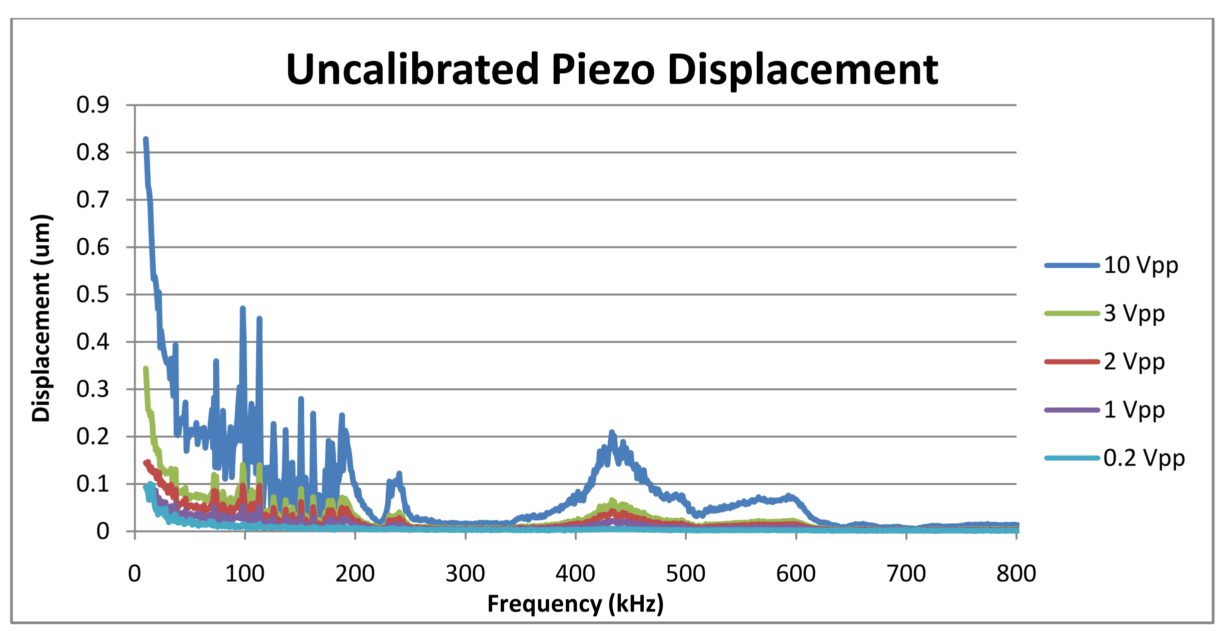

Figure 29. Uncalibrated piezo shaker response

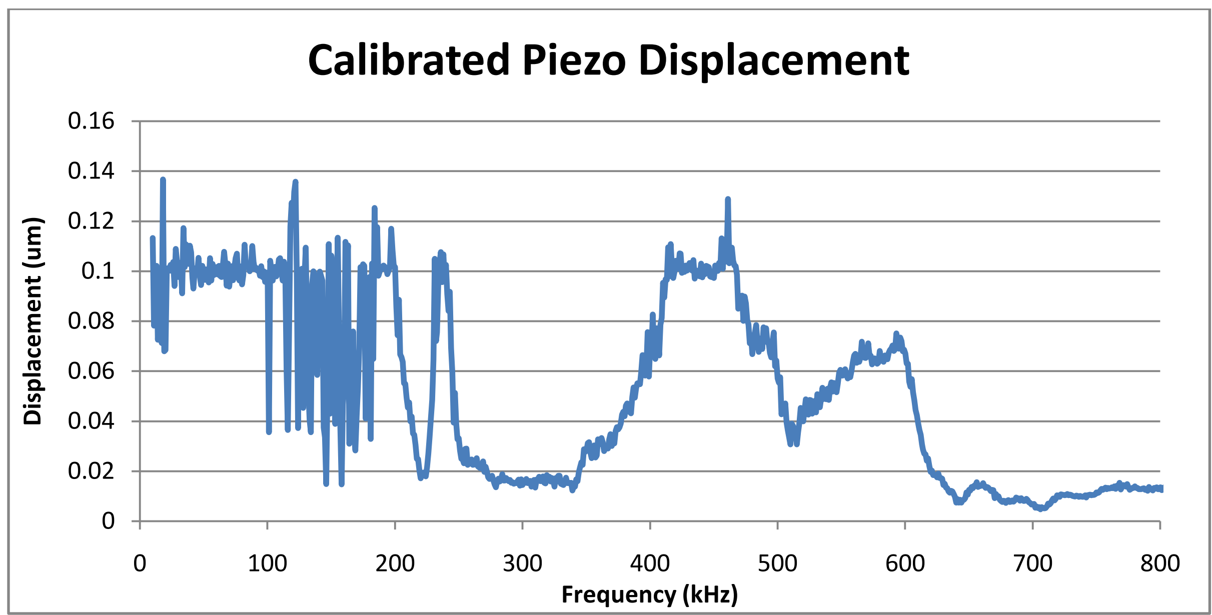

Figure 30. Calibrated piezo shaker response

A Polytec OFV-551 Vibrometer, Figure 31, was used to measure the velocity of the devices as well as for the calibration of the piezo. The vibrometer uses a laser and the Doppler effect to measure velocity and produces an appropriately scaled voltage signal. The voltage is displayed on an Agilent

5461D Mixed Signal Oscilloscope and read into the computer using a GPIB connection. Figure 32 shows the interconnection of the setup. Matlab code, Appendix A, was written to automate the testing procedure by changing the applied voltage and frequency and recording the amplitude of the displacement.

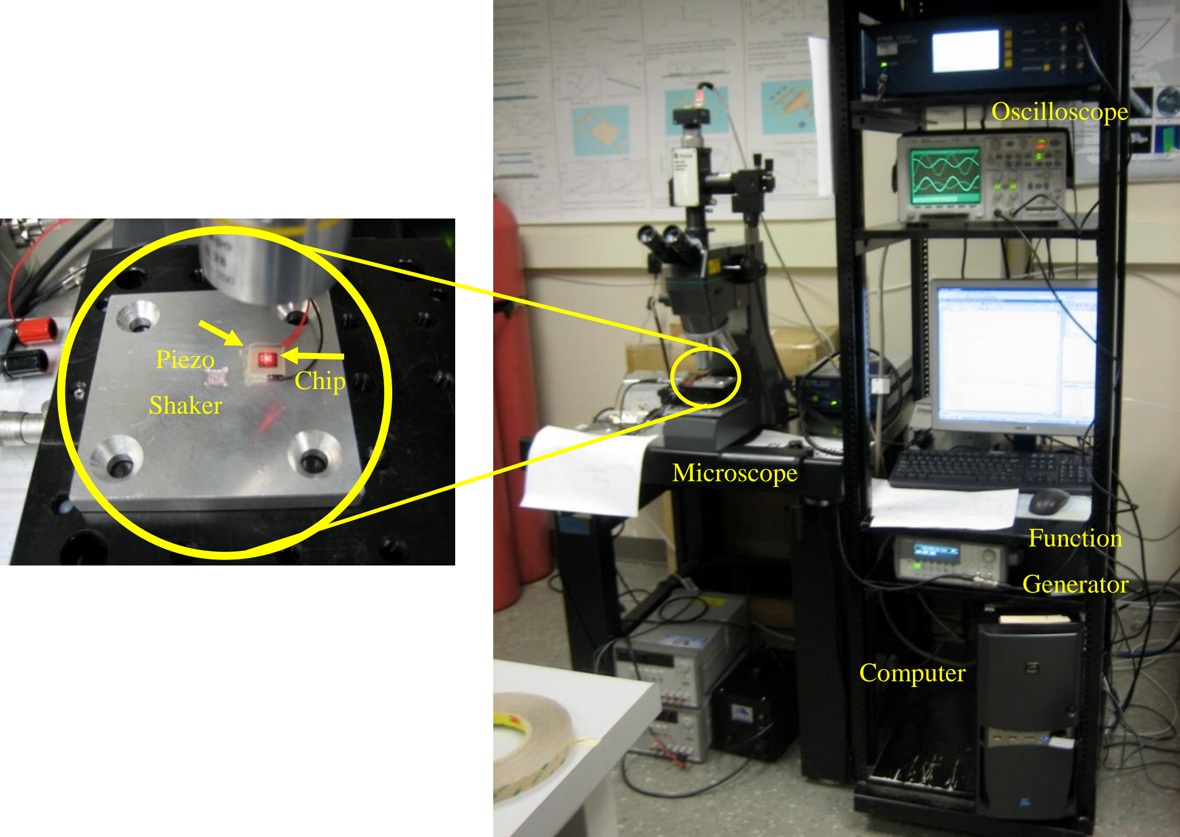

Figure 31. Photograph of experimental setup

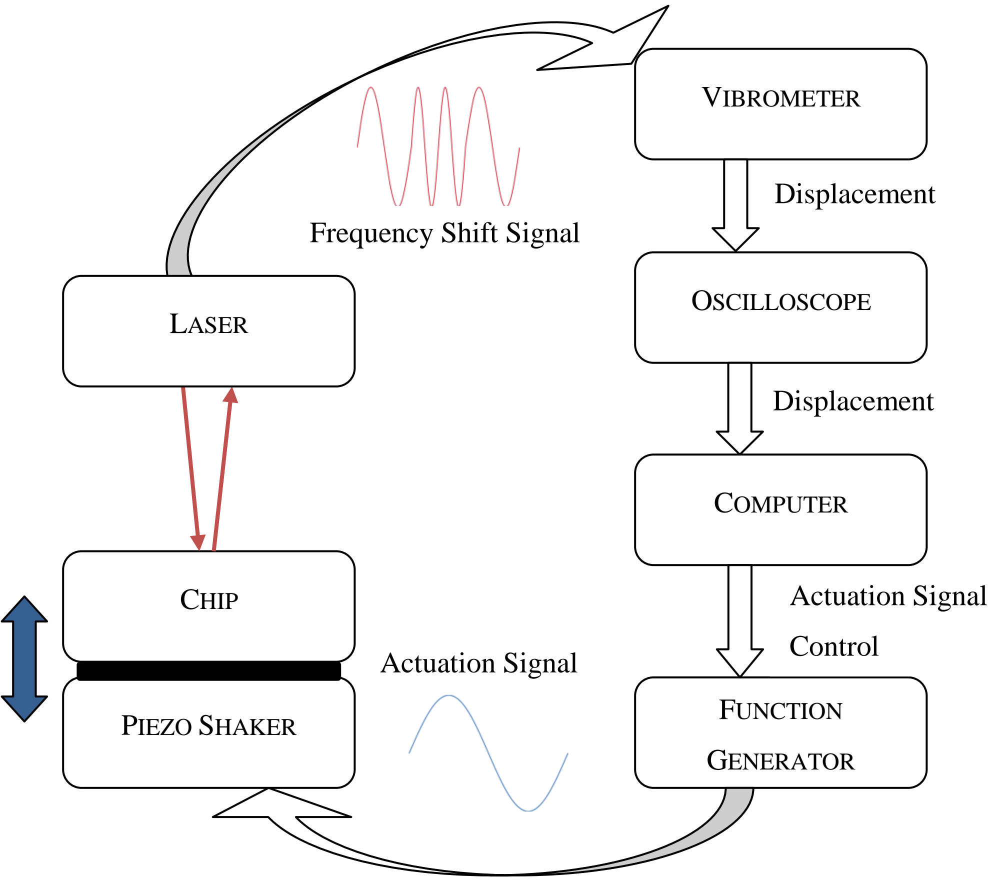

Figure 32. Experimental setup diagram **(48)**

5.2 Stress Characterization

Devices for characterizing the average stress as well as stress gradients were designed based on the calculated and expected stress values. It was expected that the undoped polysilicon would be nearly stress-free or possibly slightly compressive. The introduction of phosphorus into silicon was expected to produce an average tensile stress proportional to the dopant concentration. Since thermal diffusion without post-annealing was employed for introducing dopants into the host it was predicted that the dopant profile, and hence the out-of-plane stress was not going to be constant through the thickness of the film. The conductivity of the polysilicon was measured using a 4-point probe, Table 7 and Figure 16, and new expected dopant profiles and expected stresses were re-calculated, Figure 18, Table 9,

with this data. The average stress and stress gradient measurements are not only valuable in and of themselves but also to accurately extract the Young's modulus from resonant tests and verify the expected dopant profiles.

5.2.1 Clamped-clamped Beam Deformation

Clamped-clamped beams under compressive stress buckle and deform by an amount proportional to the stress. By observing the deformation of the beams once can extract the associated compressive stress. Tensile stress is not detectible with the use of clamped-clamped beams unless it is large enough to cause cracking or breaking. Beams of different widths and lengths were fabricated, a set of beams of the same width are shown in

Figure 33, each set contains 8 beams of different lengths, as labeled on the figure. Six sets of beams were fabricated, as shown in Figure 34, with widths of 30μm, 20 μm, 15 μm, 10 μm, 5 μm and 2 μm. In addition to average compressive stress measurement, the beams were used for resonant tests, section 5.3.2, and were going to be used for pull-in M-tests, section 5.3.1.

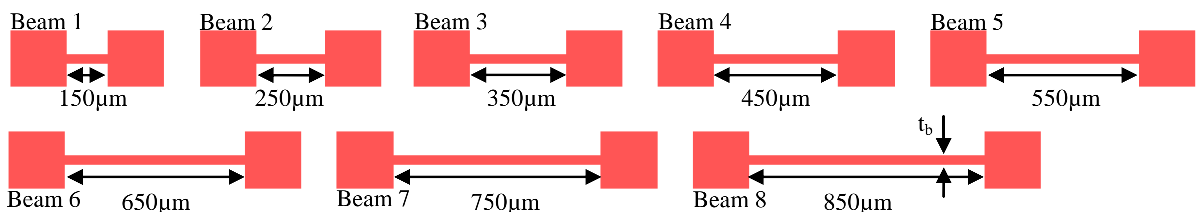

Figure 33. Clamped-clamped beam set

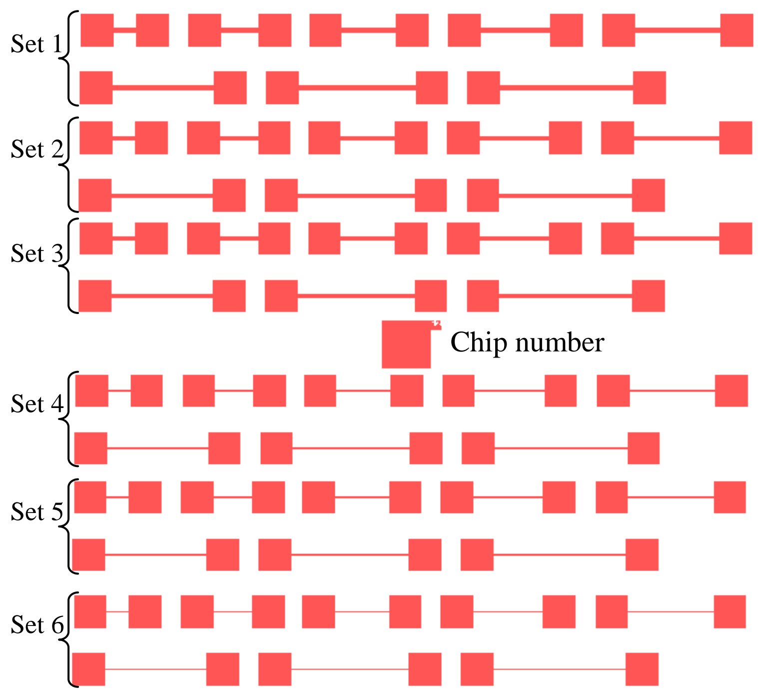

Figure 34. Clamped-clamped beams chip

5.2.1.1 Undoped Clamped-clamped Beams

Since the fabrication process involves several steps, and each step could potentially introduce variation to the material or geometrical properties of the device it is important to have a control group. In general, undoped structures serve as a control for the doped devices. The undoped clamped-clamped beams, Figure 35, clearly show significant out-of-plane buckling. Undoped polysilicon produced by chemical vapour deposition often suffers from compressive stresses, so the presence of buckling is not unexpected. Figure 36 shows the cross-section of several buckled beams.

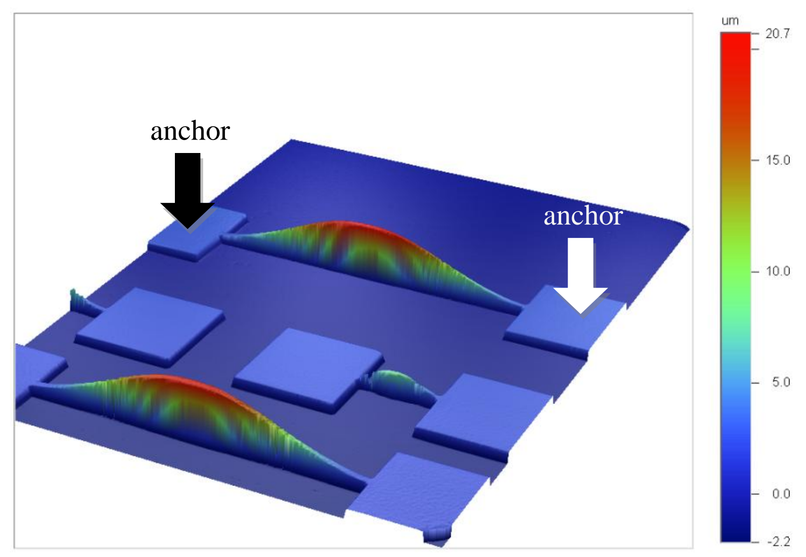

Figure 35. Three dimensional profilometer results of undoped clamped-clamped beams

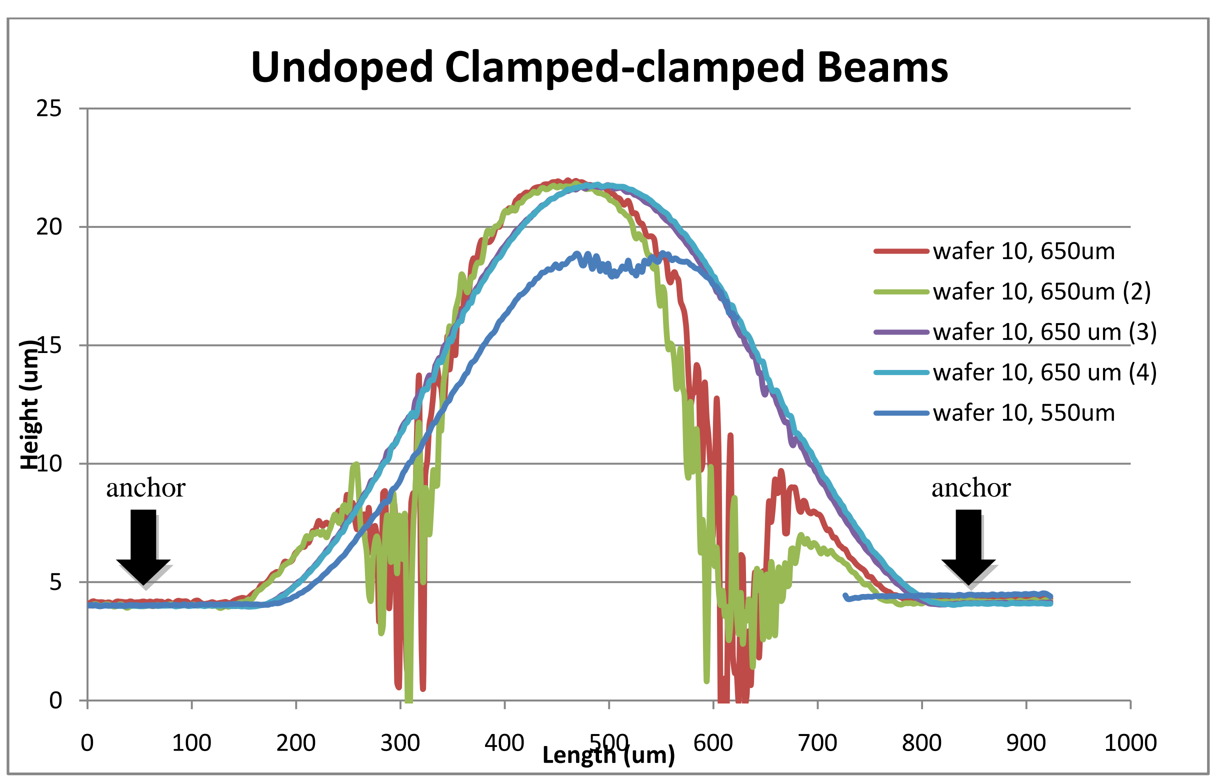

Figure 36. Cross sections of several undoped clamped-clamped beams from profilometer results

5.2.1.2 0.5 Hours Doped Clamped-clamped Beams

The 30 minute doped polysilicon was the least doped sample, which was expected to have the highest dopant gradient through the thickness of the film. Note the slight concavity change at about ¼ length of the beams in Figure 37, marked with arrows. The extra inflection points were likely introduced by the large stress gradient, a similar shape can be seen in the 0.5 hour doped cantilever beams in Figure 59, which is discussed in section 5.3.4.2.

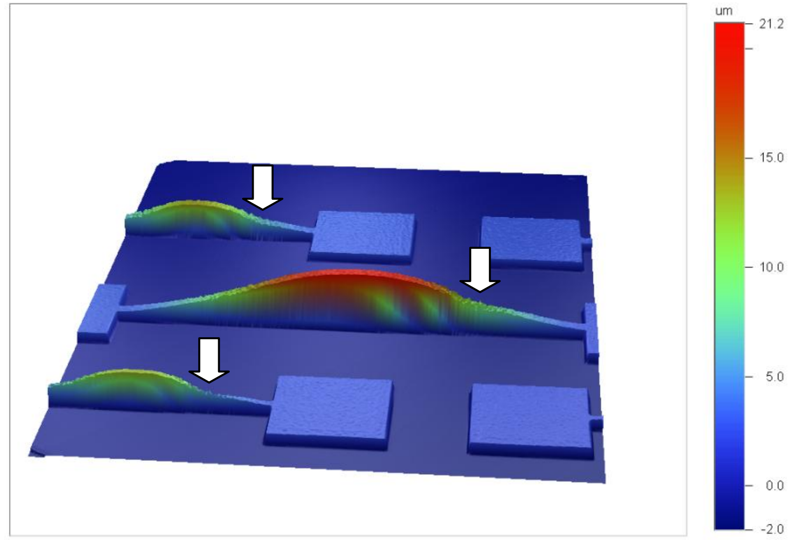

Figure 37. Three dimensional profilometer results of clamped-clamped beams from a wafer with 0.5 hours of doping

Figure 38 shows the cross-section of several 0.5 hour doped beams. Since the figure contains data from several different beams of the same length it is evident that the amount of out-of-plane buckling is very consistent between different samples.

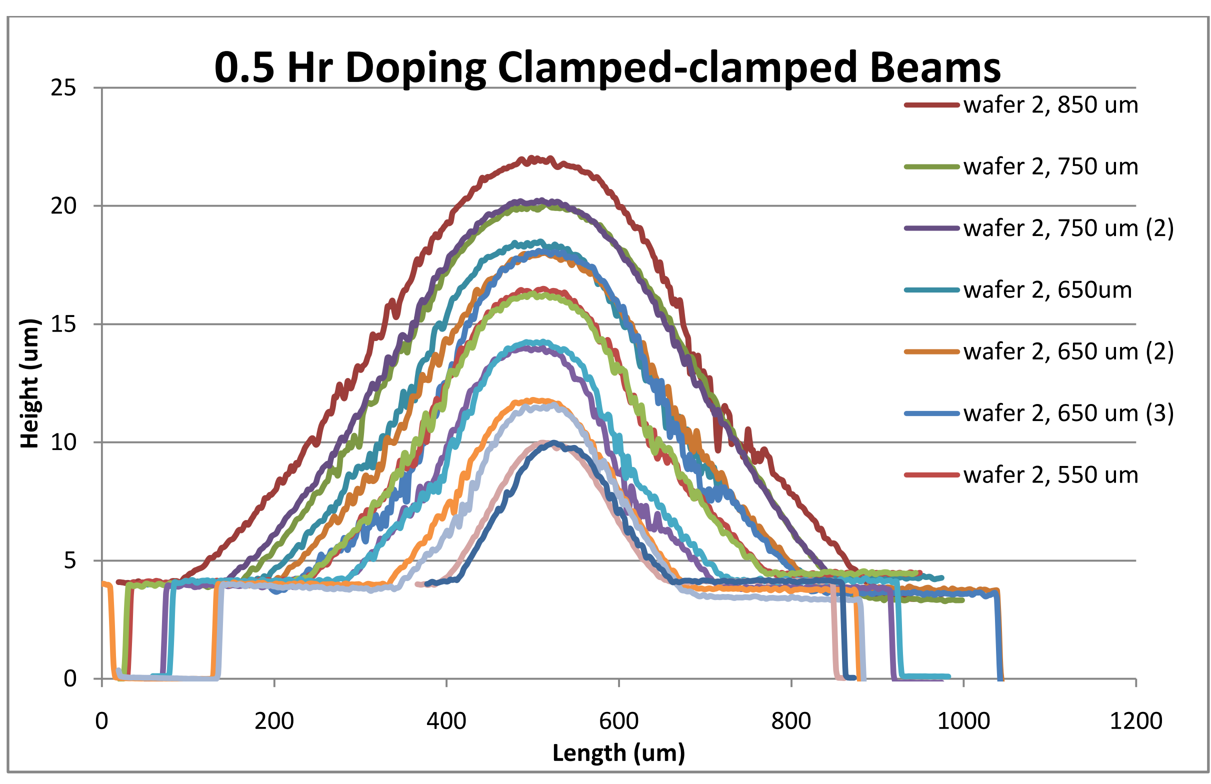

Figure 38. Cross sections of several 0.5 hour doped clamped-clamped beams from profilometer results

5.2.1.3 2 Hours Doped Clamped-clamped Beams

Figure 39 shows the three dimensional profilometer data from some of the 2 hour doped beams. The beams in that figure are only 10 μm and 5 μm wide, though most of the thinner beams were unusable there were a few that produced good results. In general, it is advantageous to have thinner structures because they are a closer match for the assumptions made in the analytical calculations. Figure 40 shows the cross-section of several beams. The data shows rapid small scale variations in height along the length of the beam. The profilometer uses optical interferometry to find the topology of the structures and since polysilicon is not 100% opaque some interference occurs between the light reflected from the substrate and that reflected from the top of the device causing the profilometer to interpret the signal as unrealistic topology. Additionally, polysilicon is fairly rough and light is likely scattered and diffused from the surface causing the signal to noise ratio to decrease.

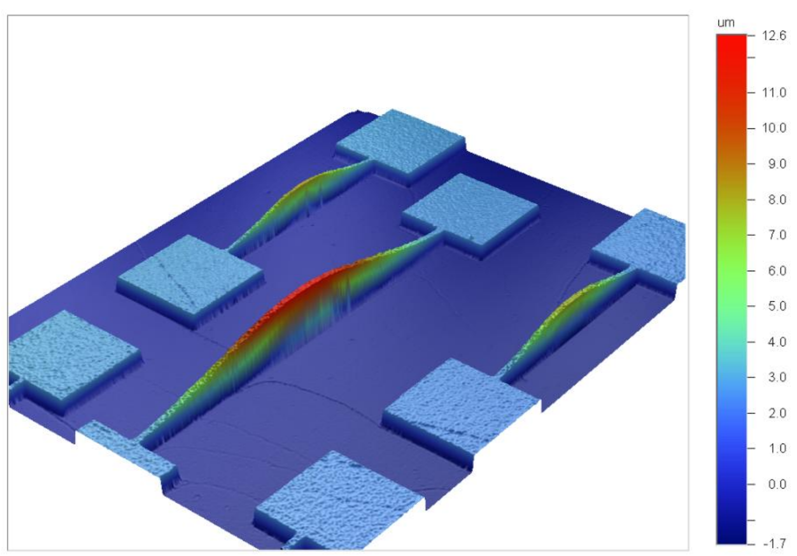

Figure 39. Three dimensional profilometer results of clamped-clamped beams from a wafer with 2 hours of doping

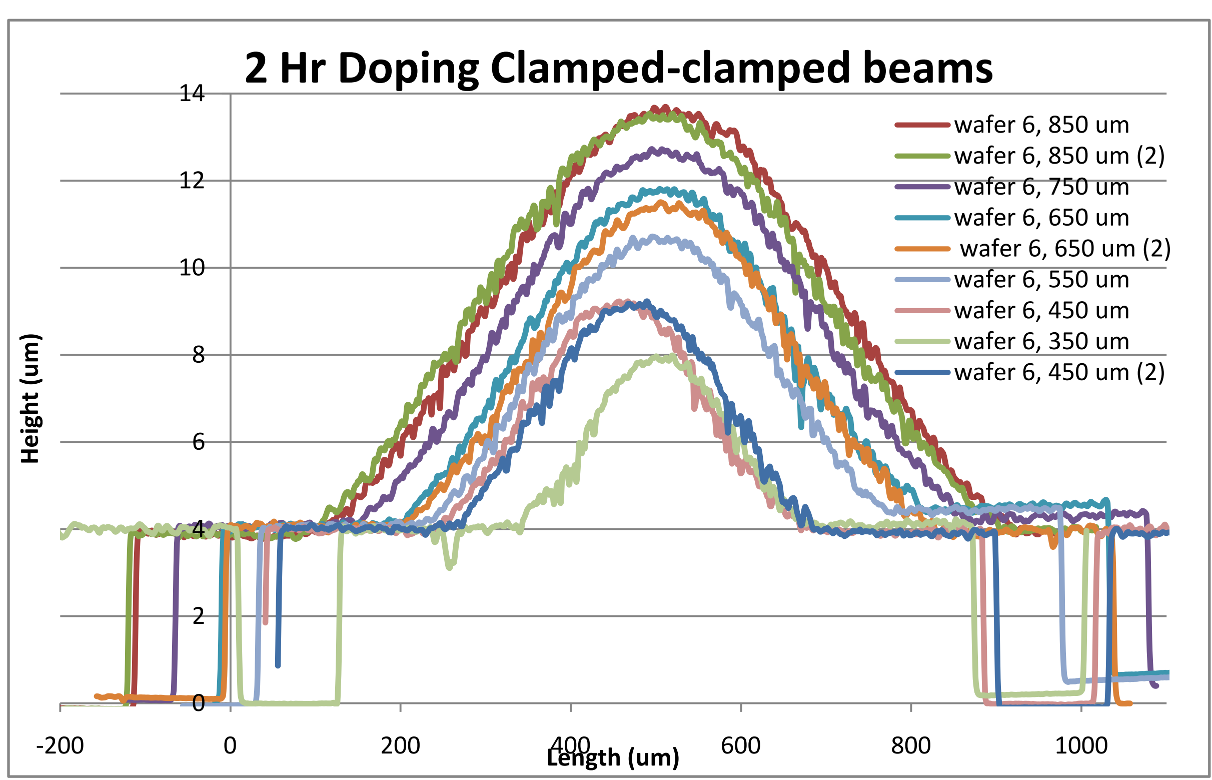

Figure 40. Cross sections of several 2 hour doped clamped-clamped beams from profilometer results

5.2.1.4 2.5 Hours Doped Clamped-clamped Beams

Figure 41 shows the topology of several 2.5 hour doped clamped-clamped beams. It is interesting to note that two of the shorter beams are stuck while the longer ones are released. Usually with a wet release, there is a critical length above which all devices are stuck and below which most devices are not. There are two possible explanations for this particular anomaly. First, there is still enough compressive stress that the beams of the given length buckle. The direction of buckling is determined probabilistically if no irregularities in the beam exist that would cause it to buckle a certain way. It is possible that the shorter beams buckled down upon release whereas the longer beams buckled up. This scenario would make the shorter beams stick while leaving the longer ones unaffected. An alternative reason could be that the amplitude of the out-of-plane deflection is higher for longer beams than for shorter ones meaning that, once buckled, they are further away from the substrate and more likely to remain unstuck. Figure 42 shows the cross-section of several unstuck beams.

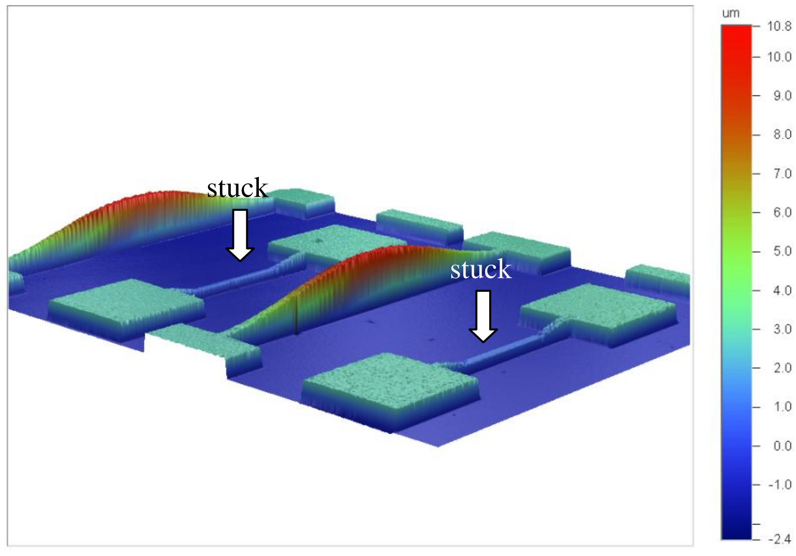

Figure 41. Three dimensional profilometer results of clamped-clamped beams from a wafer with 2.5 hours of doping

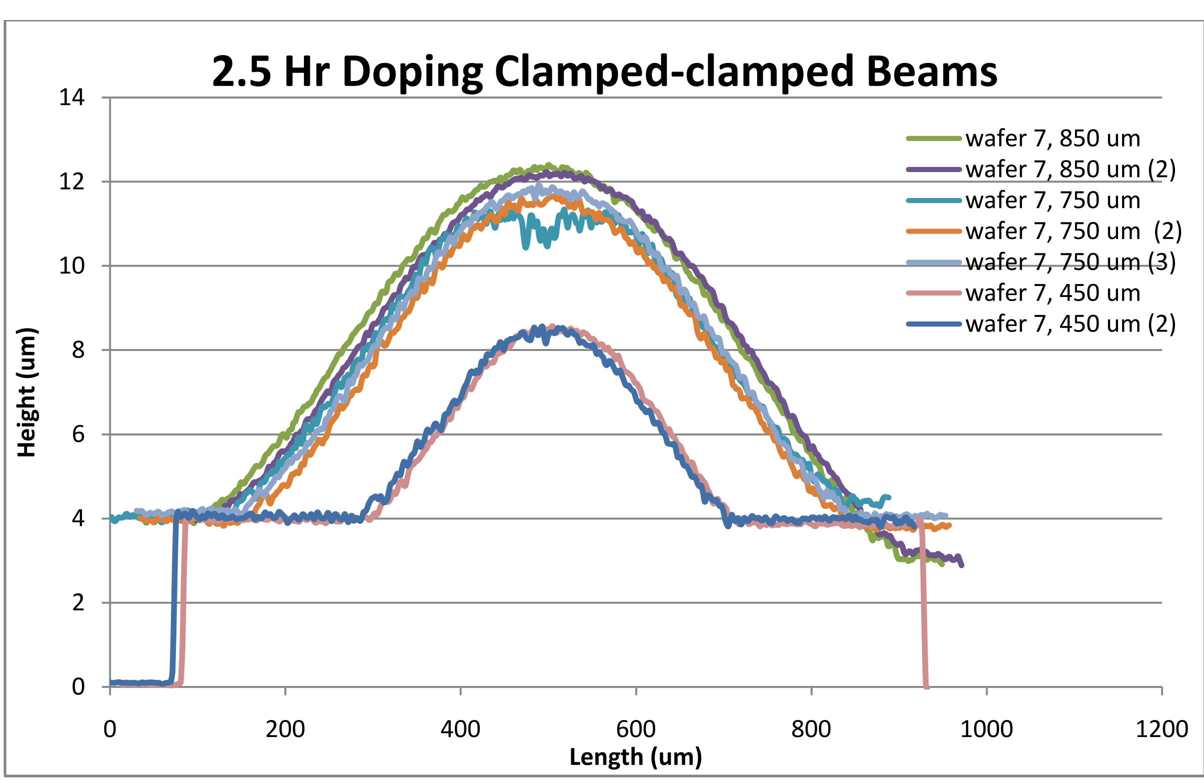

Figure 42. Cross sections of several 2.5 hour doped clamped-clamped beams from profilometer results

5.2.1.5 2.5 Comparison and Discussion

Since all the beams of all the doping concentrations are buckled it is not possible to use the critical buckling length approach in order to extract the average compressive stress. Also, it means that the fabrication process has introduced a large amount of compressive stress into the material. This likely occurred during polysilicon deposition, as this is often the case. Figure 43 summarizes the data from Figure 36-Figure 42 and shows the average out-of-plane deflections of beams of different length and different doping concentrations. The linear relation between the length of the beam and the deflection is shown clearly, as expected. This fact can serve as assurance that the data was collected properly. More importantly, there is a clear reduction in out-of-plane deflection with increase in doping time, and hence, average dopant concentration. As predicted, the smaller phosphorus atoms introduce tensile stress into the material and serve to counteract the intrinsic compressive stress.

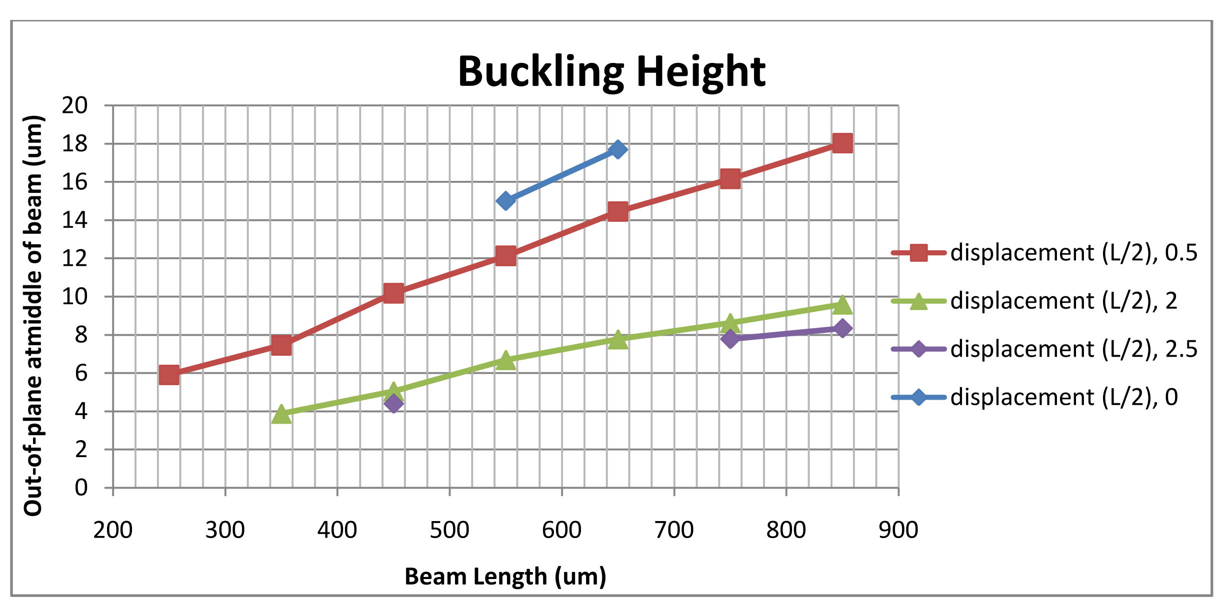

Figure 43. Out-of-plane buckling of clamped-clamped beams versus the beam length

Both stress and Young's modulus are presumed to be functions of dopant concentrations. Hence, various possible combinations of Young's modulus and stress can produce the observed deflections. Using Equation 22, the relation between the Young's modulus, stress and deflection can be defined and the Young's modulus versus stress graph can be produced for a particular deflection of a particular length beam, Figure 44. Again, the amount of predicted stress for a beam of certain length with the same presumed Young's modulus varies consistently with doping time. The amount of stress decrease between the undoped and 0.5 hour doped beams is larger than that between the 2 hour doped and the 2.5 hour doped beams. This is likely due to saturation of the host material at a doping time somewhere between 2 and 2.5 hours.

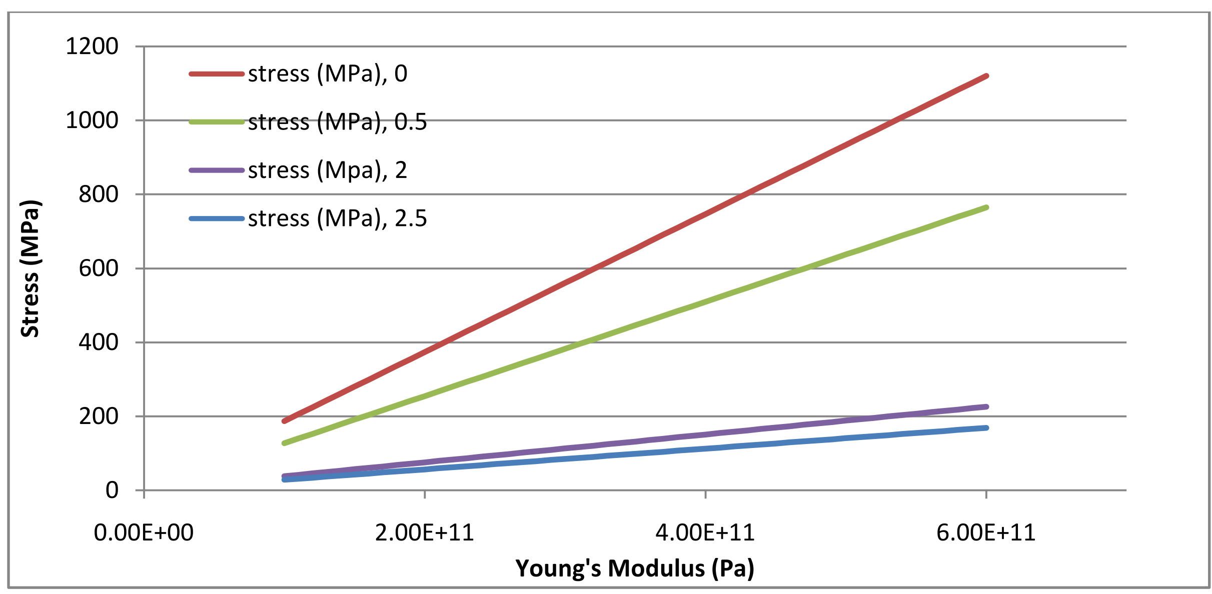

Figure 44. Possible combinations of stress and Young's modulus for various doping concentrations as extracted from clamped-clamped beam buckling

5.3 Young's modulus

5.3.1 Clamped-clamped Beam M-Test

The M-test was going to be performed using the clamped-clamped beams that were used for resonant testing and for extracting the compressive stress. Due to the unexpectedly large residual compressive stress, the beams had significant out-of-plane bending. The nature of the M-tests required that the test structure and the bottom electrode, substrate in this case, have a constant air gap. Since the electrostatic force developed between the beam and the substrate is highly distance dependent, it is not possible to proceed with the M-test using the available clamped-clamped beams without significant alterations to the available model, which is out of the scope of the current work. Cantilever beams cannot be used for the M-test due to the large stress gradient leading to large out of plane deflections.

5.3.2 Clamped-clamped Beam Resonant Tests

The clamped-clamped beams described in section 5.2.1 were also used for resonant tests. In this technique, the resonant frequency of the beam is used in conjunction with a simple analytical equation to extract the stiffness of the beam and, from there, the Young's modulus. The experimental

setup for these measurements is described in section 5.1.1. The data presented in the following subsections was collected from several chip samples which were released in different batches, labelled release 1, 2 and 3. The release process was repeated as consistently as possible. The samples were also tracked by chip number which is also noted in the graphs, K11, for example. Beams of widths 30 μm, 20 μm and 15 μm were used, and treated equivalently.

Cantilever beams were initially intended to undergo this test as well; however, due to the large stress gradient it was not possible. The large out of plane deflection of the cantilevers often meant that even though the beam was not stuck, either the tip or the middle of the cantilever came into contact with the substrate during actuation. While some data was acquired, there was not enough to make a reasonable comparison.

Figure 45 and Figure 46 show the frequency responses of several beams, the geometrical properties of the beams are described in section 5.2.1. The approximate location of the resonant frequencies is identified on the graphs with an arrow. The rest of the collected data for doping times of 0, 0.5, 2 and 2.5 hours can be found in Appendix B.

Figure 45 shows a fairly large split between the resonant frequencies of different samples. The two different frequencies occur in several samples and, as such, cannot be disregarded as outliers. Specific widths of the beams don't appear to be associated with the lower or higher frequency, and are ruled out as the possible cause of discrepancy. The release or variation between chips can also be ruled out, as each frequency occurs in both chips. Measurements were repeated several times and the resonant frequency of a specific beam varied by 2 kHz at most, so the different observed frequencies are not due to a lack of measurement consistency. Both frequencies were considered valid and were used in the analysis and material property extraction.

Figure 46 shows the resonant frequency of beam 4, which is longer than beam 2 in Figure 45. Note the shift in frequency due to the change in size of the beam. Additionally, Figure 46 shows good agreement between the resonant frequencies from several samples. Most of the data collected, and presented in Appendix B, shows agreement similar to that seen in Figure 46.

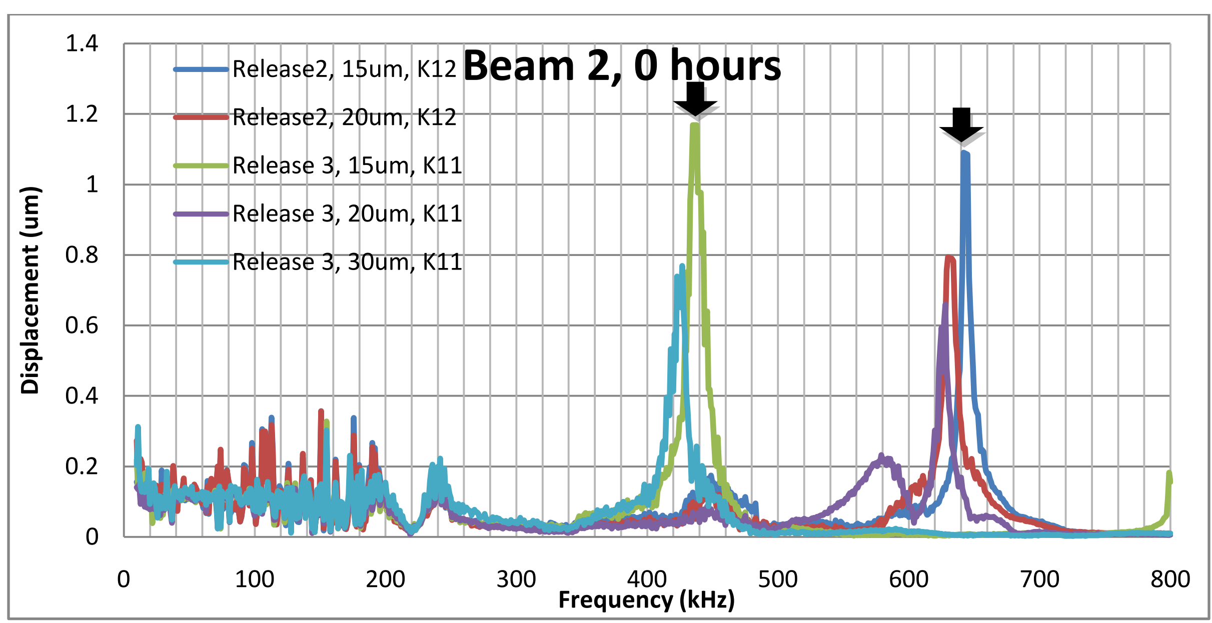

Figure 45. Frequency response of several 250µm long clamped-clamped beams with 0 hours of doping

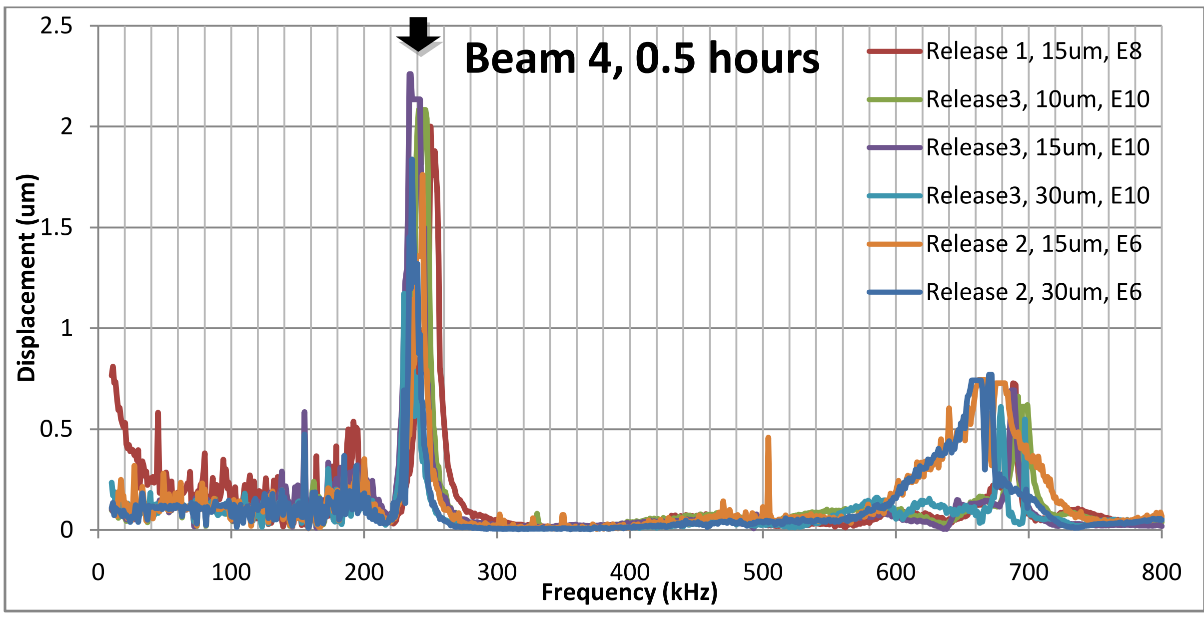

Figure 46. Frequency response of several 450µm long clamped-clamped beams with 0.5 hours of doping

5.3.2.1 Summary of Resonant Frequency Data

The data collected from the resonant tests is summarized in Figure 47.

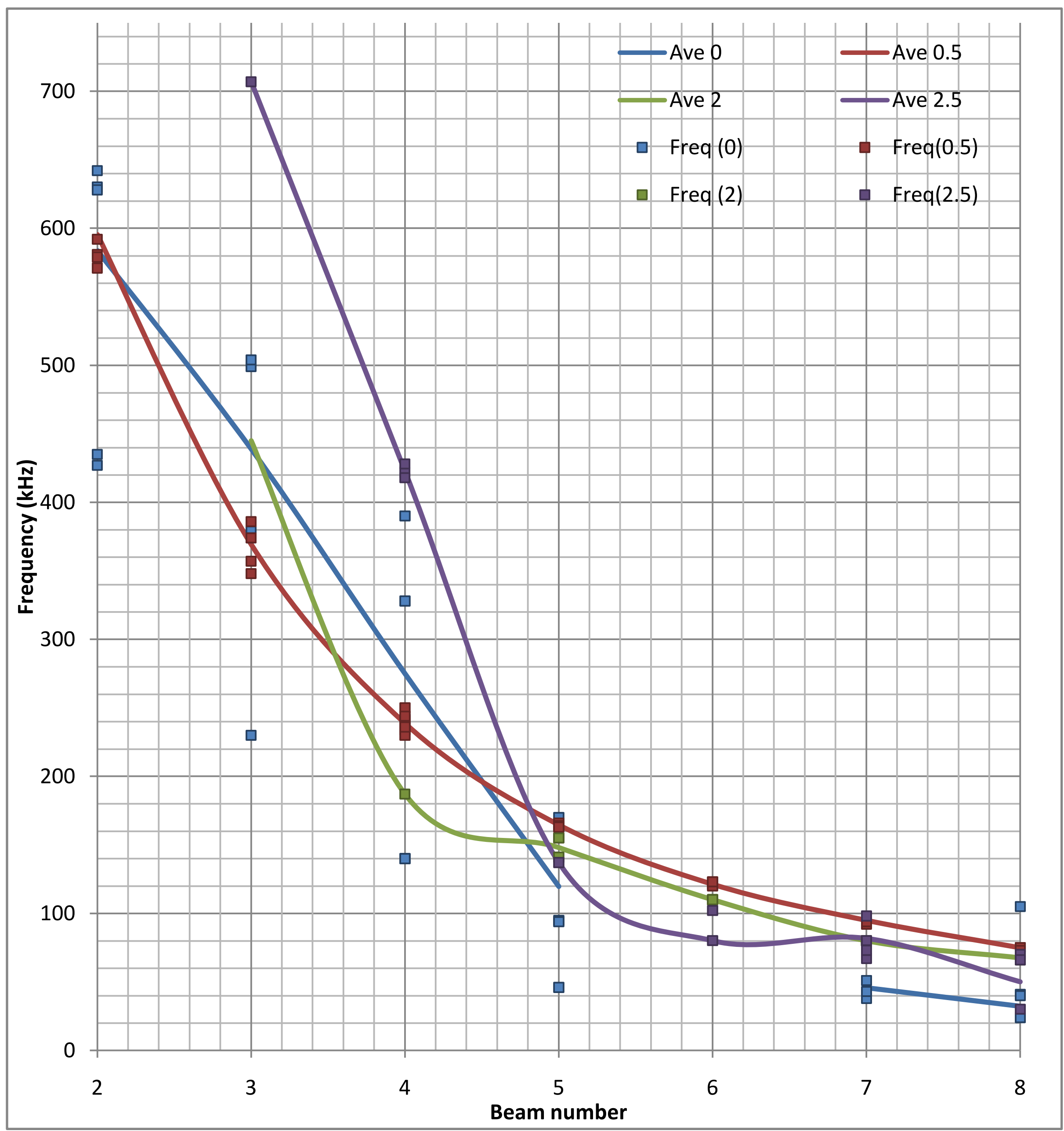

Figure 47. Resonant frequencies of various beams from undoped, 0.5 hour, 2 hour and 2.5 hour doped polysilicon

Each of the data sets in the figure show a definite decrease in resonant frequency with an increase in beam length. The data is fairly widely distributed around the average value, particularly for the undoped samples and for smaller beam lengths. When comparing the resonant frequencies of different dopant concentrations, no clear pattern can be discerned. However, since each of the films has a different average stress due to the dopant concentration it is not possible to draw conclusions regarding the value of the Young's modulus from this data. Stress must be considered as it contributes to the stiffness of the beam.

5.3.3 Extracting Young's Modulus and Average Stress

Both the buckling and the resonant frequency of the beam depend on the Young's modulus and the residual stress, due to that, both parameters cannot be extracted from only one test type. However, by combining the data of the buckling amplitude and resonant frequency both the Young's modulus and average residual stress can be extracted. By using Equation 12 and the average resonant frequency a range of Young's modulus and stress values can be found to make the equality true. Similarly, the out-of-plane buckling of clamped-clamped beams and Equation 22 can be used to find a set of solutions for the Young's modulus and average stress. Since both the equations are describing the same material, the intersection of their solutions should produce the correct Young's modulus and residual stress values. Figure 48- Figure 51 show the plots of the possible Young's modulus versus residual stress for the buckled beam and resonant frequency data. The intersections of the sets of curves provides the range for the possible Young's modulus and stress values, as marked on Figure 48.

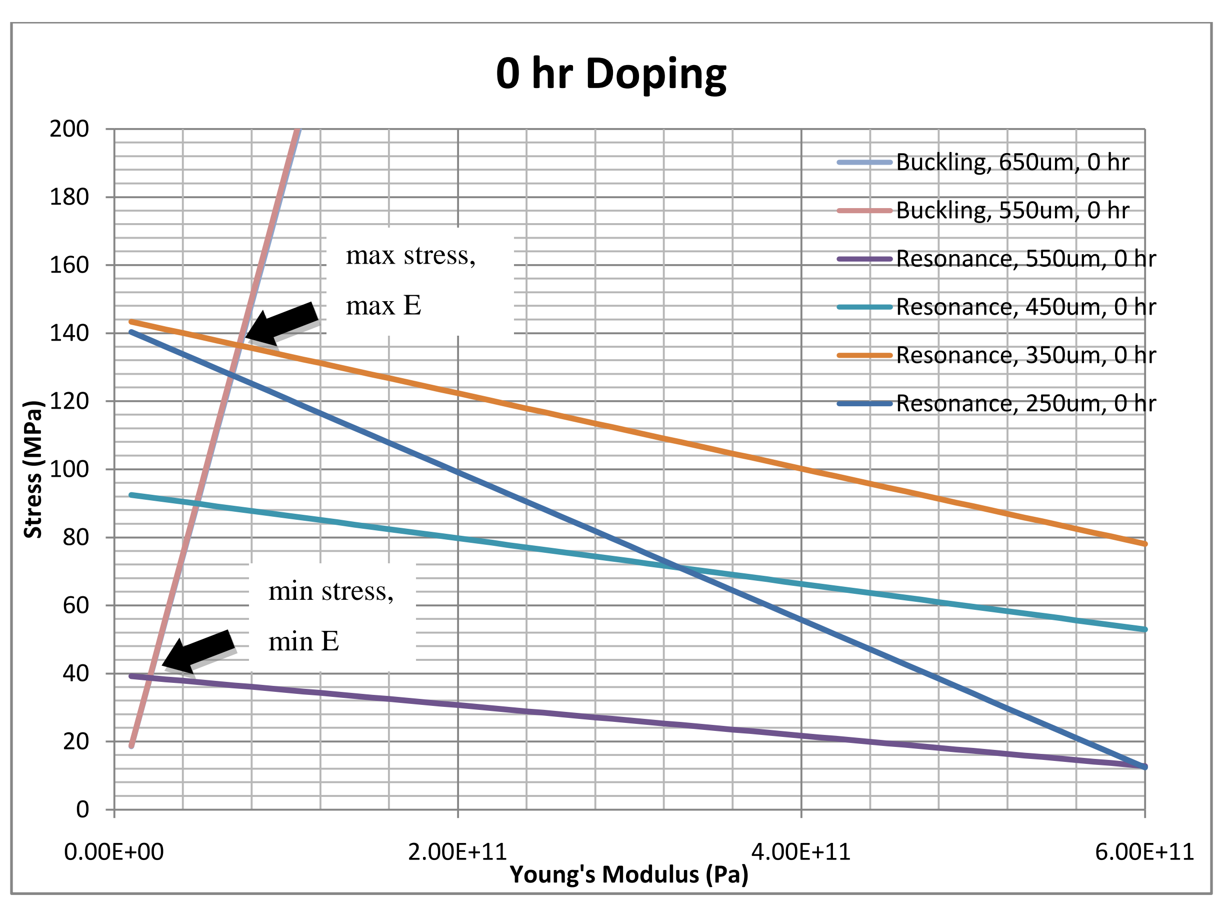

Figure 48. Possible combinations of stress and Young's modulus for undoped polysilicon as extracted from clamped-clamped beam buckling and resonant tests

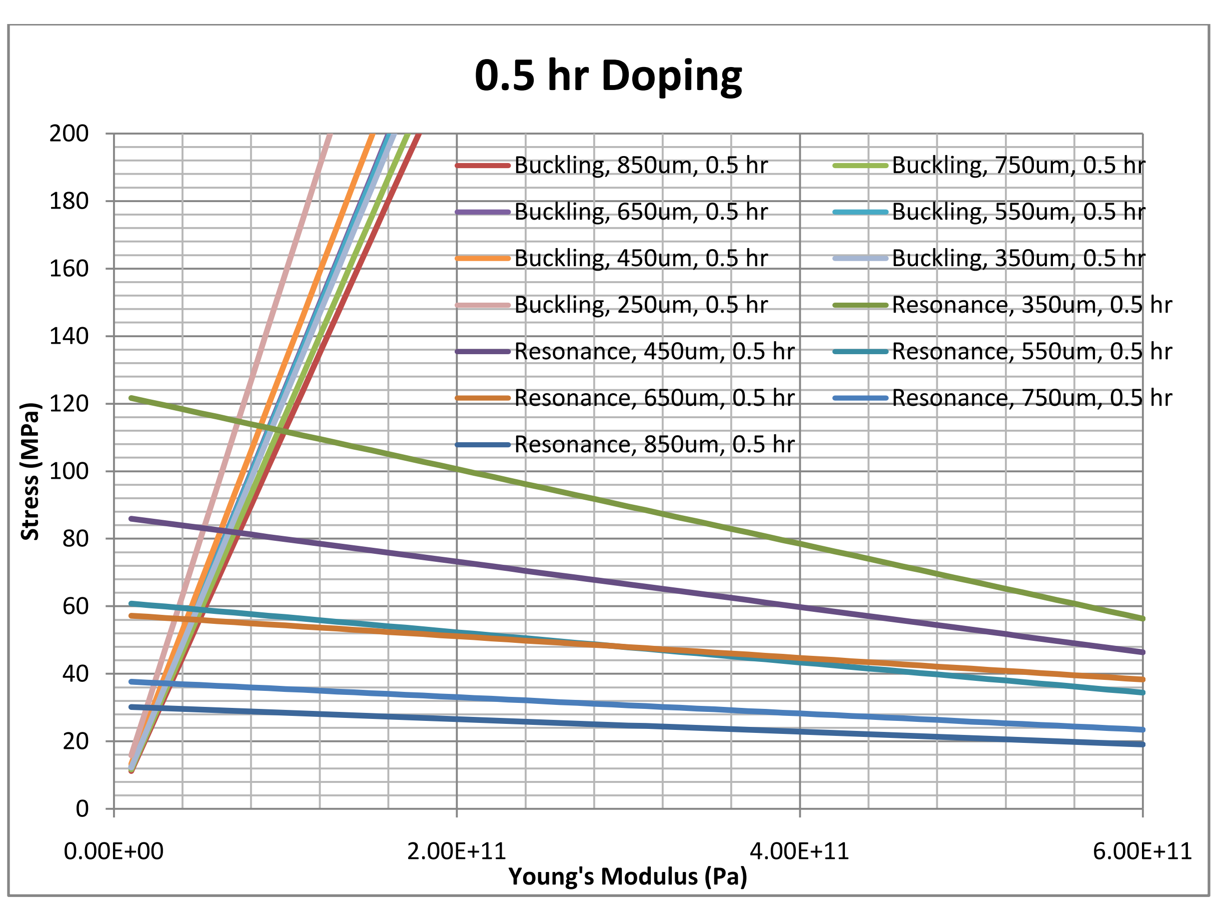

Figure 49. Possible combinations of stress and Young's modulus for 0.5 hour doped polysilicon as extracted from clamped-clamped beam buckling and resonant tests

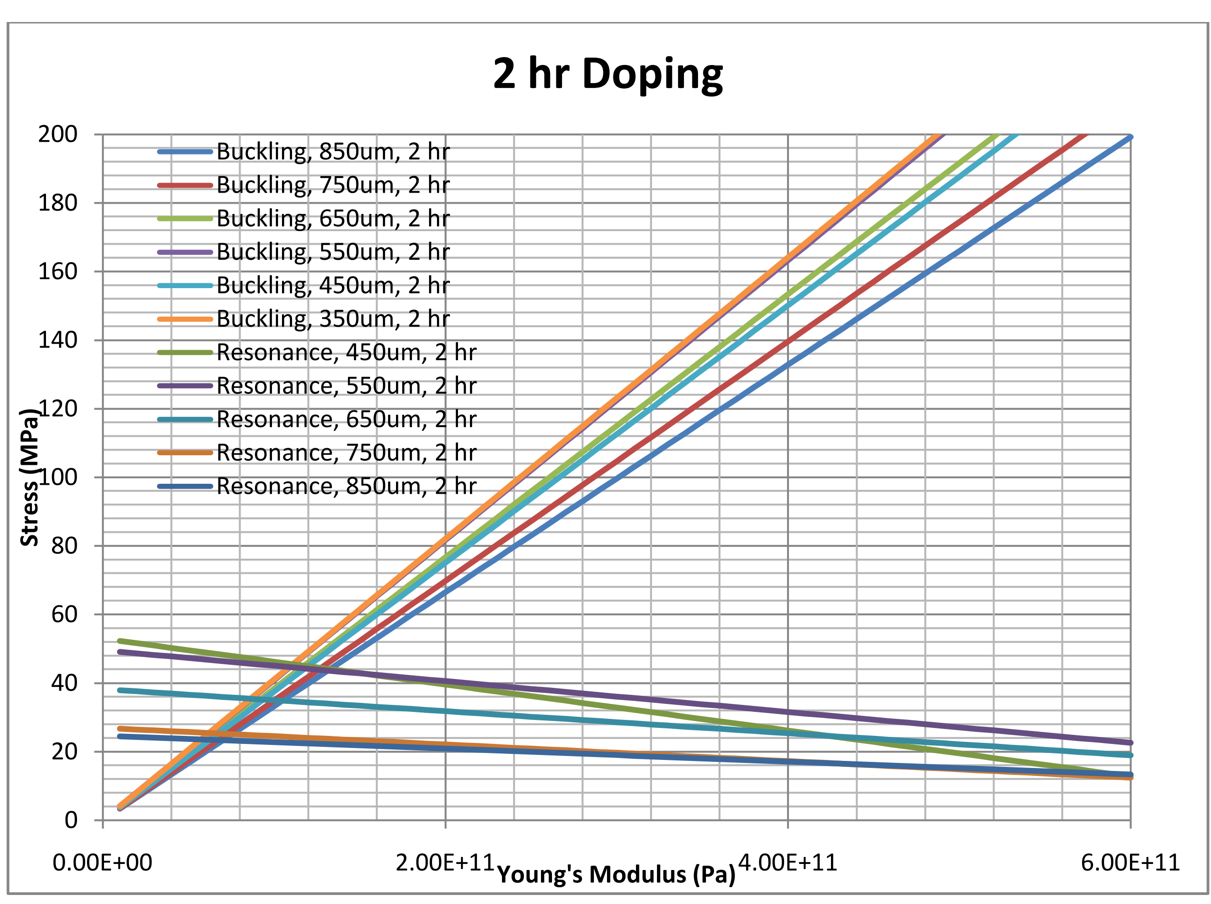

Figure 50. Possible combinations of stress and Young's modulus for 2 hour doped polysilicon as extracted from clamped-clamped beam buckling and resonant tests

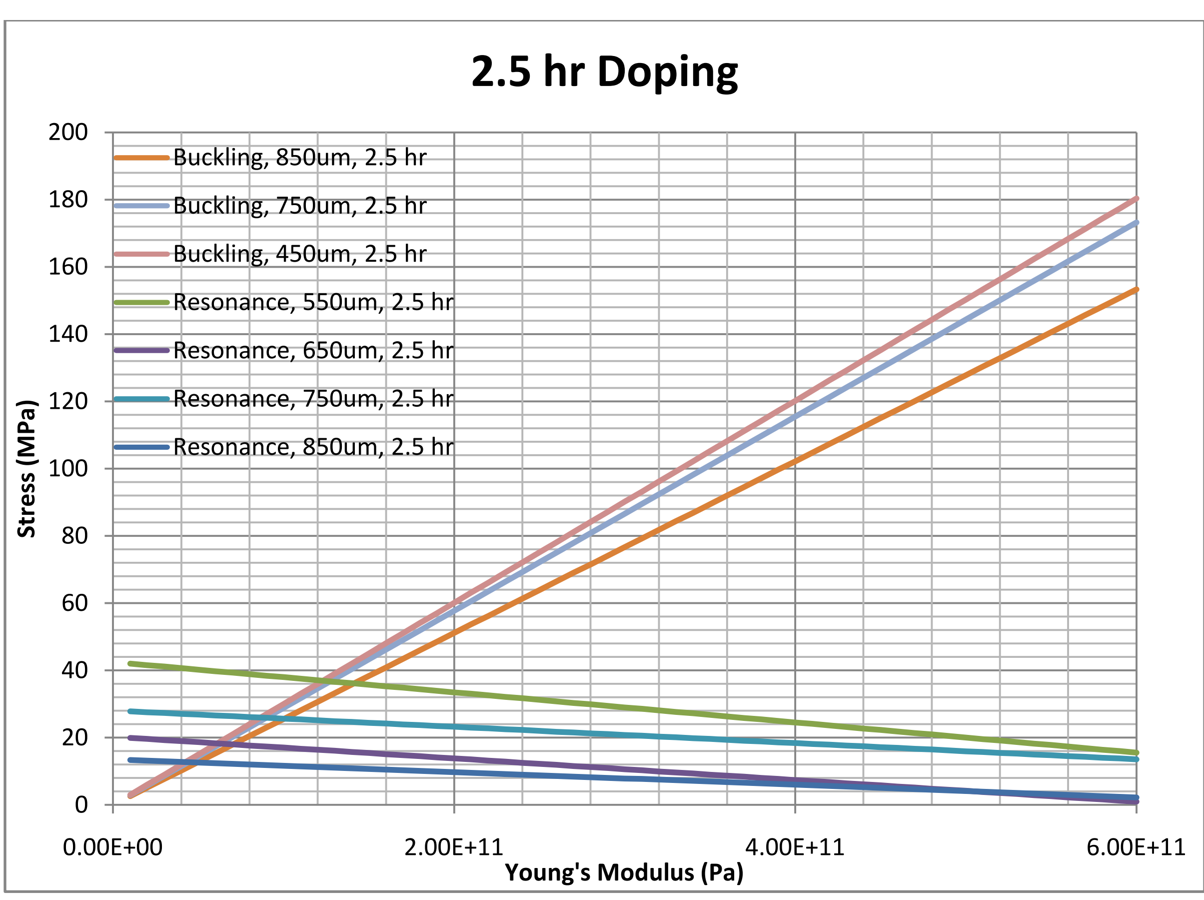

Figure 51. Possible combinations of stress and Young's modulus for 2.5 hour doped polysilicon as extracted from clamped-clamped beam buckling and resonant tests

Based on the experimental data, common solutions between the buckling and resonant frequency equations were found graphically and the ranges for the Young's modulus and residual stress were extracted.

Figure 52 shows the experimental range and the average Young's modulus for several doping times. Though the range of values for each doping concentration is fairly large, a general trend can be observed. The Young's modulus tends to increase with doping time. For the doping time of 2.5 hours the average Young's modulus value dips, however the range of values for that particular point is higher than the change in the Young's modulus over all the range of doping times, hence, this point should not be taken into consideration. The average values are significantly lower than expected, compared to the standard Young's modulus value of 160 GPa. Due to the high temperature pre-anneal

and diffusion grain growth and possibly re-crystallization occurred. Depending on the dominant crystal direction in the grains or overall structure the Young's modulus could be greatly reduced from the expected 160 GPa for polysilicon. Experimental conditions could also have contributed to a systematic offset causing a decrease in the extracted Young's modulus. For example, damping due to operation in air has not been considered in the analytical equation. Though the absolute values of the Young's modulus may not be accurate, the difference between dopant concentrations and the overall trend should still hold true. It can be concluded that the Young's modulus of undoped polysilicon which is doped for 2 hours using the technique presented in section 4.2 changes by approximately 50 GPa.

Figure 53 shows the experimental range and the average stress for several doping times. The range of data for the stress is smaller than that of the Young's modulus. The residual stress is decreasing with increasing doping time. This trend is expected as the undoped polysilicon is compressive and the introduction of phosphorus into silicon reduces compressive stress. The average stress values are within reasonable range for polysilicon, but, since they were extracted using the same data as was used for the Young's modulus it is likely that the absolute values suffer from the same inaccuracies. However, the observed trend should still remain valid and it can be concluded that the average residual stress of undoped polysilicon which is doped for 2.5 hours using the technique presented in section 4.2 changes by approximately 63 MPa.

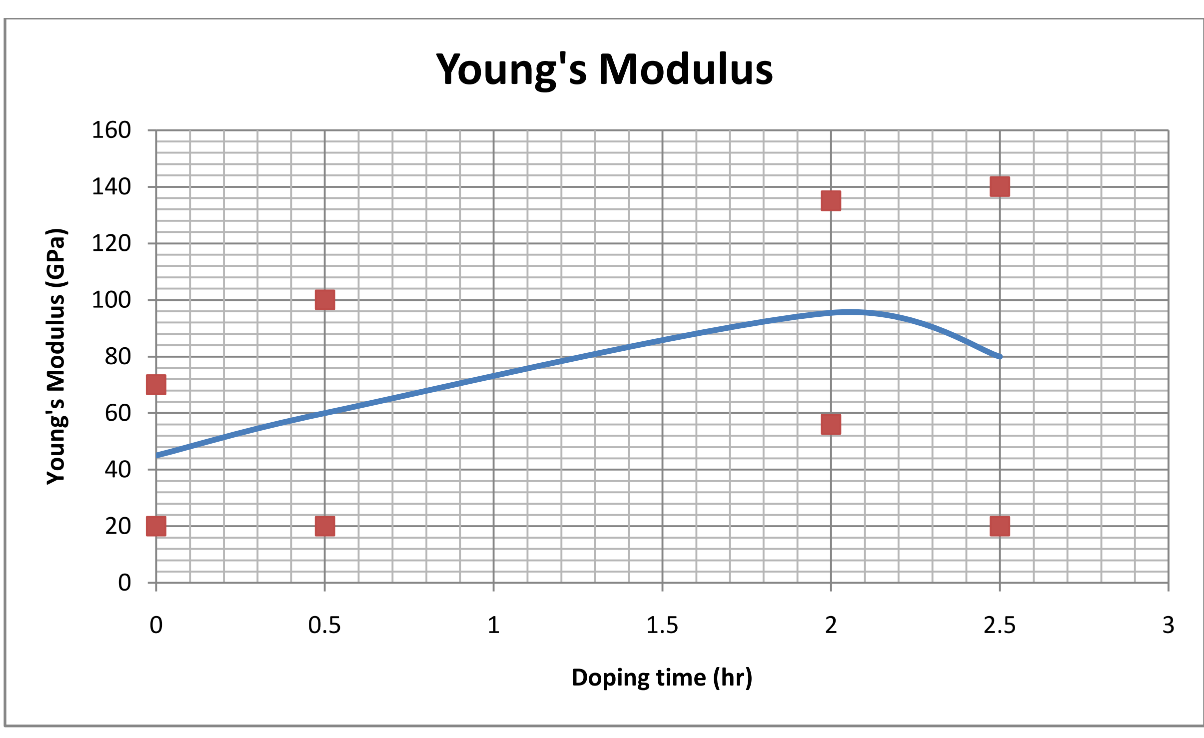

Figure 52. Average Young's moduli and experimental bounds extracted using the buckling and resonant test results for different doping times

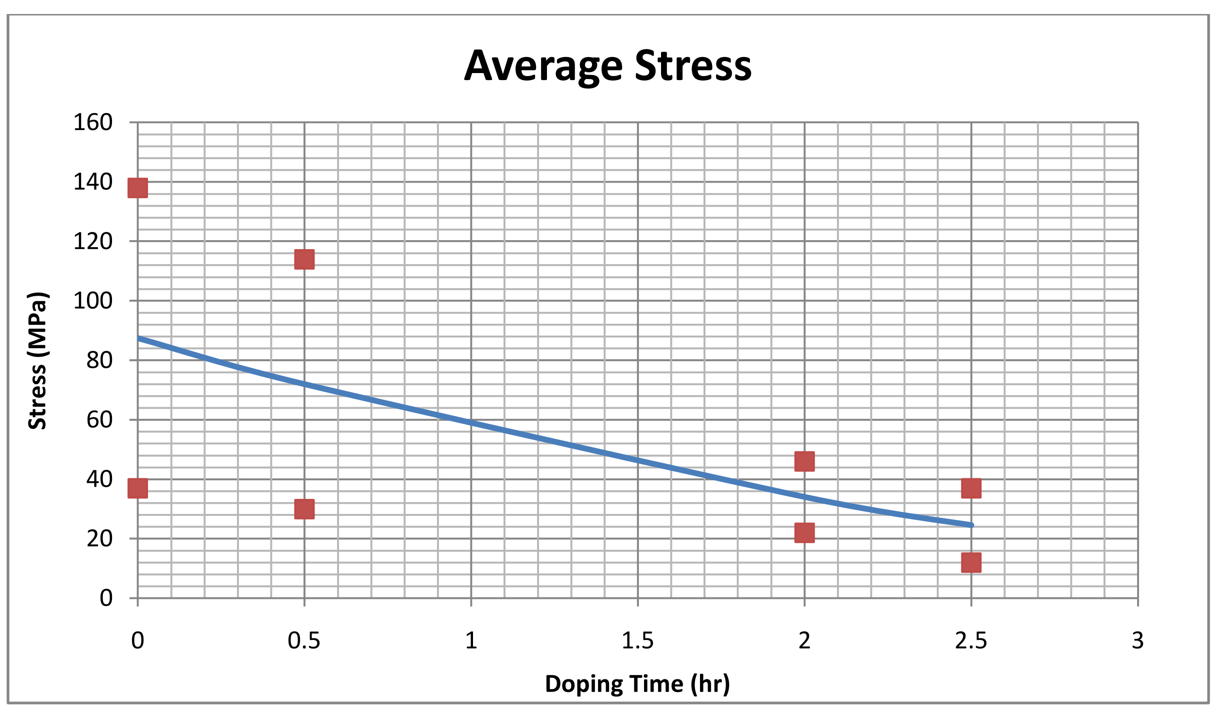

Figure 53. Average stress and experimental bounds extracted using the buckling and resonant test results for different doping times

5.3.4 Extracting Stress Gradient

Cantilever beams of different widths and lengths were fabricated. A set of cantilevers, as seen in Figure 54, contain 9 cantilevers of different lengths but the same widths. Figure 55 shows the layout of the cantilever beam chip and all the sets of cantilevers, widths 2μm, 5μm, 10 μm, 15 μm, 20 μm and 30 μm, fabricated. When cantilever beams are released, the residuals stress in the thin film is relieved by cantilever deformation. As stress is converted to strain the cantilever deformation can be related to the original stress in the thin film. The average stress in the film only serves to shrink or elongate the beam, however, the magnitude of this length change is smaller than the fabrication associated length uncertainty. Thus, the average stress cannot be extracted from cantilever beams. The effects of the stress gradient are much more noticeable as they produce significant beam curvature.

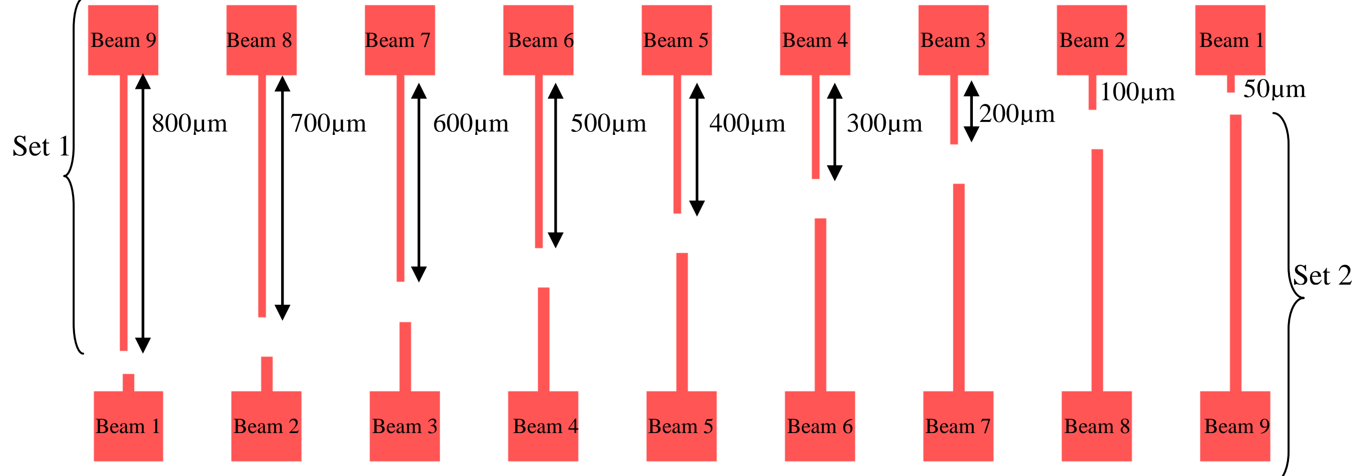

Figure 54. Cantilever beams

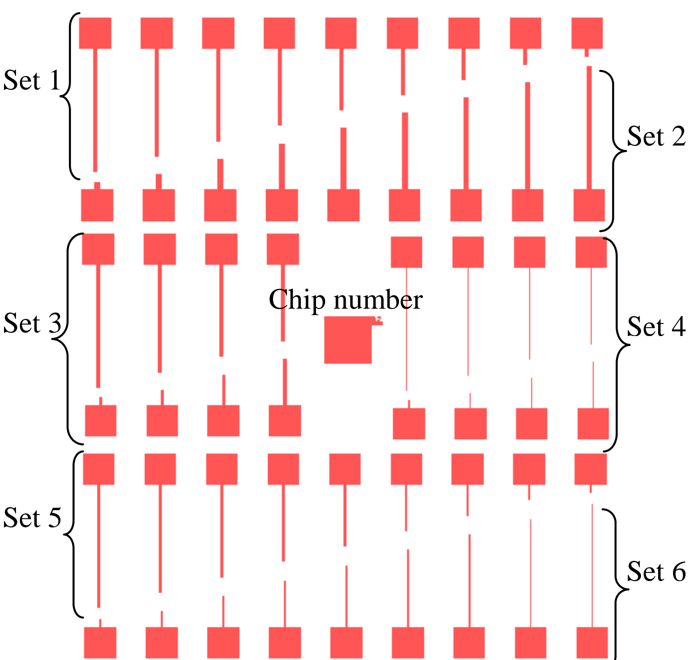

Figure 55. Cantilever beam chip

Though a critical point CO_2 dryer was used for some of the devices after the release process, some of the longer devices, particularly cantilever beams, still suffered from stiction. Figure 56 shows the profilometery results for a three 20 µm wide beams two of which, 800 µm and 700 µm long, are stuck

to the substrate. A few of the stuck beams could be released by carefully inserting a probe tip near the anchor of the beam and sliding it along the length of the beam until the entire structure came up.

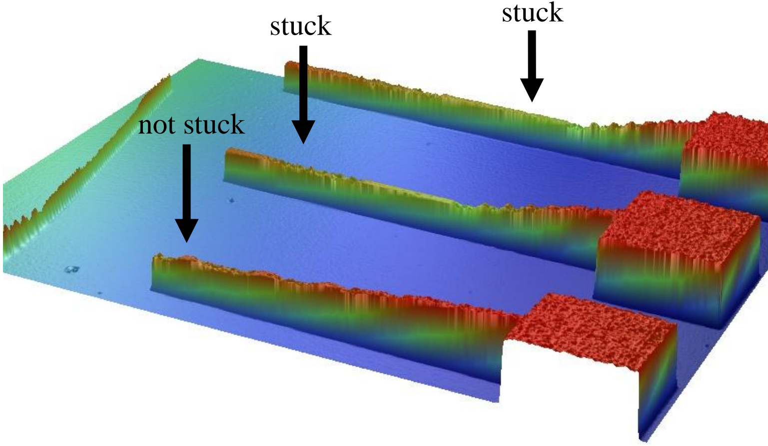

Figure 56. Profilometer results for three 20μm wide cantilever beams, the longer two beams are stuck

Most of the 2 μm and 5 μm beams did not survive the fabrication process and a good portion of the fabricated beams suffered from stiction. However, sufficient results from three doping concentrations, undoped, 0.5 hours and 1.5 hours, were available.

5.3.4.1 Undoped Cantilevers

The undoped cantilevers, shown in Figure 57, show the effects of a stress gradient. The concave down curvature suggests that they are more compressive at the bottom of the film than the top. As these beams have not undergone any doping, these effects are due to the other fabrication steps. The information obtained from these beams can be used as a comparison basis for the other doped devices. The cross sections of several undoped cantilevers of different lengths were extracted from the three dimensional data and are presented in Figure 58. Circular arcs were fitted to the curvature of the longer beams, and are also plotted in Figure 58.

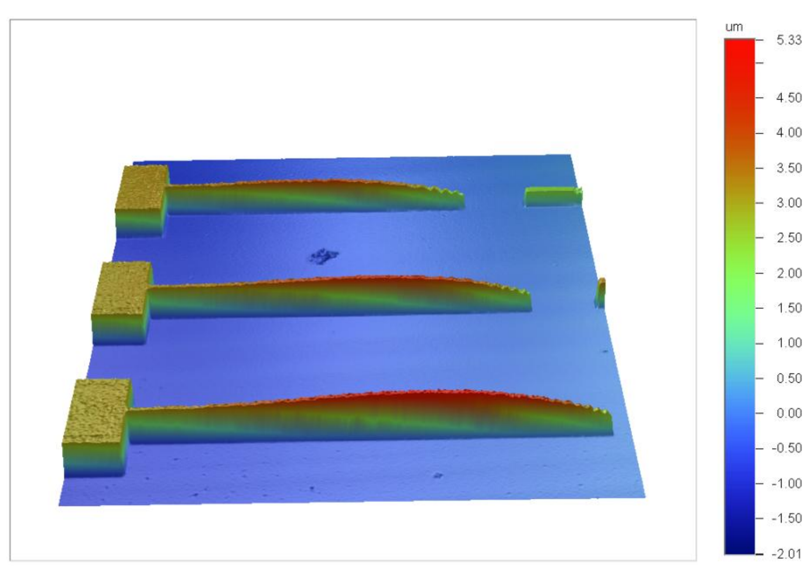

Figure 57. Three dimensional profilometer results of 800µm, 700µm and 600µm undoped cantilever beams

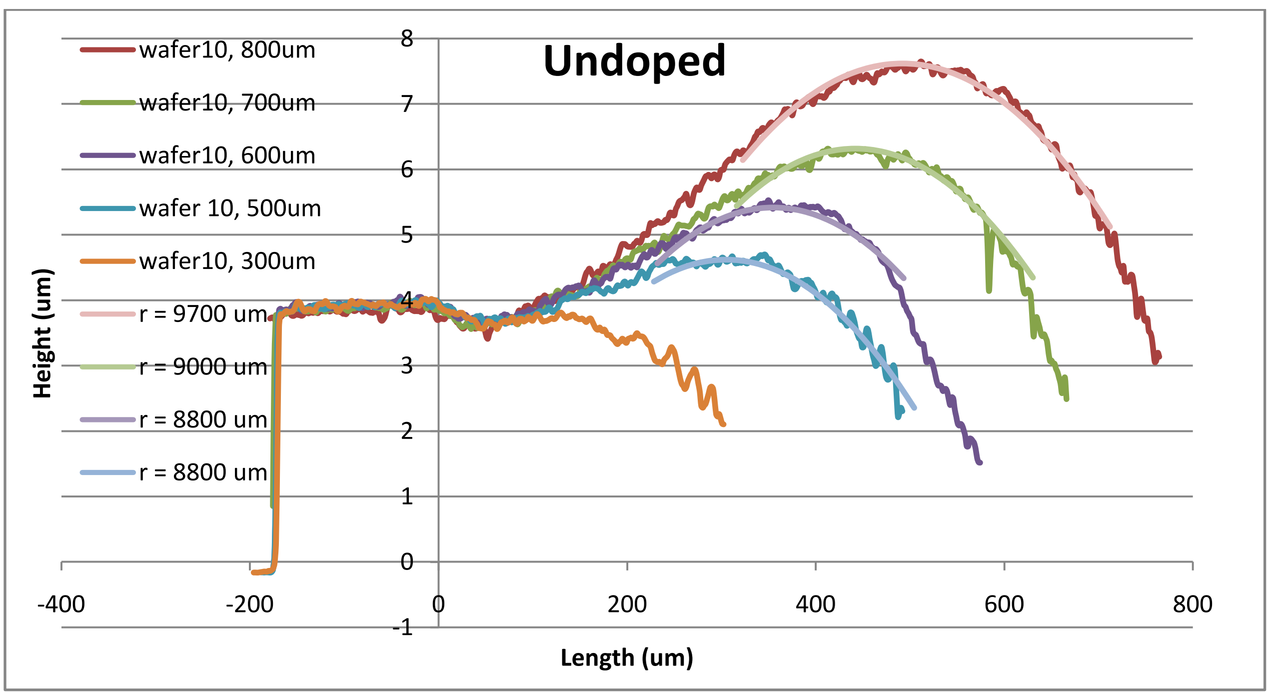

Figure 58. Cross sections of 800µm, 700µm, 600µm, 500µm, 300µm and 200µm long undoped cantilever beams from profilometer results and fitted circular arcs

5.3.4.2 0.5 Hour Cantilevers

The topology of cantilever beams from 0.5 hour doped polysilicon is shown in Figure 59. From the concave up deflection of the beams, it can be deduced that the film is more compressive at the top than at the bottom. This is a change from the concave down curvature of the undoped beams, which means that the introduced stress gradient due to the dopant atom distribution was higher than the intrinsic stress gradient of the material. The phosphorus atoms have a smaller radius than silicon atoms and are expected to contract the crystalline lattice found in the grains. The dopant profile from thermal diffusion indicates that for short diffusion times the dopant atoms do not permeate through the whole thickness of the film, as seen in Figure 18, which means that a high stress gradient is introduced. This explains the concave up curvature of the beams.

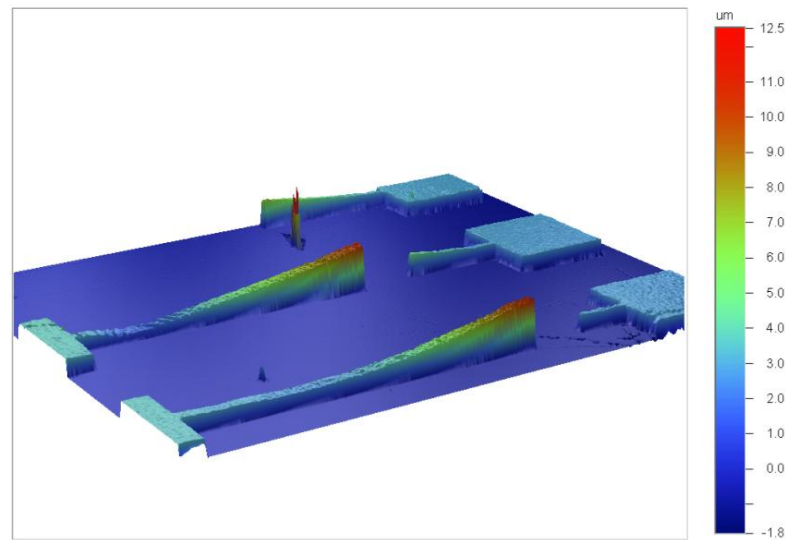

Figure 59. Three dimensional profilometer results of 800µm, 700µm, 300µm, 200µm and 100µm cantilever beams from a wafer with 0.5 hours of doping

The cross sections of several beams and the fitted circular arcs are shown in Figure 60. Note that the curvature of the 200µm beam is so similar to the 800µm that it is difficult to see. The stress gradient can be calculated using Equation 19.

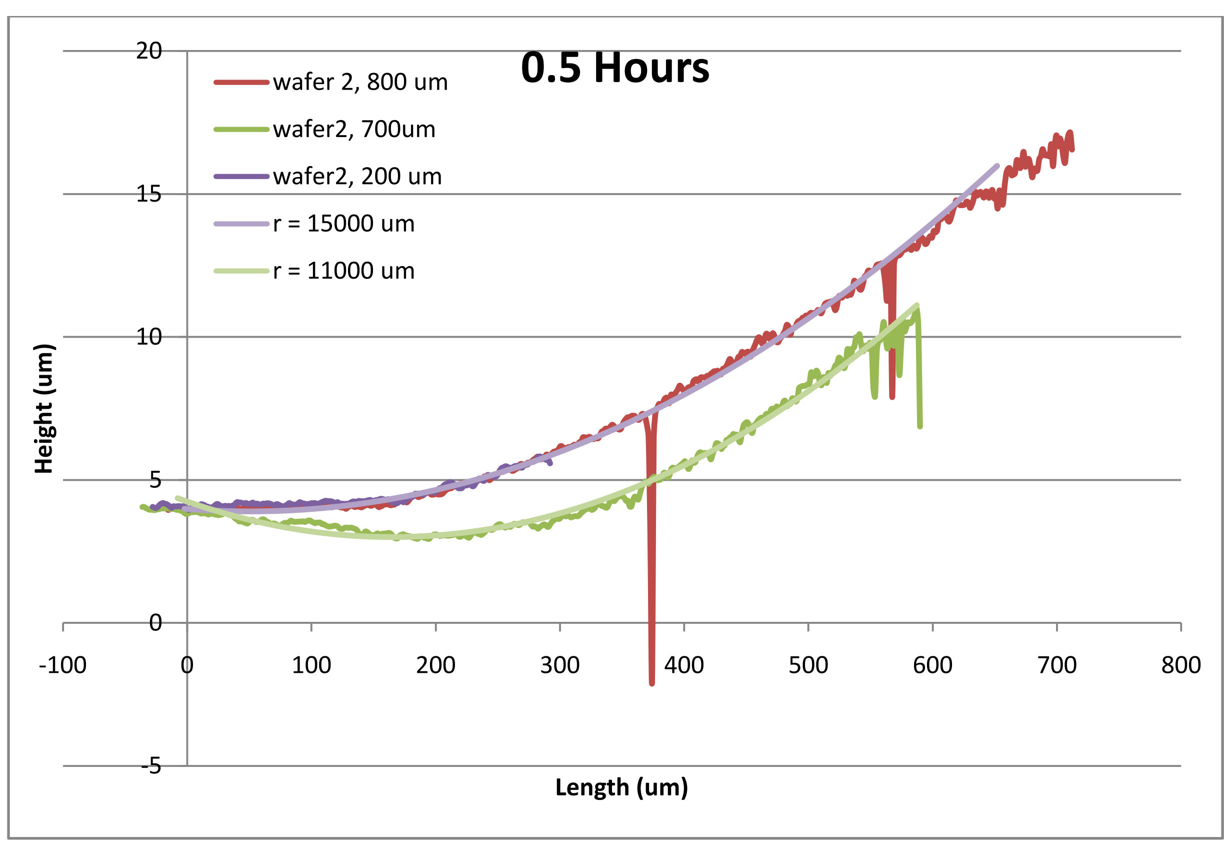

Figure 60. Cross sections of 800μm, 700μm, and 200μm long 0.5 hour doped cantilever beams from profilometer results and fitted circular arcs

5.3.4.3 1.5 Hour Cantilevers

The three dimensional depiction of several cantilevers fabricated from 1.5 hour doped polysilicon are shown in Figure 61. The curvature has again returned to a concave down configuration, meaning that the intrinsic residual stress gradient is higher than the dopant stress gradient. As Figure 18 shows, the dopant distribution through the thickness of the film is more uniform due to the longer diffusion time. This means that the introduced stress gradient is smaller though the introduced average tensile stress is higher. Figure 62 shows the cross-sections of several beams and fitted circular arcs.

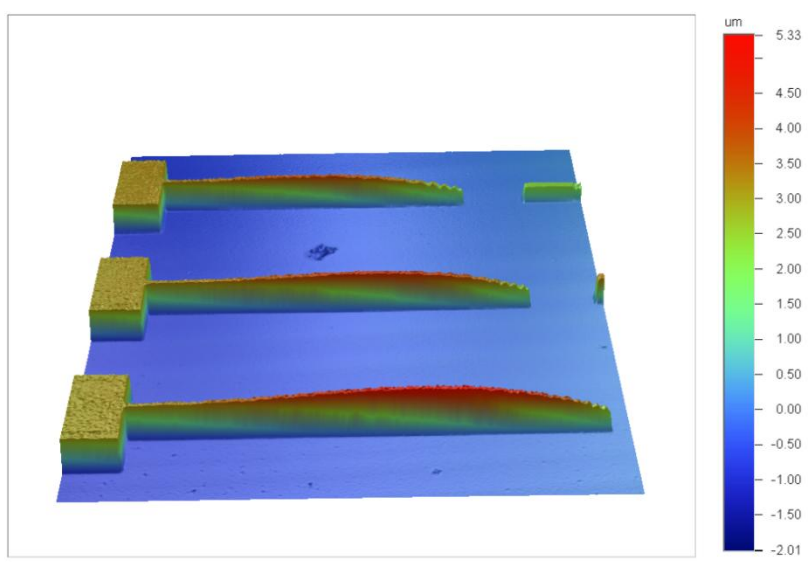

Figure 61. Three dimensional profilometer results of 800µm, 700µm and 600µm cantilever beams from a wafer with 1.5 hours of doping

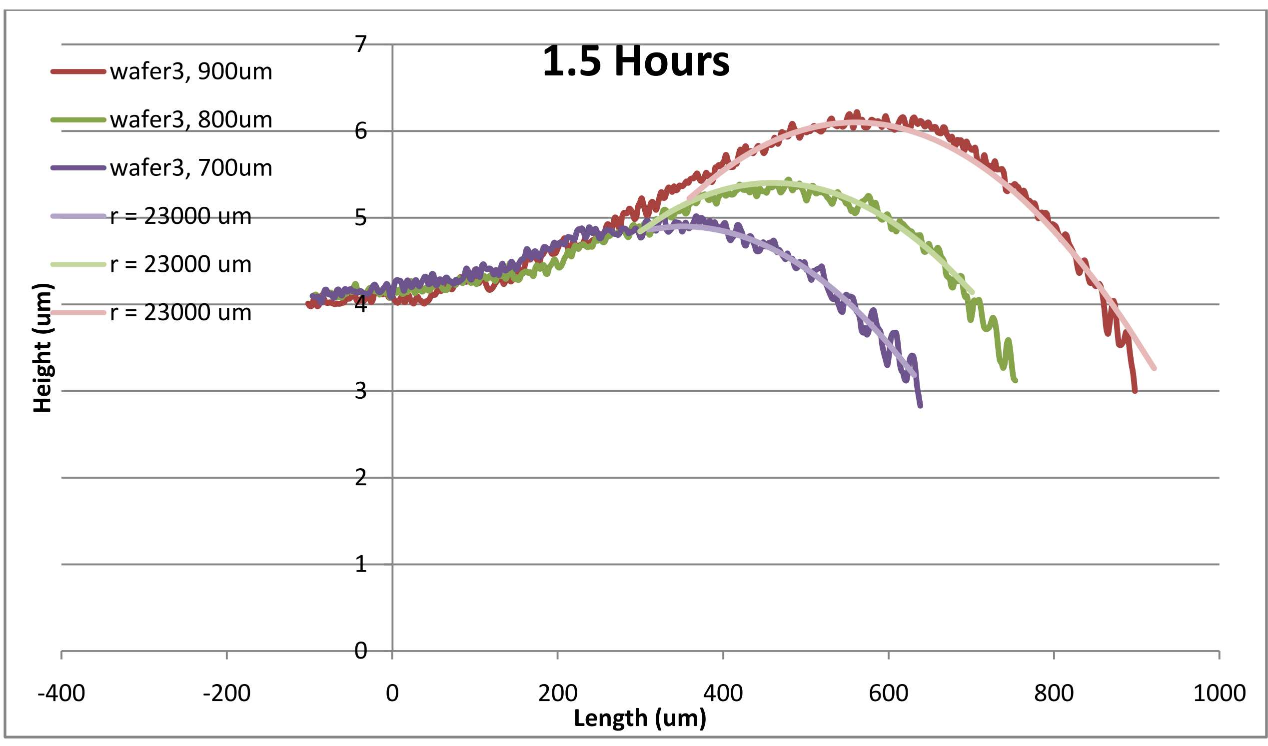

Figure 62. Cross sections of 900µm, 800µm, and 700µm long 1.5 hour doped cantilever beams from profilometer results and fitted circular arcs

5.3.4.4 Comparison

Using Equation 19 and the average radii of curvature of the fitted arcs for each of the concentrations, the stress gradient can be extracted. Using the Young's moduli calculated in section 5.3.3 for each of the respective doping concentrations the blue curve in Figure 63 is obtained. Since the extracted Young's moduli were lower than expected or previously reported in literature, the same calculations for the stress gradient were also performed using a standard value of 160 GPa for the Young's modulus of polysilicon. The result is the red curve in Figure 63.

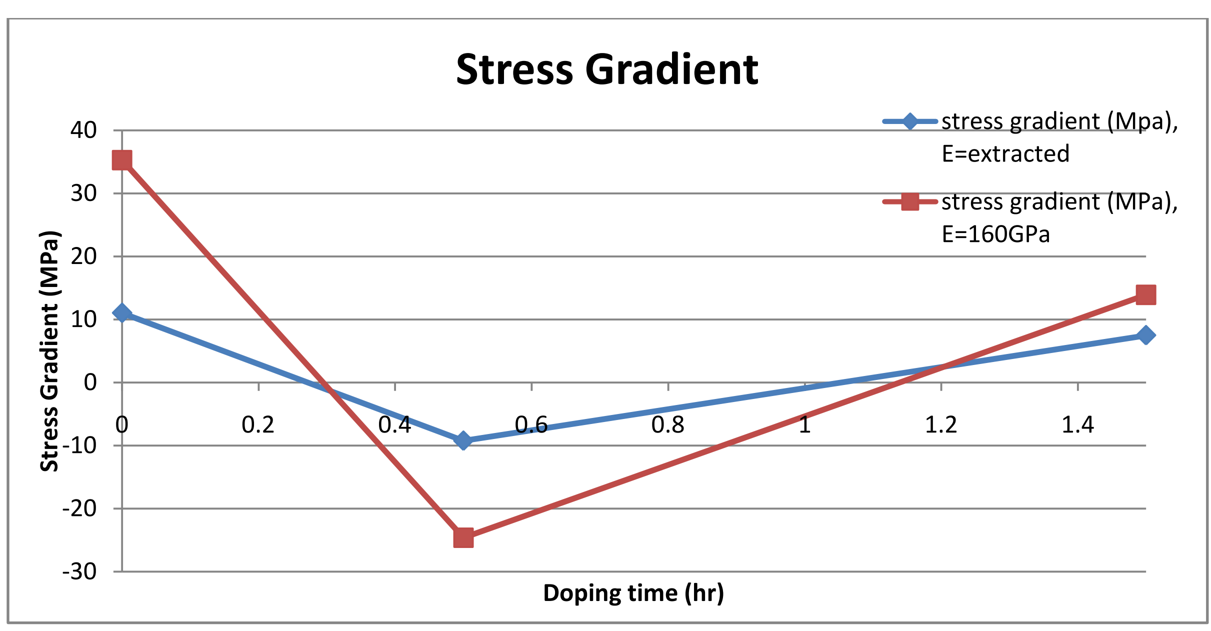

Figure 63. Stress gradient calculated using the circular arcs fitted to cantilever beam bending

With both Young's modulus assumptions, the stress gradient is highest for the undoped polysilicon, being more compressive at the bottom than the top. The gradient changes sign, as indicated by the change in concavity of the cantilever beams, for 0.5 hours of doping becoming more compressive at the top than the bottom. This is explained by the introduction of a large dopant distribution gradient due to the short doping time. The introduced gradient is enough to counteract the initial stress gradient of undoped polysilicon. With longer doping time, the dopant profile becomes more even and the introduced gradient is smaller, though the average dopant concentration and stress are higher. Due to that, the gradient introduced due to 1.5 hours of doping is not high enough to counteract the initial stress gradient, but does reduce it. Though data is not available for the higher doping concentrations, it is expected that their dopant profiles will be even more consistent and will introduce smaller stress gradients. Hence, the overall stress gradient would increase as the intrinsic fabrication-related stress gradient dominates.

Chapter 6
Conclusions and Future work

A suite of devices for characterizing the Young's modulus, average residual stress and stress gradient has been designed and used to extract the material properties of phosphorus doped polysilicon thin films. It has been determined that the Young's modulus of polysilicon doped for 2 hours increases by approximately 50GPa and the average stress of polysilicon doped for 2.5 hours decreases by approximately 63 MPa. The change in the Young's modulus residual stress is quite significant which makes doping a very promising technique for changing the mechanical properties of thin films and increasing the sensitivity of sensors.

In order to build on the work done, improve the data and increase the certainty of the drawn conclusions several ameliorations and additions should be considered. The resonant test experiments should be performed in a chamber where the environmental conditions, such as pressure, humidity, temperature are controlled and can be kept constant for each sample. This would likely reduce the scatter of the data reduce the number of variables that may be impacting the outcome of the experiments. Additionally, the tests can be run at various temperatures to determine the temperature dependence of the material properties and whether they vary with doping. Devices for extracting the coefficient of thermal expansion should be redesigned in order to withstand the fabrication process and be used to extract the coefficient of thermal expansion. Using this new setup, a larger number of resonant experiments should be performed in order for the data to obtain statistical validity.

The grain structure of the material should be studied in order to ascertain that the grain sizes between differently doped samples do not change. This should already be the case due to the fact that they were fabricated in the same run and were annealed for the same amount of time; however, validating this point would remove future doubts. Additionally, finding the dominant crystal orientation would be useful in order to verify that the low average value of Young's modulus is due to re-crystallization. The chemical composition of the material should be studied using secondary ion mass spectrometry, as this is a better measure of chemical dopant concentration than electrical measurements and extrapolation. Additionally, the chemical composition in the grain and at the grain boundary should be studied separately to see the amount dopant segregation. The electrical and mechanical effects of dopant atoms in the grain and at the grain boundary differ, and knowing the ratio of the

concentrations could shed light on the reasons behind the experimental results. Furthermore, a post-diffusion anneal could be used in order to reduce some of the intrinsic stresses in the film. This would reduce the out-of-plane deflection of the test structures and reduce the discrepancy between the assumptions made in the analytical model and the physical devices.

Additional samples could be made in order to further zero in on the effects of the dopant atoms themselves and try to dissociate those effects from the fabrication process. Of course, all the above mentioned measures should be implemented in order to track the grain size, chemical content and other factors. First, a polysilicon layer produced at a different facility could be used. Perhaps several different polysilicon samples deposited at different conditions could be doped and tested. Studying the effects of doping on different polysilicon could confirm the currently held belief that the effect of doping will be transferable, or, perhaps it would show that certain polysilicons react differently to doping. MEMS designers could use this information in order to pick the most appropriate polysilicon for their applications. Additionally, various thicknesses of polysilicon could also be studied. Next, the actual doping technique could be changed in order to see how the fabrication process affects the material properties. In this work, thermal diffusion was used and the temperature parameter was kept constant for all samples while the diffusion time varied. In future work, the temperature could be varied between instead of time, or, a different constant temperature could be used. The effects of an ambient with a different O_2 to N_2 ratio could also be studied.

Also, the way that the dopants are introduced into the host could be changed altogether. For example, ion implantation instead of thermal diffusion could be used. The effects of beam dose, energy, post-annealing could be studied. In-situ doping could also be studied. The data from these different doping techniques could be compared to see if there is a consistent difference between identical dopant concentrations that could be attributed to different doping techniques. The effects of grain boundaries can simultaneously be studied by performing the above experiments using single crystalline silicon at the same time as polycrystalline.

Once the effect of phosphorus on polysilicon has been thoroughly studied and an empirically derived model for the change in Young's modulus with phosphorus concentration and other factors has been derived one could use a different common silicon dopant, such as boron or arsenic, could be used to

test the model. Since this work was performed in order to determine the usability of doping a technique to change the material properties of high temperature sensors one could perform the above experiments using silicon carbide instead of silicon. The congruency of dopant-related changes between the two materials could be studied and used to draw a general conclusion about the similarity of the two materials. The final step would be to apply the obtained knowledge to design a better, more sensitive temperature pressure sensor for harsh environments.

Appendix A

MATLAB CODE FOR AUTOMATING RESONANT FREQUENCY MEASUREMENTS

```
% Create a GPIB object.
obj1 = instrfind('Type', 'gpib', 'BoardIndex', 7, 'PrimaryAddress', 30, 'Tag', '');
% Create the GPIB object if it does not exist
% otherwise use the object that was found.
if isempty(obj1)
   obj1 = gpib('AGILENT', 7, 30);
else
   fclose(obj1);
   obj1 = obj1(1)
end

% Create a GPIB object.
obj2 = instrfind('Type', 'gpib', 'BoardIndex', 7, 'PrimaryAddress', 7, 'Tag', '');
% Create the GPIB object if it does not exist
% otherwise use the object that was found.
if isempty(obj2)
   obj2 = gpib('AGILENT', 7, 7);
else
   fclose(obj2);
   obj2 = obj2(1)
end

% Connect to instrument object, obj1.
fopen(obj2);
```

```
% Connect to instrument object, obj1.
fopen(obj1);

file1 = fopen('output.csv','a');
file2 = fopen('voltage_comp.csv','r');
%file3 = fopen('actual_voltage.csv','a');
fprintf(obj1, 'OUTPUT ON');
for freq = 10:800

  volt = str2double(fgetl(file2));
  if (volt > 10)
    volt=10;
  end
  fprintf(obj1, 'APPL:SIN %f KHZ', freq);
  %fprintf(obj1, 'VOLT:OFFS 2.5');
  fprintf(obj1, 'VOLT %f',volt);
  %fprintf(file3, '%3.6f\n', volt);
  fprintf(obj2, 'TRIGGER:SOURCE CHAN1');
  pause(0.2)

  fprintf(obj2,'DIGITIZE CHAN1, CHAN2');

  fprintf(obj2,'AUTOSCALE');
  fprintf(obj2, 'TRIGGER:SOURCE CHAN1');
  voltage_amplitude_string = query(obj2, 'MEASURE:VAMPLITUDE? CHANNEL2');
  voltage_amplitude = str2double(voltage_amplitude_string);
  fprintf(file1,'%6f, %3.5f,%3.5f\n',freq, voltage_amplitude,
voltage_amplitude*25000/(freq*1000));
```

```
end

fprintf(obj1, 'OUTPUT OFF');
fclose(file1);
fclose(file2);
fclose(obj1);
delete(obj1);
fclose(obj2);
delete(obj2);
```

Appendix B

0 HOURS DOPING RESONANT BEAM TEST RESULTS

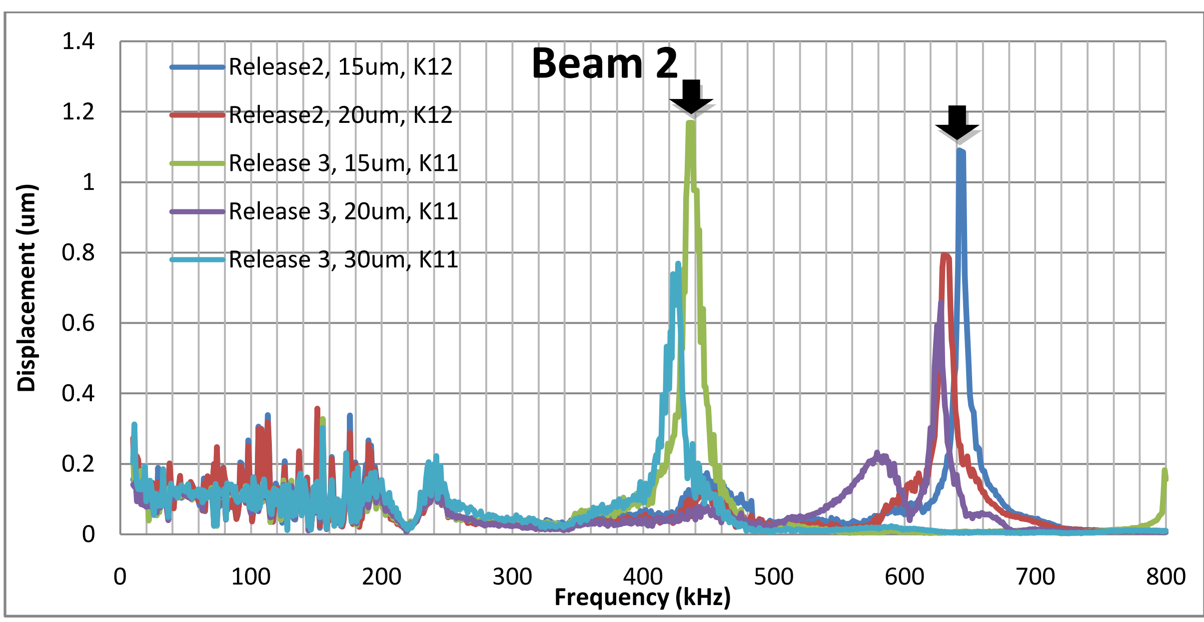

Figure 64. Frequency response of several 250µm long clamped-clamped beams with 0 hours of doping

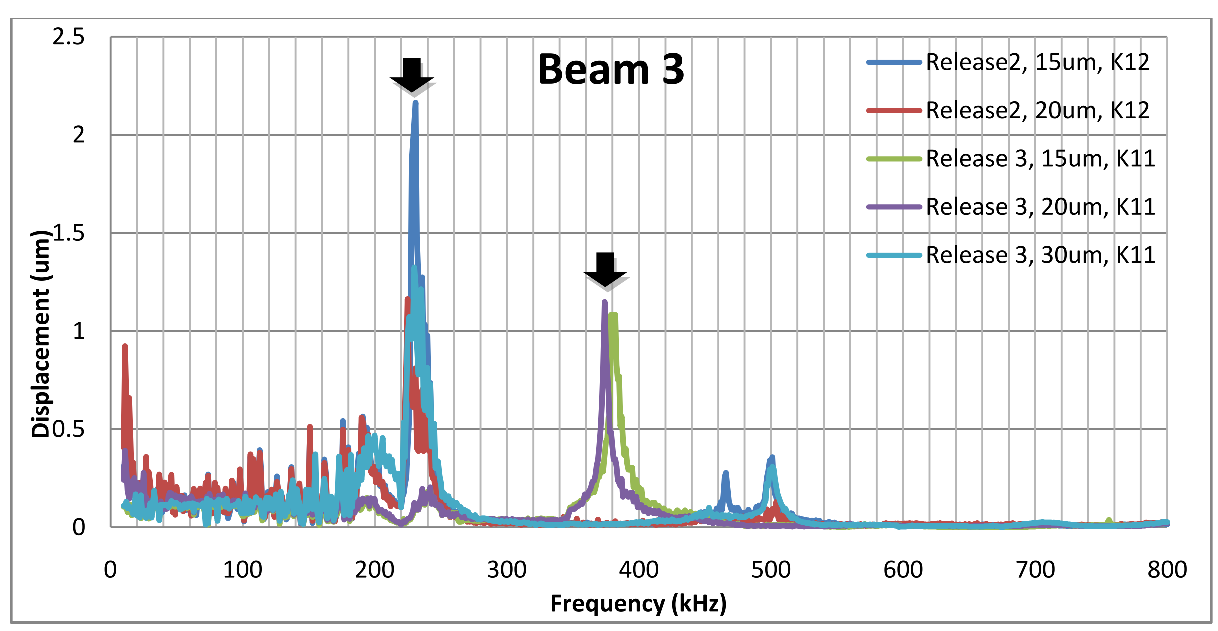

Figure 65. Frequency response of several 350μm long clamped-clamped beams with 0 hours of doping

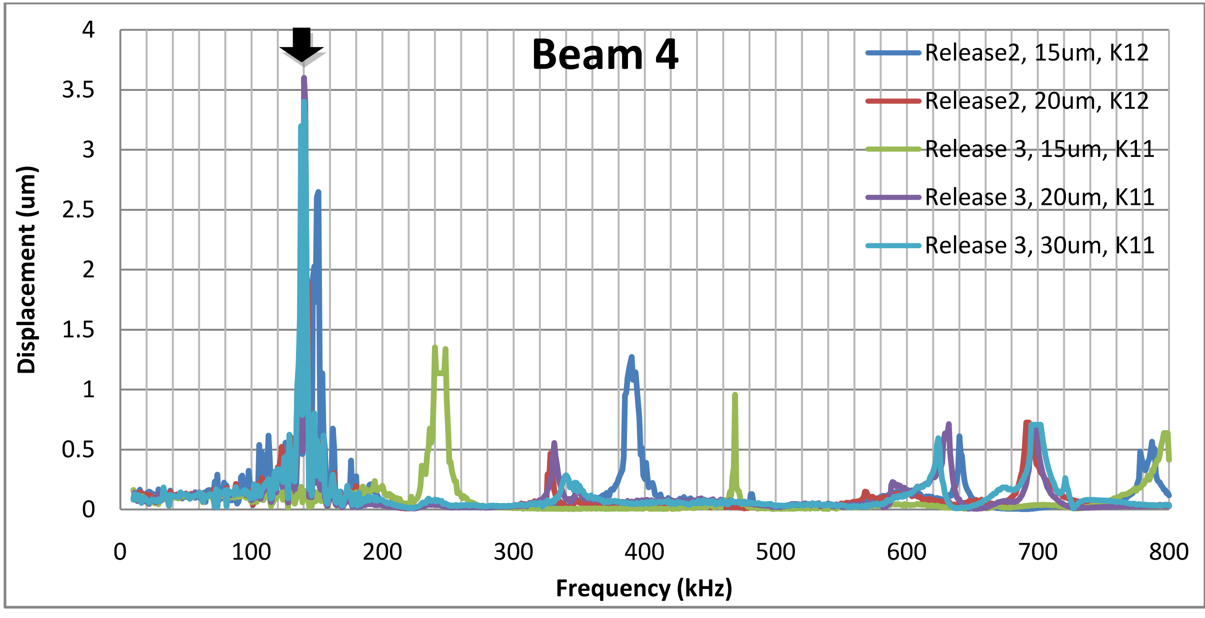

Figure 66. Frequency response of several 450μm long clamped-clamped beams with 0 hours of doping

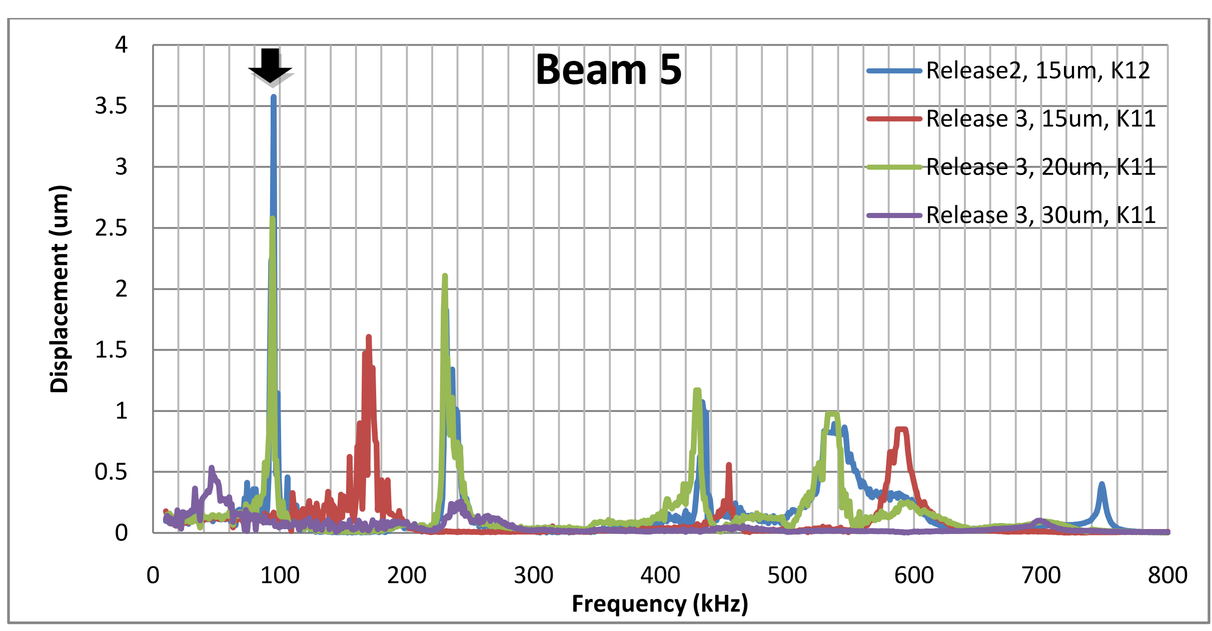

Figure 67. Frequency response of several 550µm long clamped-clamped beams with 0 hours of doping

0.5 HOURS DOPING RESONANT BEAM TEST RESULTS

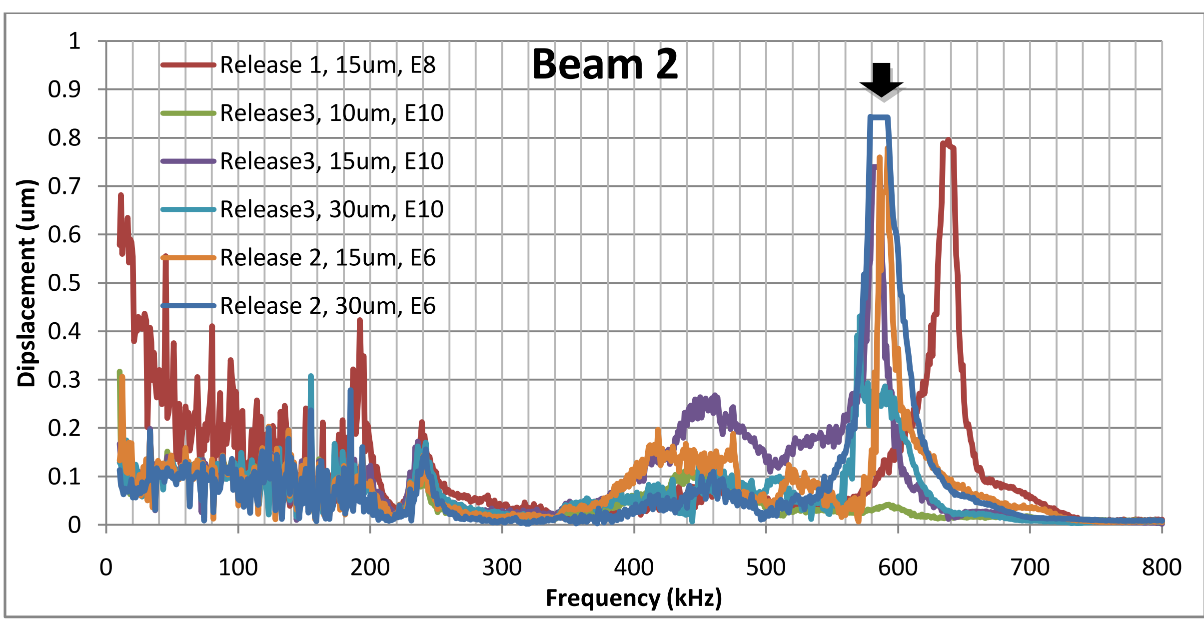

Figure 68. Frequency response of several 250µm long clamped-clamped beams with 0.5 hours of doping

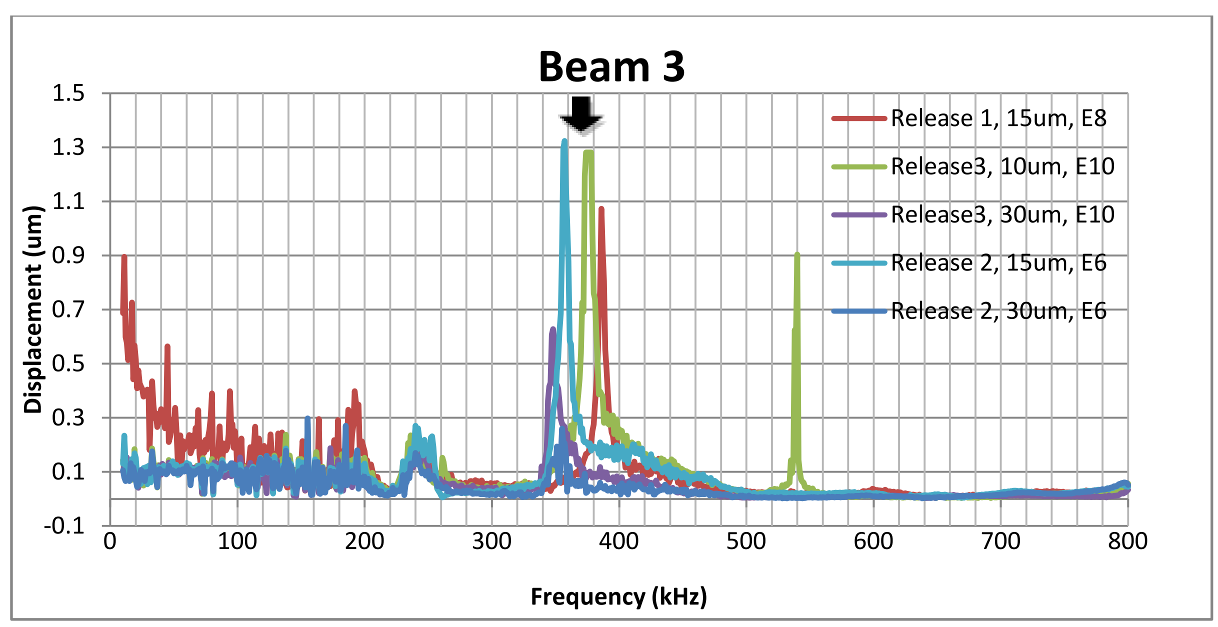

Figure 69. Frequency response of several 350µm long clamped-clamped beams with 0.5 hours of doping

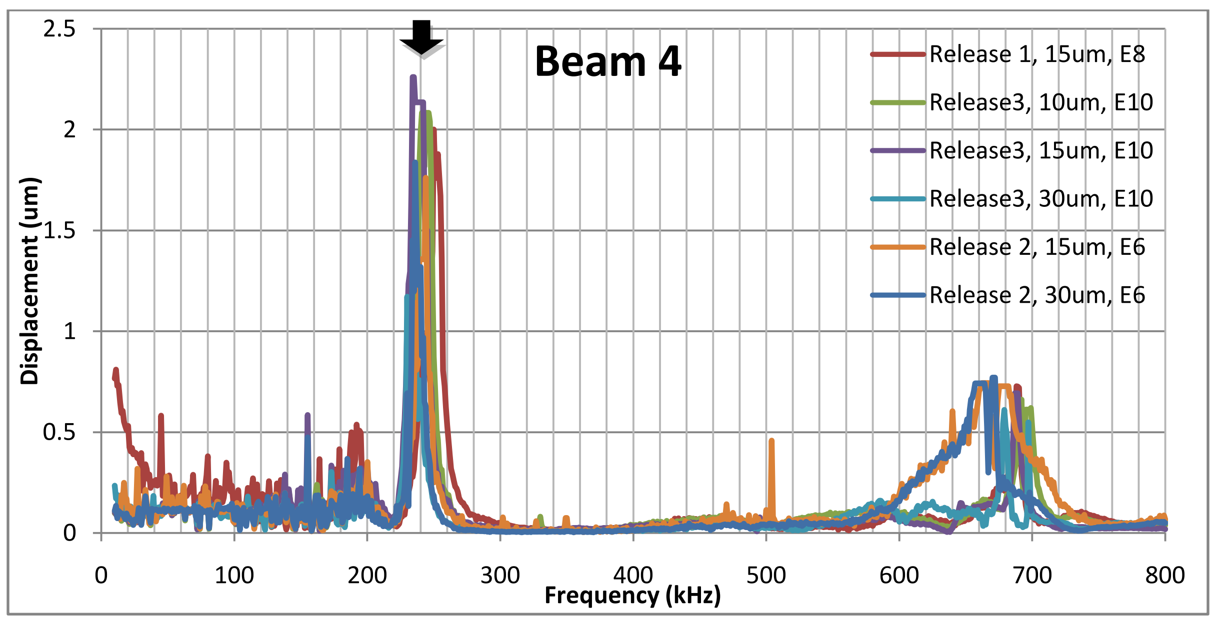

Figure 70. Frequency response of several 450µm long clamped-clamped beams with 0.5 hours of doping

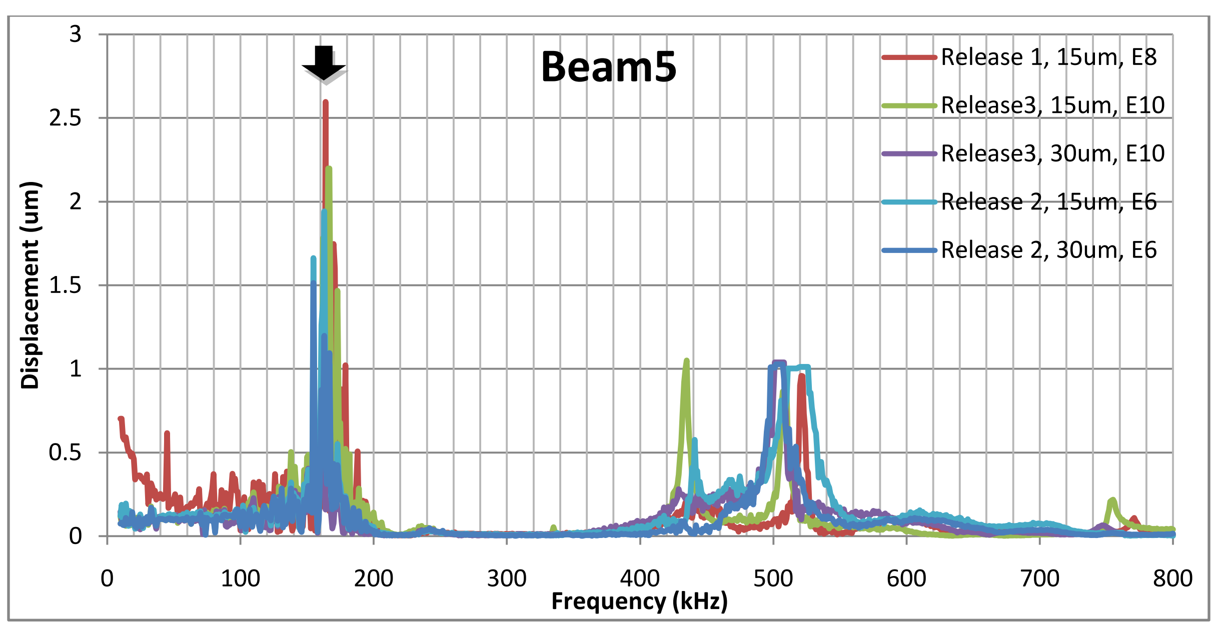

Figure 71. Frequency response of several 550μm long clamped-clamped beams with 0.5 hours of doping

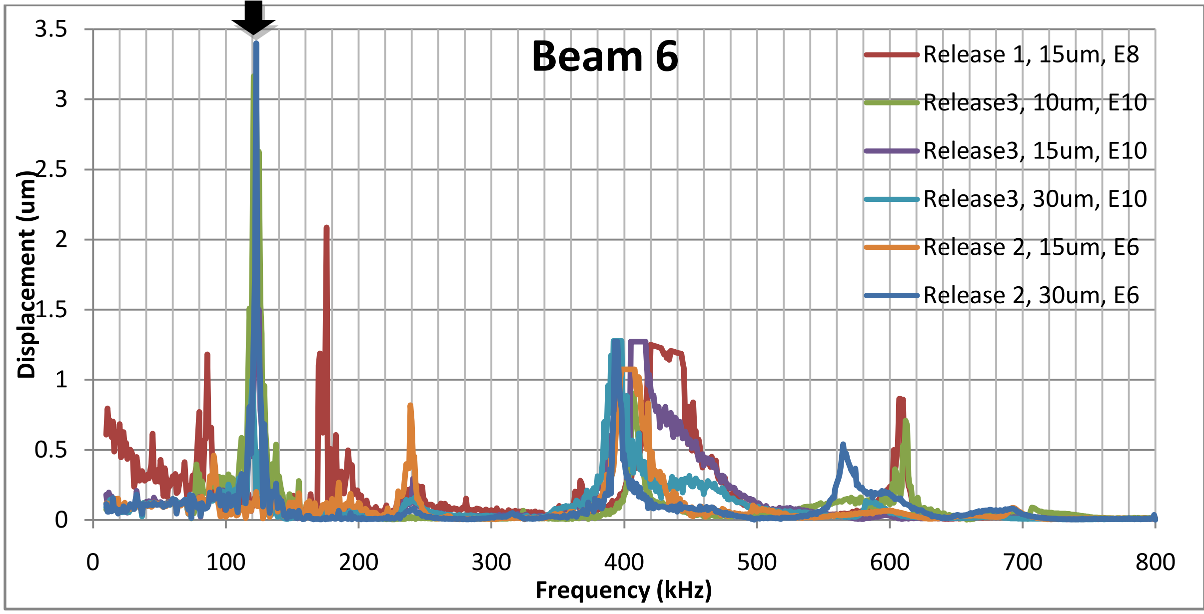

Figure 72. Frequency response of several 650μm long clamped-clamped beams with 0.5 hours of doping

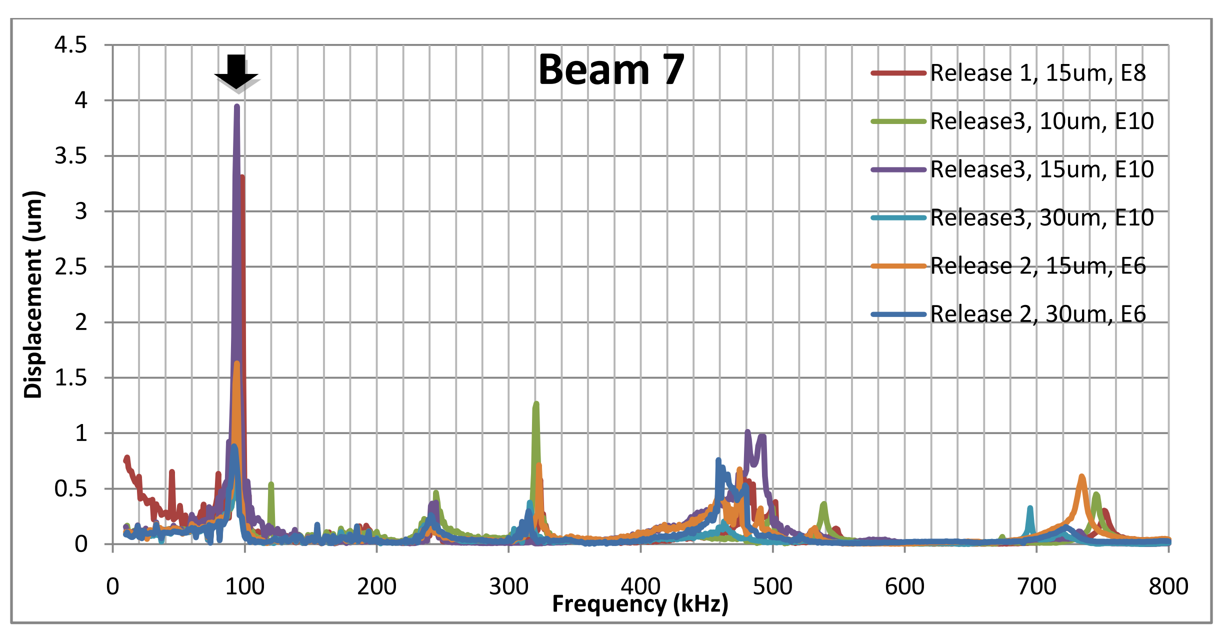

Figure 73. Frequency response of several 750μm long clamped-clamped beams with 0.5 hours of doping

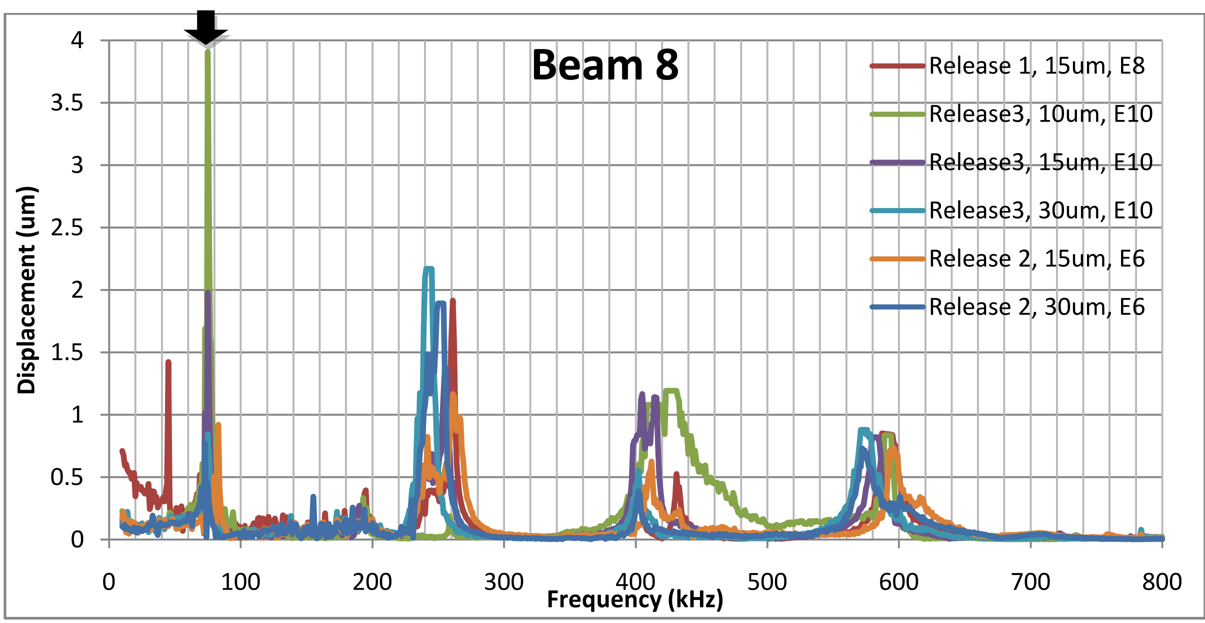

Figure 74. Frequency response of several 850μm long clamped-clamped beams with 0.5 hours of doping

2 HOURS DOPING RESONANT BEAM TEST RESULTS

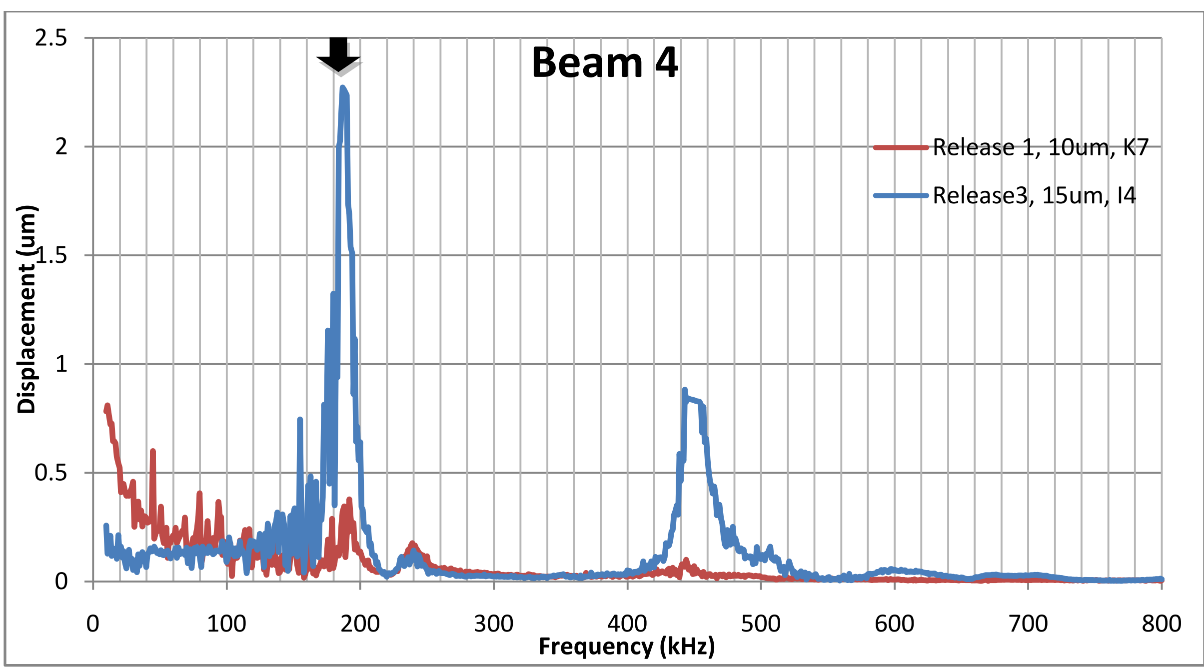

Figure 75. Frequency response of several 450µm long clamped-clamped beams with 2 hours of doping

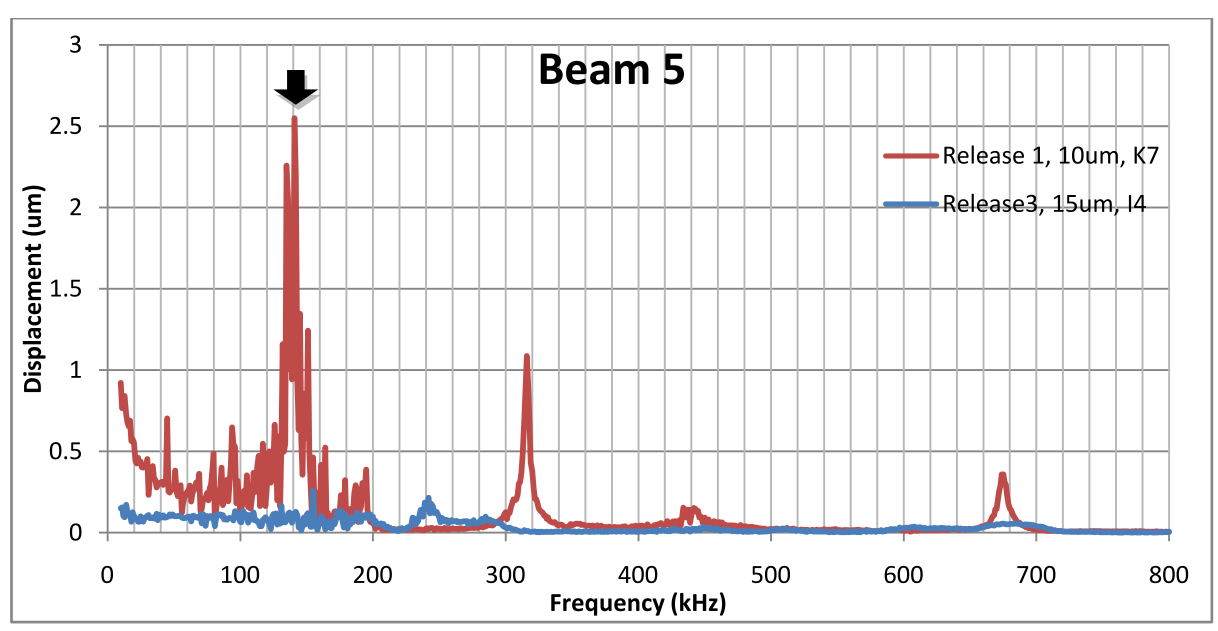

Figure 76. Frequency response of several 550µm long clamped-clamped beams with 2 hours of doping

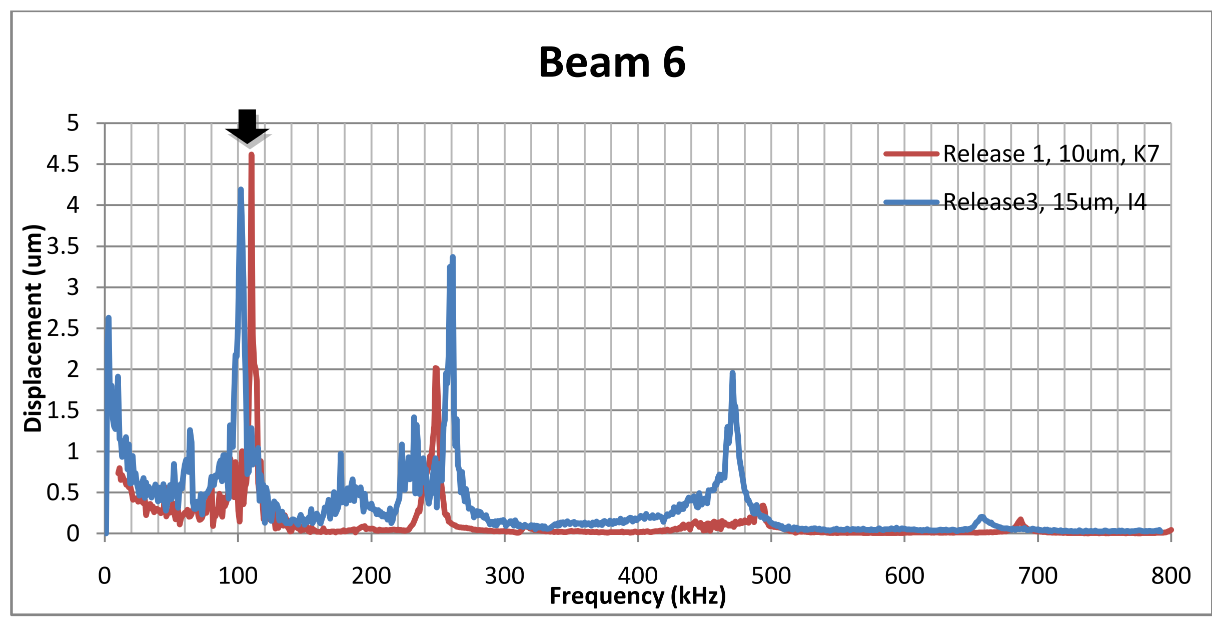

Figure 77. Frequency response of several 650µm long clamped-clamped beams with 2 hours of doping

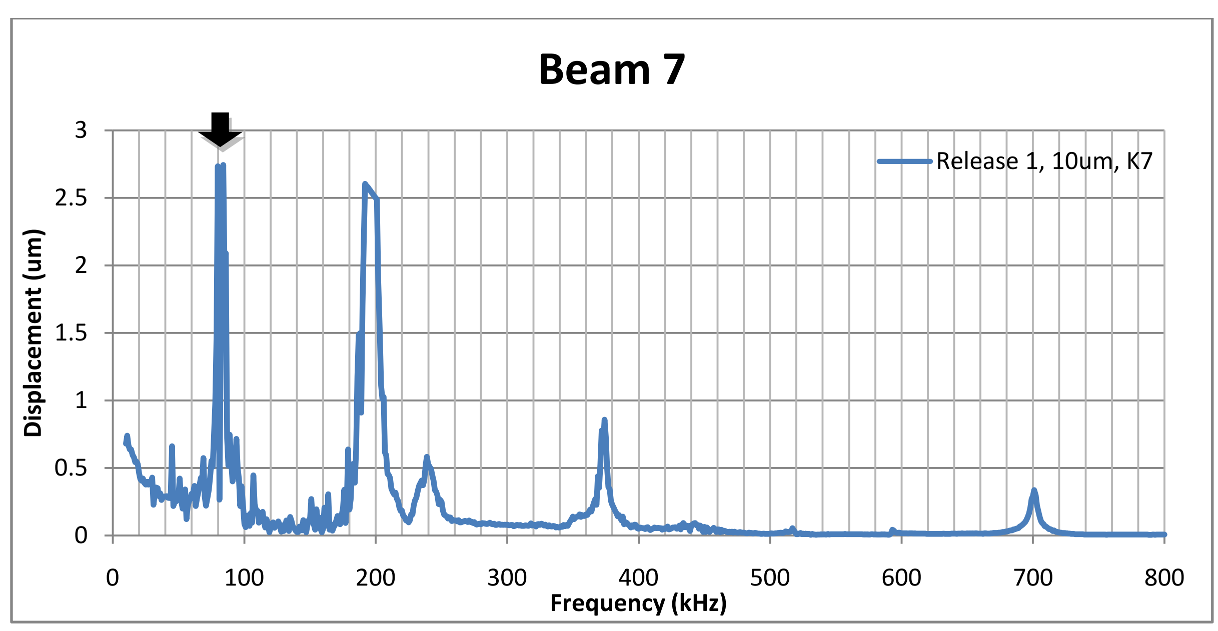

Figure 78. Frequency response of a 750μm long clamped-clamped beam with 2 hours of doping

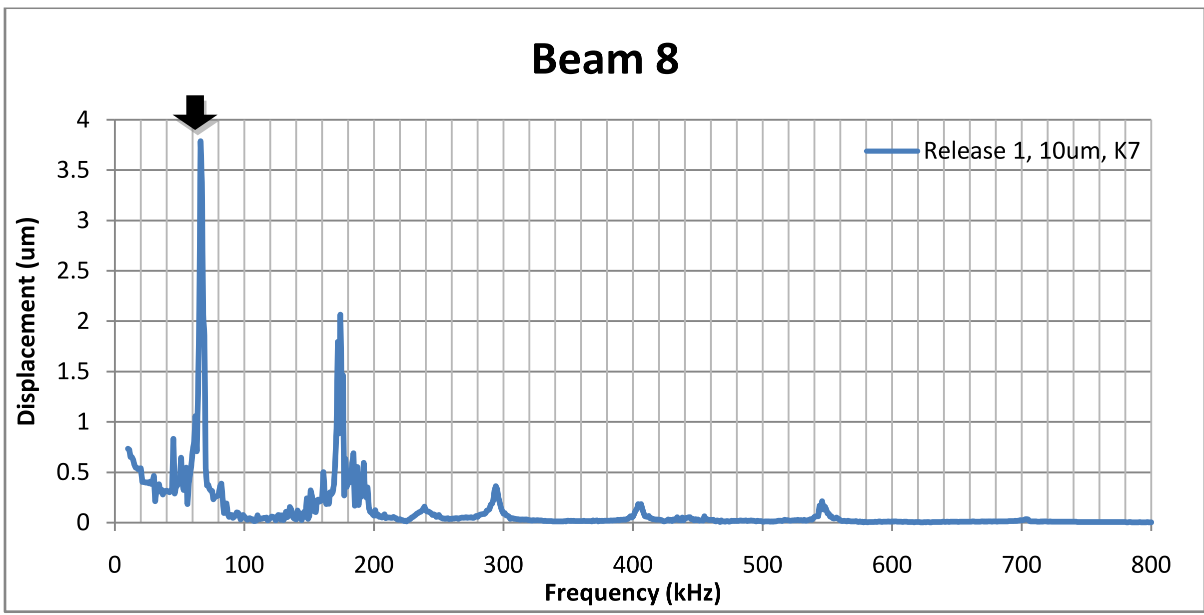

Figure 79. Frequency response of a 450μm long clamped-clamped beam with 2 hours of doping

2.5 HOURS DOPING RESONANT BEAM TEST RESULTS

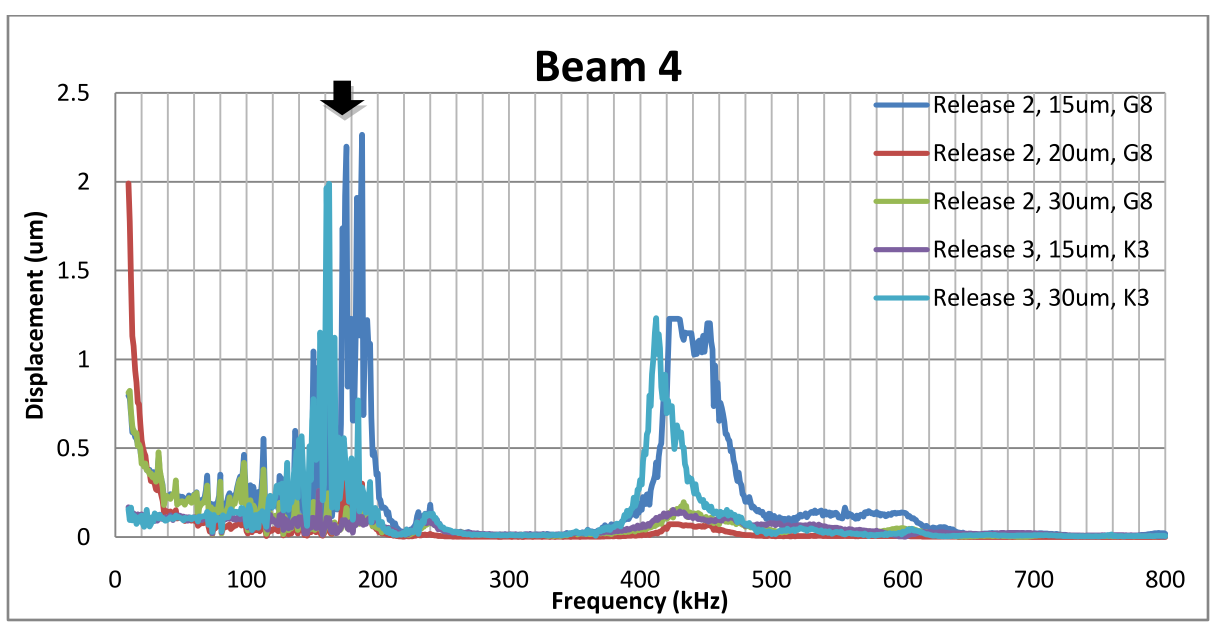

Figure 80. Frequency response of several 450μm long clamped-clamped beams with 2.5 hours of doping

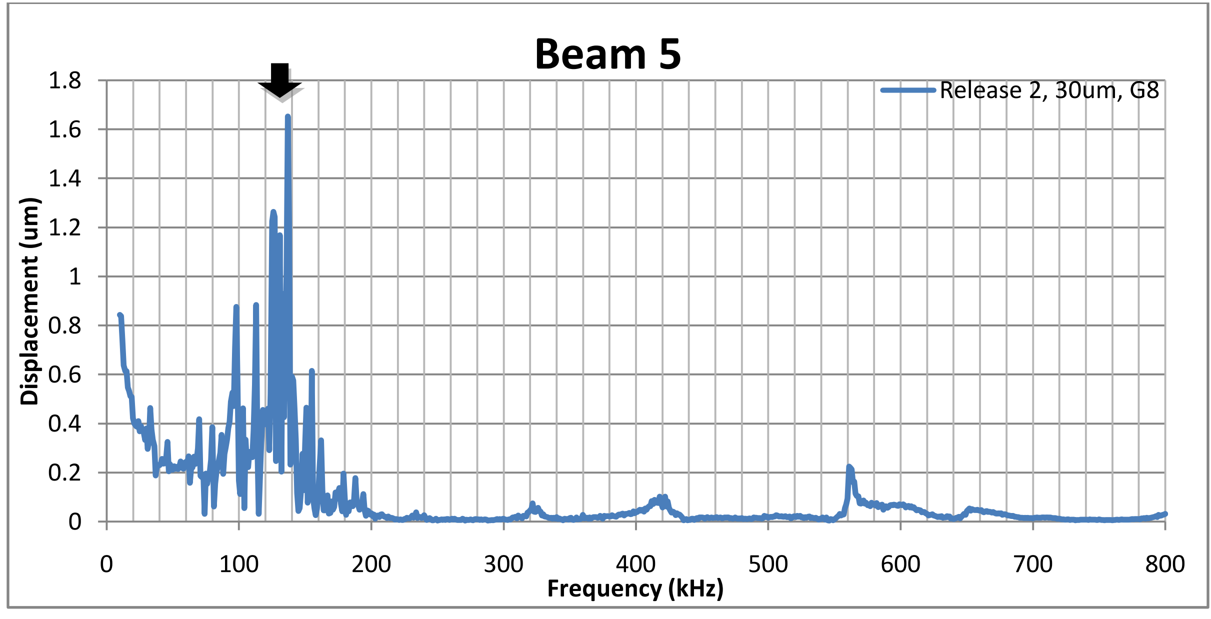

Figure 81. Frequency response of a 550μm long clamped-clamped beam with 2.5 hours of doping

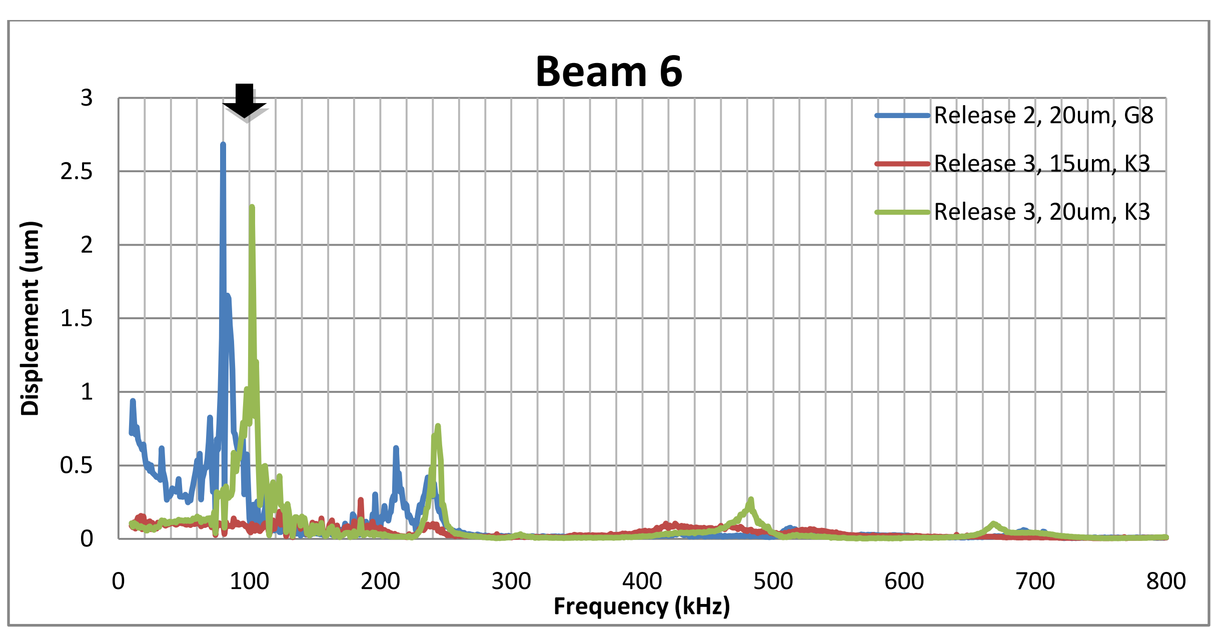

Figure 82. Frequency response of several 650µm long clamped-clamped beams with 2.5 hours of doping

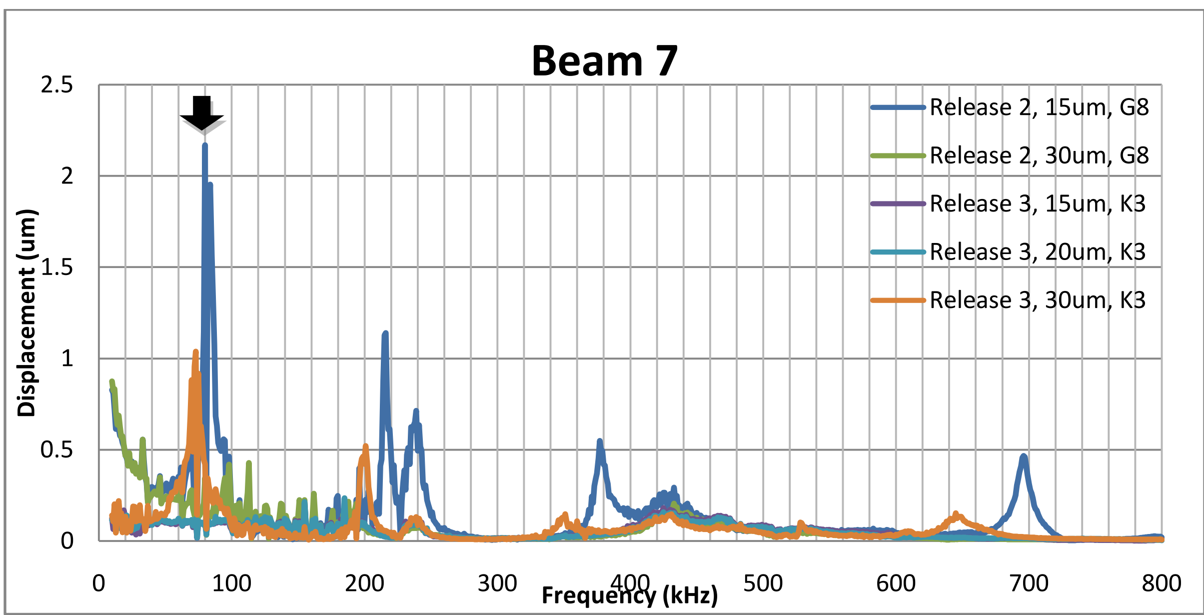

Figure 83. Frequency response of several 750µm long clamped-clamped beams with 2.5 hours of doping

Bibliography

1. *Effect of phosphorus doping on stress in silicon and polycrystalline silicon.* **S.P. Murarka, T.F. Retajczyk Jr.** 4, April 1983, J. Appl. Phys., Vol. 54, pp. 2069-2072.

2. *Mechanical properties of phsophorus-doped polysilicon films.* **S.W. Lee, C.H. Cho, J.P. Kim, S.J. Park, S.W. Yi, D.I. Cho.** November 1998, Journal of the Korean Physical Society, Vol. 33, pp. 392-395.

3. *Stress and thermal expansion of boron-doped silicon membranes on silicon substrates.* **B.S. Berry, W.C. Pritchet.** 4, July/August 1991, J. Vac. Sci. Technol. A, Vol. 9, pp. 2231-2234.

4. *Residual stress and mechanical properties of boron-doped p+ silicon films.* **Ding, X., Ko, W.H., Mansour, J.M.** 1990, Sensors and Actuators, Vols. A21-A23, pp. 866-871.

5. *A study of residual stress distribution through the thickness of p+ silicon films.* **Chu, W.H., Mehregany, M.** 1993. IEEE Transactions of electronic devices. Vol. 40 No. 7, pp. 1245-1250.

6. *Microphysical investigation on mechanical structuresrealized in p+ silicon.* **Cabuz, C., Fukatsu, K., Kurabayashi, T., Minami, K., Esashi, M.** 3, September 1995, Journal of Microelectromechanical Systems, Vol. 4, pp. 109-116.

7. *Elastic properties and representative volume element of polycrystalline silicon for MEMS.* **Cho, S.W., Chasiotis, I.** 2007, Experimental Mechanics, Vol. 47, pp. 37-49.

8. *New test structures and techniques for measurement of mechanical properties of MEMS materials.* **Sharpe Jr., W.N., Yuan, B., Vaidyanathan, K. R., Edwards, R.L.** 1996. SPIE Symposium on micromachining and microfabrication. Vol. 2880, pp. 78-91.

9. *Process temperature-dependent mechanical properties of polysilicon measured using a novel tensile test structure.* **Kamiya, S., Kuypers, J.H., Trautmann, A., Ruther, P., Paul, O.** 2, April 2007, Journal of Microelectromechanical Systesms, Vol. 16, pp. 202-212.

10. *Measurement of mechanical properties for MEMS materials.* **Yi, T., Kim, C.J.** 1999, Measurement Science Technology, Vol. 10, pp. 706-716.

11. **Sharpe Jr., W.N.** *An interferometric strain displacement measurement system.* s.l. : NASA , 1989.

12. *High-cycle fatigue of single-crystal silicon thin films.* **C.L. Muhlstein, S.B. Brown, R.O. Ritchie.** 4, December 2001, Journal of Microelectromechanical Systems, Vol. 10, pp. 593-600.

13. *Mechanical characerization of polysilicon through on-chip tensile tests.* **A. Corigliano, B. De Masi, A. Frangi, C. Comi, A Villa, M. Marchi.** 2, April 2004, Journal of Microelectromechanical Systems, Vol. 13, pp. 200-219.

14. *Dynamic MEMS devices for multi-axial fatigue and elastic modulus measurement.* **White, C.D., Xu, R., Sun, X., Komvopoulos, K.** 2003. SPIE: Reliability, testing, and characterization of MEMS/MOEMS II. Vol. 4980, pp. 63-74.

15. *Micromechanical and tribological characterization of doped single-crystal silicon and polysilicon films for microelectromechanical systems devices.* **B. Bhushan, X. Li.** 1, January 1997, Journal of Material Research, Vol. 12, pp. 54-63.

16. *Mechanical characterization of micro/nanoscale structures for MEMS/NEMS applications using nanoindentation techniques.* **Li, X., Buhashan, B., Takashima, K., Baek, C.W., Kim, Y.K.** 2003, ULTRAMICROSCOPY, Vol. 97, pp. 481-494.

17. *Evaluation of size effect on mechanical properties of single crystal silicon by nanoscale bending test using AFM.* **T. Namazu, Y. Isono, T. Tanaka.** 4, December 2000, Journal of Microelectromechanical Systems, Vol. 9, pp. 450-459.

18. *Measurement of Young's modulus on microfabricated structures using a surface profiler.* **Y.C. Tai, R. Muller.** 1990. IEEE Xplore. pp. 147-152.

19. *Young's modulus of in situ phosphorus-doped polysilicon.* **M. Biebl, G. Brandl, R.T. Howe.** Stockholm, Sweden : s.n., 1995. The 8th International Conference on Solid-State Sensors and Actuators, Eurosensors IX. pp. 80-83.

20. *Determination of the elastic modulus of thin film materials using self-deformed micromachined cantilevers.* **Fang, W.** 1999, J. Micromech. Microeng., Vol. 9, pp. 230-235.

21. *Laterally driven polysilicon resonant microstructures.* **Tang, W.C., Nguyen, T.C.H., Howe, R.T.** 1989. IEEE Xplore. pp. 53-59.

22. *A MEMS-based evaluation of mechanical properties of metallic thin films.* **Reddy, A., Kahn, H., Heuer, A.H.** 3, June 2007, Journal of Microelectromechanical Systems, Vol. 16, pp. 650-658.

23. *Measurement of Young's modulus and internal stress in silicon microresonators using a resonant frequency technique.* **Zhang, L.M., Uttamchandani, D., Culshaw, B., Dobson, P.** 1990, Measurement Science Technology, Vol. 1, pp. 1343-1346.

24. *M-TEST: A test chip for MEMS material property measurement using elecrtostatically actuated test structures.* **Osterberg, P.M., Senturia, S.D.** 2, June 1997, Journal of Microelectromechanical Systems, Vol. 6, pp. 107-118.

25. *Material property measurements of micromechanical polysilicon beams.* **Gupta, R.K., Osterberg, P.M, Senturia, S.D.** 1996. SPIE: Microlithography and metroogy in micromachining II. pp. 1-7.

26. *The lattice contraction coefficient of boron and phosphorus in silicon.* **McQuhae, K.G., Brown, A.S.** 1972, Solid-State Electronics, Vol. 15, pp. 259-264.

27. *Lattice parameter study of silicon uniformly doped with boron and phosphorus.* **Celotti, G., Nobili, D., Ostoja, P.** 1974, Journal of Materials Science, Vol. 9, pp. 821-828.

28. *A micro strain gauge with mechanical amplifier.* **Lin, L., Pisano, A.P., Howe, R.T.** 4, December 1997, Journal of Microelectromechanical Systems, Vol. 6, pp. 313-321.

29. *Bent-beam strain sensors.* **Gianchandani, Y.B., Najafi, K.** 1, March 1996, Journal of Microelectromechanical Systems, Vol. 5, pp. 52-58.

30. *Diagnostic microstructures for the measurement of intrinsic strain in thin films.* **Guckel, H., Burns, D., Rutigliano, C., Lovell, E., Choi, B.** 1992, Journal of Micromechanics and Microengineering, Vol. 2, pp. 86-95.

31. *Modeling of strain in boron-doped silicon cantilevers.* **Rueda, H.A., Law, M.E.** 1998. International Conference of Modeling and Simulation of Microsystems, Semiconductors, Sensors and Actuators. pp. 94-99.

32. *Characterization of the mechanisms producing bending moments in polycrystalline micro-cantilever beams by interferometric deflection measurement.* **Lober, T.A., Huang, J., Schmidt, M., A., Senturia, S.D.** 1988. IEEE. pp. 92-95.

33. *Determining mean and gradient residual stress in thin films using micromachined cantilevers.* **Fang, W., Wickert, J.A.** 1996, Journal of Microengineering, Vol. 6, pp. 301-309.

34. **Levinshtein, M., Rumyantsev, S., Shur, M.** *Handbook Series on Semiconductor Parameters.* Danvers : World Scientific Publishing Co. Pte. Ltd., 1996. Vol. 1.

35. *Thermal expansion coefficient of polycrystalline silicon and silicon dioxide thin films at high temperatures.* **Tada, H., Kumpel, A.E., Lathrop, R.E., Slanina, J.B., Nieva, P., Zavracky, P., Miaoulis, I.N., Wong, P.,Y.** 9, May 1, 2000, Journal of Applied Physics, Vol. 87, pp. 4189-4193.

36. *Analysis and design of polysilicon thermal flexure actuator.* **Huang, Q.A., Lee, N.K.S.** 1999, Journal of Micromechanics and Microengineering, Vol. 9, pp. 64-70.

37. *Modeling the thermal behavior of a surface-micromachined linear-displacement thermomechanical microactuator.* **Lott, C.D., McLain, T.W., Harb, J.N., Howell, L.L.** 2002, Sensors and Actuators A, Vol. 101, pp. 239-250.
38. *Measurement of fracture stress, Young's modulus, and intrinsic stress of heavily boron-doped silicon microstructures.* **Najafi, K., Suzuki, K.** 1989, Thin Solid Films, Vol. 181, pp. 251-258.
39. *Interferometry of actuated microcantilevers to determine material properties and test structure nonidealities in MEMS.* **Jensen, B.,D., de Boer, M.P., Masters, N.,D., Bitsie, F., LaVan, D.A.** 3, September 2001, Journal of Microelectromechanical Systems, Vol. 10, pp. 336-346.
40. *Design Properties of Polyscrystalline Silicon.* **Kamins, T.I.** 1990, Sensors and Actuators, Vols. A21-A23, pp. 817-824.
41. **Sze, S.M.** *VLSI Technology.* New York : McGraw-Hill, 1988.
42. *Diffusion of impurities in polycrystalline silicon.* **Kamins, T.I., Manolin, J., Tucker, R.N.** 1972, Journal of Applied Physics, Vol. 43, p. 83.
43. *A Quantitative Model for the Diffusion of Phosphorus in Silicon and the Emitter Dip Effect.* **Fair, R.B, Tsai, J.C.C.** 7, July 1977, Journal of the Electrochemical Society: Solid-state Science and Technology, Vol. 124.
44. *Solubility of implanted dopants in polysilicon: phosphorus and arsenic.* **Lifshitz, N.** December 1983, Journal of the Electrochemical Society: Solid-State Science and Technology, pp. 2464-2468.
45. *Effects of phosphorus on stress of multi-stacked polysilicon film and single crystalline silicon.* **Lee, C. S., Lee, J.H., Choi, C.A., No, K., Wee, D.M.** 1999, Journal of Micromechanical Microengineering, Vol. 9, pp. 252-263.
46. *Kinetics of phosphorus proximity rapid thermal diffusion using spin-on dopant source for shallow junctions fabrication.* **Grabiec, P.B., Zagozdzon-Wosik, W.** 1, March 1995, Journal of Applied Physics, Vol. 78, pp. 204-211.
47. *Relationship between resistivity and phosphorus concentration in silicon.* **Mousty, F., Ostoja, P., Passari, L.** 10, October 1974, Journal of Applied Physics, Vol. 45, pp. 4576-4580.
48. **Cham, Jorge.** PhD comics. [Online]
49. **A. Frangi, C. Cercignani, S. Mukherjee, N. Aluru.** *Advances in multiphysics simulation and experimental testing of MEMS.* London : Imperial College Press, 2008.